Title
Ultrafast Spectroscopy of Correlated Electron Systems

Author
Schmid, Benjamin Andrew

Publication Date
2009

Peer reviewed|Thesis/dissertation

Ultrafast Spectroscopy of Correlated Electron Systems

by

Benjamin Andrew Schmid

A dissertation submitted in partial satisfaction of the

requirements for the degree of

Doctor of Philosophy

in

Applied Science and Technology

in the

Graduate Division

of the

University of California, Berkeley

Committee in charge:

Professor Oscar D. Dubon, Chair
Professor Eugene E. Haller
Professor Dung-Hai Lee

Fall 2009

The dissertation of Benjamin Andrew Schmid, titled Ultrafast Spectroscopy of Correlated Electron Systems, is approved:

Chair _____ Date _____

_____ Date _____

_____ Date _____

University of California, Berkeley

Ultrafast Spectroscopy of Correlated Electron Systems

Abstract

Ultrafast Spectroscopy of Correlated Electron Systems

by

Benjamin Andrew Schmid

Doctor of Philosophy in Applied Science and Technology

University of California, Berkeley

Professor Oscar D. Dubon, Chair

This dissertation attempts to illuminate and expand our understanding of charge dynamics in a number of different semiconductor materials, in particular the behavior of electron-hole pairs which are correlated via the long-range Coulomb interaction. Terahertz spectroscopy gives us direct access to probe the fundamental excitations of quasiparticles in a wide range of materials systems. By probing the low-energy excitations of materials on short time scales, one can learn a great deal about their quasiparticles and dynamics as well as explore new tools for their manipulation.

Carriers in semiconductors, existing either as bound electron-hole pairs or "free" carriers (or both), are particularly amenable to this avenue of study. The internal structure of excitons in semiconductors lies energetically in the far- to mid-infrared. Free carriers moving under the influence of a free-space electric field reveal much about themselves. By exploiting this unique window, one can both characterize and manipulate these systems in novel ways, as well as seek to understand the physics of new materials.

I study the ferromagnetic semiconductor gallium manganese phosphide (GaMnP) to better understand the role of charge carriers in the origins of ferromagnetism. By applying the tools of terahertz spectroscopy, I am able to make contact free measurements of hole populations in a novel GaMnP film.

I exploit THz spectroscopy to provide a direct gauge of bound and unbound pair densities in gallium arsenide quantum wells, enabling the observation of the excitonic fine structure as it evolves under high-density conditions. And finally I have observed for the first time stimulated emission of far-infrared radiation from internal transitions in excitons in the semiconductor Cu_2O. Broadband THz spectroscopy is employed to directly map out the ultrafast dynamics, spectral positions, and line broadenings of intra-excitonic transitions. This work has opened up new possibilities for the quantum manipulation of excitons. With these studies, I continue to test and expand the atomic analogy of excitons.

to Tarisa

and

in Memory of
Daniel S. Chemla

Contents

List of Figures

Acknowledgments

I am eager to take this opportunity to thank those without whose help and support I could never have persevered in my time at Berkeley. It is a hopeless task to mention everyone who had a significant positive impact on my studies, but I would like to single out a few in particular.

First and foremost, I am indebted to Prof. Chemla, whose faith in me and whose determination to make me a better scientist have shaped who I am and how I see myself today. He was a mentor par excellence, and his passing is a great loss to those around him and the wider scientific community.

In his absence, many have stepped in to fill his shoes as advisor and mentor. I am especially grateful to Dr. Rupert Huber for sharing his knowledge and contagious enthusiasm for research during our many long evenings in the THz lab. He is without a doubt the best teacher I have ever had. The expertise, supervision, and support of Dr. Kaindl have been indispensable during my time in Berkeley. Without his hard work and dedication, it is doubtful that any of us in the Chemla group could have accomplished much during Daniel's illness. I am especially grateful to Prof. Dubon, who has patiently and graciously supported me throughout my studies as an academic advisor, and now by stepping in as committee chair.

I would also like to thank all the members of the Chemla group who taught me many important lessons, in physics and life, especially Keshav Dani, Neil Fromer, Ingrid Cotoros, Nils Nielsen, Marc Carnahan, Chi-Wei Lai, and Michael Breit. I would like to specially thank Jigang Wang for his patient guidance and friendship during both my graduate *and* undergraduate studies.

I would like to acknowledge and thank the faculty and staff of the AS&T program, especially Pat Beruman, who was always there for me when I was most in need of help and support. It is beyond the shadow of a doubt that without her I could never have made it through my time here.

Last but surely not least, I would like to thank my family. To my parents, thank you for teaching, motivating, and supporting me throughout the long and arduous journey. To Becky, Thomas and the kiddos, thank you for your love and support.

And to my wife Tarisa, if no other good thing had come of my time in Berkeley, meeting you would have made it all worthwhile. Thank you for your love, your gentleness, your faith and support, and your patience.

Finally, to the countless others who must go unmentioned, as I cannot possibly name you all, I am truly grateful for your time, support, inspiration, knowledge, motivation, and vision. Without you, I would not be who I am today. Thank you.

Chapter 1

Introduction

1.1 Motivation

The growth of our understanding of the physics of semiconductors in the past century has revolutionized not just those disciplines directly tasked with their study but all of society. The ways in which we communicate, do business, or spend our leisure time have all been radically altered by the manipulation of the electronic properties of semiconductors. From integrated circuits, to optical communications, to laser printers, it is difficult to find a facet of modern society which has been left untouched. Over the course of this revolution, there has been an explosion of materials to continue the advancement. As technologies continue to be pushed to new limits, understanding newly relevant quantum size effects, novel materials, and continued integration are of fundamental importance.

The interaction of matter with light allows for a rich and complex study of the physics and properties of these new materials and systems. In particular, ultrafast spectroscopy grants access to previously impenetrable time-scales for our observations. It is now possible to observe the response of a physical system with time resolutions able to resolve the response time of many of the most fundamental excitations of that system. At high pulse energies and short pulse durations, a wide array of linear and nonlinear spectroscopic techniques may be brought to bear on a wide range of fields of inquiry.

Two major themes can be identified throughout the following investigations: the application of ultrafast optical techniques, especially time-domain terahertz spectroscopy to the study of semiconductors, and the effects of engineering on the nanoscale. Terahertz spectroscopy gives us direct access to probe the fundamental excitations of quasiparticles in a wide range of materials systems. The THz regime lies in the far-infrared, from the microwave (hundreds of GHz or $\lesssim 1$ meV) to the mid-infrared ($\gtrsim$ tens of meV). One THz is equal to approximately 4.1 meV or 33 cm^{-1}. By probing the low-energy excitations of materials on short time scales, one can learn a great deal about their quasiparticles and dynamics as well as explore new tools for their manipulation. And as dimensions are reduced to nanometer scales, new physical behaviors are encountered as quantum effects become significant or even dominant in the physics of these systems.

1.2 Outline of dissertation

This dissertation attempts to illuminate and expand our understanding of charge dynamics in a number of different semiconductor materials, in particular the behavior of electron-hole pairs which are interacting via the long-range Coulomb interaction.

This first chapter, beyond providing a road map for my presentation, also includes a short discussion of a few basic concepts which will recur frequently in the subsequent chapters.

In chapter 2, I discuss ultrafast optical techniques and their application to the study of semiconductors. I focus particularly on the utility of time domain terahertz spectroscopy to resonantly probe quasiparticles and their dynamics. I also discuss and briefly explain the key optical tools and techniques which are applied in the subsequent chapters.

In chapter 3, I present measurements of charge density in the carrier-mediated ferromagnet gallium manganese phosphide. Application of time-domain terahertz spectroscopy allows for a new sensitive and contact-free measurement of the free-carrier density in this unusual material. Holes play a key role in the origins of ferromagnetism in magnetic semiconductors, in ways that are very different from traditional magnetic metals. This study helps to further the understanding of the origins of long-range ferromagnetic order in this unusual material.

In chapter 4, I present studies of the behavior of excitons at high densities in gallium arsenide quantum wells. Here, I attempt to push the limits of the hydrogenic picture of excitons. A dilute exciton gas is known to be insulating, while an electron-hole plasma is conductive. I seek to more deeply understand the transition between these regimes, and test the boundaries of the atomic analogy for excitons.

In chapter 5, I present the first observations of stimulated terahertz emission from internal exciton transitions in cuprous oxide (Cu_2O). This study demonstrates the potential for the direct, coherent manipulation of excitons by far-infrared light. I also discuss a closely related observation of the generation of terahertz radiation by quantum beating of internal exciton levels. This again allows me to further expand the atomic analogy to excitons.

1.3 Background

A few key concepts which recur frequently throughout this work are worthwhile to be briefly reviewed at the outset.

1.3.1 Optical properties of semiconductors

Optical dielectric function

The dielectric function $\epsilon(\omega)$ concisely describes the linear response of a material to an electric field. Because the response is not instantaneous, it depends on the electric field at all previous times–or equivalently it is both frequency dependent and complex,

$\epsilon(\omega) = \epsilon_1(\omega) + i\epsilon_2(\omega)$. This causality restriction, that the response depends on the past, but obviously not on the future, places a strict relation between the real and imaginary parts of the dielectric function. This "Kramers-Kronig" relation means that if the real part of the dielectric constant is known for all frequencies, the imaginary part can be computed exactly, and vice-versa. It is often exploited in spectroscopy to try to calculate the full complex dielectric function based on incomplete data, usually transmission, by making assumptions about the behavior outside of the measurement window. Measurements over a very large wavelength range are necessary for this, often from the far-infrared up to the ultraviolet.

One of the greatest advantages of time-domain terahertz spectroscopy (TDTS) is that no such assumptions are necessary to measure the full, complex dielectric function within the spectral window of interest. The oscillating electric field of the far-infrared pulse is directly measured, giving both amplitude *and* phase information about the material in the optical path. Thus both real and imaginary parts of the dielectric function are directly measurable with this technique.

There are a number of equivalent quantities containing the same information as the dielectric function: the dielectric susceptibility ($\chi^{(1)} = \epsilon - 1$), the complex conductivity $\sigma(\omega) = \frac{-i\omega}{4\pi}(\epsilon(\omega) - 1)$, and the index of refraction $N(\omega) = [\epsilon(\omega)]^{1/2}$. Absorption is proportional to the imaginary index of refraction, while the real part tells us about the speed of light in the medium. The complex dielectric $\epsilon(\omega)$ function can also be expressed by the real part of the dielectric function and the real part of the conductivity:

$$\epsilon(\omega) = \epsilon_1(\omega) + i\frac{4\pi}{\omega}\sigma_1(\omega) \tag{1.1}$$

While each of the quantities or representations contains the same information, the different representations may be utilized to make one feature or another more concise or apparent. When discussing the response of free carriers, for example, it is most natural to speak in terms of the complex conductivity, while when discussing the optical properties of an insulator, the index of refraction is more appropriate. For example, when measuring the density of holes in gallium manganese phosphide, I plot the conductivity to analyze the "metallic" behavior of the material. In the search for stimulated emission from excitons, on the other hand, the absorption and real index of refraction are naturally most illuminating given the sign change when moving between absorption and emission.

Oscillator sum rule

Because of the constraints placed on the dielectric function (or conductivity or index of refraction) by the causality discussed above, it is possible to make some general, though rigorous, statements about these functions. The most useful of these are the sum rules, which relate the total spectral weight of the functions to real quantities in the material under study. For example, within a parabolic band approximation it is known that the area under the real part of the conductivity is directly linked to the charge and mass of the

quasiparticle involved in the excitation:

$$\int_0^\infty \sigma_1(\omega) d\omega = \frac{\pi}{2} \sum_j \frac{(q_j)^2}{M_j} \tag{1.2}$$

This allows for observations of the optical conductivity to be directly linked to the density of quasiparticles, be they free carriers, phonons, or excitons.

1.3.2 Interest in semiconductor nanostructures

The behavior of semiconductors at the nanoscale is of interest for several reasons: (1) to allow the observation and utilization of quantum mechanical effects which are manifest only at sufficiently small length scales, (2) to take advantage of a convergence of scales with natural molecular processes, such as in medicine, or (3) to make an existing device or technology smaller, without necessarily seeking to change its fundamental physics. In the first two cases, the driving goal is to take advantage of new nanoscale effects previously unavailable or unobserved. In the latter case, the new nanoscale effects must be understood so that they can be tamed or avoided, rather than explicitly utilized. In the work at hand, the motivation is primarily the first case: to either study or exploit quantum mechanical effects only observable at the nanoscale. Key impacts of nanoscale confinement on the optical properties of semiconductors include two important forms: increasing energy due to confinement and broken symmetry. In chapter 4, I take advantage of the effects of confinement in GaAs quantum wells to provide a well defined and accessible model system for a study of exciton dynamics.

Chapter 2

Ultrafast spectroscopic techniques

The invention of the solid-state laser in 1960 ushered in an new era of spectroscopy.[1] For the first time, researchers had access to an intense, coherent, monochromatic light source which was tunable across broad spectral ranges. Up to this point, thanks to the weak interaction of light and matter, nonlinear optics were hopelessly out of reach. The achievement of mode-locked pulsed lasers, where many laser modes are "locked" together to resonate in concert producing pulses of light which are broad in frequency and short in time, now allows the creation of ultrashort pulses with astounding peak powers of a terawatt or more. Starting from commercially oscillator/amplifier systems, researchers from a wide variety of disciplines now have the ability to construct tabletop optical laboratories where states of matter may be studied using photons from the far-infrared (FIR) to the deep ultraviolet and even X-ray. It is even possible to create a laser driven tabletop particle accelerator.[2]

In the experimental work presented in the follow chapters, I utilize a highly customized Titanium-doped sapphire laser oscillator and regenerative amplifier system driving a variety of non-linear optical processes harnessed for the study of charge carriers in solids. In this introductory chapter, I will briefly describe the underlying principles, utility, capabilities, and basic operation of these tools. To begin, I give a brief primer of the nonlinear optics used in these systems. Then I briefly describe the Titanium-doped sapphire laser: its operation, capabilities and limitations, as well as a brief description of the specific $Ti{:}Al_2O_3$ lasers used in this work. Next I describe the construction and operation of a visible optical parametric amplifier used extensively in these studies. Finally, I will discuss the details of time-domain terahertz spectroscopy, the primary tool utilized in the subsequent experiments.

2.1 Non-linear optics

Generally speaking, only laser light is sufficiently intense to invoke a measurable non-linear optical response from matter. Nonlinear optics was only born in 1961 shortly after the invention of the laser in 1960.[1,3] Simply put, one can write the polarization induced in

a material as a power series in electric field. The linear term $\chi^{(1)}$ is the familiar dielectric susceptibility from section 1.3.1, where $\mathbf{P} = \chi\mathbf{E}$. The series may be continued, however, to $\chi^{(2)}$, $\chi^{(3)}$ and above ($\mathbf{P}(t) = \chi^{(1)}\mathbf{E}(t) + \chi^{(2)}\mathbf{E}^2(t) + \chi^{(3)}\mathbf{E}^3(t) + \dots$). The spectroscopic tools utilized in this work, time domain terahertz spectroscopy, harmonic generation, optical parametric amplification, are generally all second order ($\chi^{(2)}$) processes.

Importantly, these second order interactions may occur only in the case of materials lacking inversion symmetry (non-centrosymmetric).[4] It is also important that in the power law expansion in the previous paragraph, it is assumed that the polarization at any point in time is described exclusively by the electric field at that exact same point in time. This is equivalent to saying that the response in instantaneous, which implies, by causality and the Kramers-Kronig relations, that the medium has no absorption at these frequencies. These lossless processes are often referred to as "parametric."

Focusing on the second order interactions, one can examine the case where the driving electric field is the superposition of two frequencies: $\mathbf{E} = E_1 e^{-i\omega_1 t} + E_2 e^{-i\omega_2 t} + c.c.$, where "*c.c.*" is the complex conjugate. The second order polarization may thus be written down as

$$\begin{aligned}\mathbf{P}^{(2)} = \chi^{(2)}\Big[&E_1^2 e^{-2i\omega_1 t} + E_2^2 e^{-2i\omega_2 t} + 2E_1E_2 e^{-i(\omega_1+\omega_2)t} \\ &+ 2E_1E_2^* e^{-i(\omega_1-\omega_2)t} + E_1E_1^* + E_2E_2^* + c.c.\Big]\end{aligned} \tag{2.1}$$

Each of these terms is relevant to the tools mentioned above. The first two terms have a frequency of exactly twice the input frequency. This effect is used in this work for the generation of high energy photons both to pump the optical parametric amplifier (OPA) and to excite semiconductors non-resonantly well above their band-gaps. This is known as second harmonic generation (SHG), or simply frequency doubling. The third term, with a frequency of $\omega_1 + \omega_2$ is sum frequency generation (SFG), or up-conversion. Second harmonic generation can be thought of as simply a degenerate case of SFG. Here two photons are in effect "added" together to generate a new photon of higher energy. This effect is utilized in the detection portion of time-domain terahertz spectroscopy, discussed below. The fourth term similarly is difference frequency generation (DFG), or down-conversion, where the created photon has an frequency equal to the difference of the two driving fields. This interaction underpins both the generation portion of the time-domain terahertz spectrometer as well as forming the "heart" of the optical parametric amplifier used as a tunable light source.

Finally, the last terms, which lack any time dependence (equivalently, zero frequency), are referred to as optical rectification (OR). Just as second harmonic generation is the sum of a particular frequency with itself, optical rectification is the *difference* of a particular frequency with itself. Terahertz generation is often called optical rectification, because it involves the self-interaction of an optical pulse with itself. The result, however, is not at precisely zero frequency, but at far-infrared frequencies because of the interaction of the full, non-zero bandwidth of an ultrafast pulse with itself. Thus the "rectification" of an

ultrafast optical pulse will have frequency components from DC (zero frequency) all the way up to the bandwidth of the pulse.

An optical parametric amplifier is fundamentally a difference frequency generator involving the interaction of three waves of very different intensities. A strong "pump" pulse of high photon energy interacts in a nonlinear medium with a weak seed pulse of a lower frequency. Through difference frequency generation, the high energy photon is annihilated, and two photons are generated: one at the difference frequency ($\omega_{\text{pump}} - \omega_{\text{seed}}$) called the "idler", and by conservation of energy a second is created at the original seed energy. Thus a pump and a seed photon go in, and an idler and two "seed" photons come out. This multiplication (amplification) of the seed pulse is precisely the intended effect in optical parametric amplification.[5–7]

2.2 Ti:sapphire lasers

The titanium-doped sapphire ($Ti{:}Al_2O_3$), more than any other single lasing medium, has revolutionized ultrafast and non-linear optics. The $Ti{:}Al_2O_3$ laser has become the preeminent ultrafast laser for a number of reasons: its unparalleled bandwidth, superb efficiency, and physical durability.

Like the first ruby laser, the key to lasing in $Ti{:}Al_2O_3$ is the transition metal ion. In this case, the Ti^{3+}'s lone $3d$ electron couples to the sapphire lattice, lifting its five-fold degeneracy, creating a triplet ground state and two excited states. Absorption between these triplet and excited states occurs at around 500 nm.[8] However, when the electron is in the excited state, it is energetically favorable for the ion to displace with respect to the lattice in the Jahn-Teller effect, lowering the excited state energy and raising the ground state level.[9] A photon emitted during relaxation between these modified states, therefore, is of lower energy, centered in this case around 800 nm. It is this coupling with the crystal lattice which gives the $Ti{:}Al_2O_3$ its bandwidth and efficiency.

The energy of the ground state varies strongly with the displacement of the Ti^{3+} ion, meaning that the occupied excited state, after relaxing to its preferred displacement, even with a relatively moderate displacement distribution about equilibrium, may relax to a very wide range of highly non-equilibrium ground state energies. After emission from the displaced excited state to the displaced ground state, the atom very quickly relaxes to its original ground state by the emission of phonons.

Finally, all higher excited states are much higher in energy still, such that neither the 800 nm nor 500 nm photons are energetic enough to couple the excited state to them. This means that the Ti^{3+} ions have no excited state absorption at the lasing wavelength. All infrared absorption seen in these crystals is due to improper incorporation of the titanium dopants or other trace impurities.[10,11]

Like is the case so often, a key element of the continued success of the $Ti{:}Al_2O_3$ laser is the development of the materials science behind its production. As discussed above, the Titanium dopant must be incorporated into the crystal substitutionally, or else the

crystal will display parasitic absorption at the lasing wavelength, strongly limiting the efficiency. As the materials science has improved, crystal growers have been able to achieve higher substitutional titanium incorporation. This means that for the same gain, one can use a shorter crystal length, reducing the dispersion that must be compensated to create ultrashort pulses.

Sapphire is among the hardest materials in nature (after, for example, diamond and silicon carbide), and has an exceptionally high thermal conductivity. This allows for the construction of power amplifiers with very high pump intensities without damaging the crystal.

2.2.1 Oscillator

To create an ultrashort (sub-picosecond) pulse in the NIR, it is clear from basic Fourier analysis that the spectrum of the pulse must be quite broad. Lasers, however, are traditionally known for exceptionally *narrow* spectra, where one single oscillation mode with the maximum net gain out-competes all other possible lasing modes to become the sole oscillation mode of the lasing cavity. The key to creating ultrafast pulsed lasers comes in forcing the cavity to operate coherently in many modes simultaneously. The process of forcing such operation is referred to as "mode-locking." Historically, a variety of techniques have been used to force mode-locking operation, from saturable absorbers to the Kerr effect using hard or soft apertures.[12–15] These methods all work on the same general principle: introduce a high-loss mechanism for single-mode operation. A laser operating in a single mode (continuous wave, or CW) has the same power at all times; a laser operating in a pulsed mode (mode-locked) for the same average power has a much higher peak power thanks to the small duty cycle. For a 80 MHz repetition rate oscillator with a pulse duration of 100 fs, this duty cycle is more than 1:100,000. If a loss mode has either a slow time response or a strong power dependence, it is possible to make pulsed operation the preferred mode.

Aperture mode-locking relies on the non-linear ($\chi^{(3)}$) Kerr effect. In this effect, the index of refraction of a material depends on the intensity of the light passing through it. As an optical pulse propagates through the crystal, its index of refraction increases in proportion to the instantaneous intensity of the pulse: $n(I) = n_0 + \lambda K I$, where K is a material dependent constant. This introduces a small phase delay at the center of the pulse, exactly like a positive lens. This Kerr-lens is significant for large intensities, but negligible for the small intensities of CW operation. By optimizing the laser cavity and pump overlap to match the spatial mode of pulsed-operation with its additional Kerr-lensing effects, the optical gain of mode-locked operation can be much higher than for CW. In fact, because any small perturbation from CW operation may result in momentarily higher gain, Kerr-mode-locked lasers are not only highly stable but can even be self starting thanks to this positive reinforcement. Most commonly, either a hard or soft aperture is used to decrease the cavity Q for CW operation. For a hard aperture, something is introduced into the laser cavity which will impinge on the beam waist for CW operation, but given the additional

focusing due to the Kerr effect, a pulsed mode is not interfered with. In the case of a soft aperture, as I use in the oscillators in this work, the gain profile created by the pump beam is used as the aperture. The additional self-focusing of the laser pulse gives a better spatial mode matching to the profile of the pump beam in the $Ti{:}Al_2O_3$ crystal, resulting in higher gain. Mode-locking is extremely stable, and can be started by any small perturbation to the oscillator cavity, typically shifting one of the intra-cavity prisms or even just tapping the table.

In this work I have utilized two different oscillators: in chapters 4 and 5, I use an off-the-shelf Coherent Inc. MIRA 900 with an autocorrelation sech ^{2} pulse width of 130 fs. For later experiments, this was replaced with a self-built oscillator based on a published design[16] in conjunction with a customized grating pulse shaper for seeding and recompressing the regenerative amplifier described in the next section. This oscillator is capable of producing pulses as short as 15 fs, but was operated at narrower bandwidth allowing 45 fs operation to optimize the seeding of the regenerative amplifier.

2.2.2 Regenerative amplifier

There are many applications where the nanojoule pulse energies from an oscillator are simply too small. In this case, it is necessary to amplify the pulses to the desired level. It is not possible, for example, to drive an OPA to resonantly pump a sample while simultaneously probing with terahertz pulses using the output of an oscillator. In this work, to have sufficient pulse energy to both optically excite a sample as well as to generate and detect the terahertz probe beam, I utilize a regenerative amplifier operating at a high (250 kHz) repetition rate. In this regenerative amplifier, the $Ti{:}Al_2O_3$ crystal is pumped continuously while spontaneous lasing is suppressed by means of a Q-switch, which can selectively misalign the amplifier cavity. At some point, when the crystal has been pumped with as much energy as possible, the Q of the cavity is simultaneously switched back high (the cavity is "realigned") and a single pulse from the oscillator is injected into the cavity mode. The pulse makes multiple passes through the highly population-inverted amplifier crystal, gaining as much energy as possible. As soon as the pulse energy saturates, it is then ejected from the cavity, and the Q is switched back low to begin "recharging" the amplifier crystal.[17] Thus one can trade repetition rate for peak power by allowing more pumping time between injected pulses up to the storage time of $Ti{:}Al_2O_3$ ($\sim 4\mu$s). Typically, the regenerative amplifier operates at 250 kHz while being seeded by an oscillator operating at 80MHz. The pulse energy is increased from the nanojoule level to over 6 μJ.

One limitation on the output power of the amplifier, however, is that the increasing peak power of the amplified pulse itself can cause changes in the mode or simply exceed the damage threshold of the materials in the amplifier. This restriction can be circumvented by carefully (and reversibly) stretching out the seed pulses in time before injecting them into the amplifier. By so chirping the pulse, the peak powers can be significantly reduced, and higher overall pulse energies obtained. The stretched, amplified pulse may then be recompressed after ejection from the amplifier. This stretching-amplification-compression

methodology is known as chirped pulse amplification.

In the measurements described in this work, I utilize a Coherent Inc. RegA 9000 regenerative amplifier operating at a repetition rate of 250 kHz. Like the oscillator described above, for the work in the later chapters it was modified for greater bandwidth and less dispersion and to accept pumping by a Verdi V18 diode-pumped solid state laser operating at 532 nm. After recompression, this customized laser amplifier delivers ultrafast pulses of 45 fs at a repetition rate of 250 kHz with an average power of 1.6W, or $> 6\mu$J per pulse at 810 nm.

2.3 Optical parametric amplifier

While the $Ti{:}Al_2O_3$ oscillator and amplifier are powerful and versatile tools in their own rights, there are a great many materials whose fundamental interband excitations do not fall within the pulse bandwidth. It is a tedious process to tune the center wavelength of the system more than ten or twenty nanometers, and accounting for all of the downstream optics which are sensitive to wavelength (prisms, gratings, dielectric mirrors, anti-reflection coatings), it can be simply prohibitive. When dealing with semiconductor nanostructures, the difficulty of achieving the appropriate excitation becomes even more challenging. Quantum confinement raises the fundamental excitation energy above that of the material bulk bandgap, often well into the visible or even ultraviolet range. For a material with a bandgap above 1.6 eV, non-linear optics are needed to convert the $Ti{:}Al_2O_3$ output into usable, higher energy photons for resonant pumping.

Fortunately, the short pulse duration and high average powers of the oscillator/amplifier system open up a wide range of non-linear optical techniques for producing higher energy photons. The simplest is second harmonic generation, typically in the crystal BBO (β-barium-borate), which produces photons with twice the energy of the fundamental. Power conversion efficiencies from 1.55 to $3.1eV$ as high as 50% are relatively straightforward to achieve with the pulse energies available in my lab. This arrangement, while generally good for highly non-resonant excitation at high average powers, will not allow for direct excitation of electron-hole pairs or excitons in their lowest energy state.

One can, however, utilize these second harmonic photons in another non-linear optical process, namely optical parametric amplification as described above, to generate photons of nearly any energy between the fundamental and second harmonic. Such a device was built as part of this thesis. Figure 2.1 shows a schematic representation of the OPA construction. In this design, a seed pulse is generated containing the desired signal wavelengths by continuum generation in sapphire. In continuum generation, an extremely intense laser pulse interacts with itself in a crystal to significantly broaden its spectrum. This occurs though the $\chi^{(3)}$ effects of Kerr lensing and self-phase modulation. The optical Kerr effect was briefly described in the earlier discussion of $Ti{:}Al_2O_3$ mode-locking, and in this case serves to further enhance the intensity of the pulse by self-focusing the pulse into a very small filament. Self-phase modulation occurs because the intensity dependent index of refraction

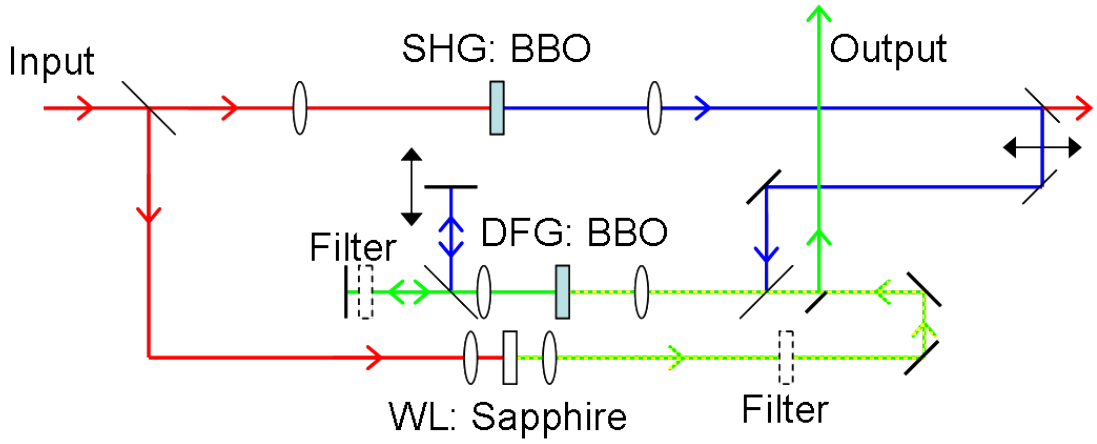

Figure 2.1: A schematic of the visible collinear optical parametric amplifier.

is rapidly varying with the intensity envelope of the ultrashort pulse. This produces shifts of the instantaneous phase of the electric field, which are thus changes of the frequency. By tightly focusing the ultrashort NIR pulse in a sturdy crystal like sapphire, it is possible to broaden the pulse spectrum to cover the entire visible spectrum. Continuum generation is therefore often also called white light generation.

This seed is then amplified in two passes in a BBO crystal in a co-linear geometry. The intense NIR part of the continuum is first filtered out with a dielectric band-pass filter, to avoid any unwanted interaction with the UV pump pulse. Frequency tuning of the output is accomplished by simply adjusting the phase-matching angle of the BBO crystal and the time-delay of the (significantly chirped) seed pulses. Great care is taken to match the spatial overlap of the pump and signal beams, while avoiding other unwanted non-linear processes or damage in the amplifier crystal. The pump and seed are combined and re-separated on either side of the amplification crystal by means of dichroic beam-splitters.

Two mechanical delay stages control the temporal overlap of the pump and signal pulses. To avoid interferometric effects, most prominent in the longer-wavelength operation regime, another spectral filter to block the idler pulse generated in the first pass is used. After the second amplification pass, the spatial mode is smoothed using a small aperture on a beam waist.

The pulse is then re-compressed and spectrally shaped outside the OPA using either a high-dispersion glass prism compressor or grating compressor with an adjustable hard aperture in the usual manner. The pulse duration of the resulting output pulses were optimized as needed by measuring and maximizing up-conversion efficiency in a thin nonlinear crystal.

Figure 2.2 shows the OPA in operation. Here the output has been tuned to the green wavelength range. The beam paths have been drawn for clarity. The bright blue spots are due to scattering from the pump beam. The locations of the second harmonic generation

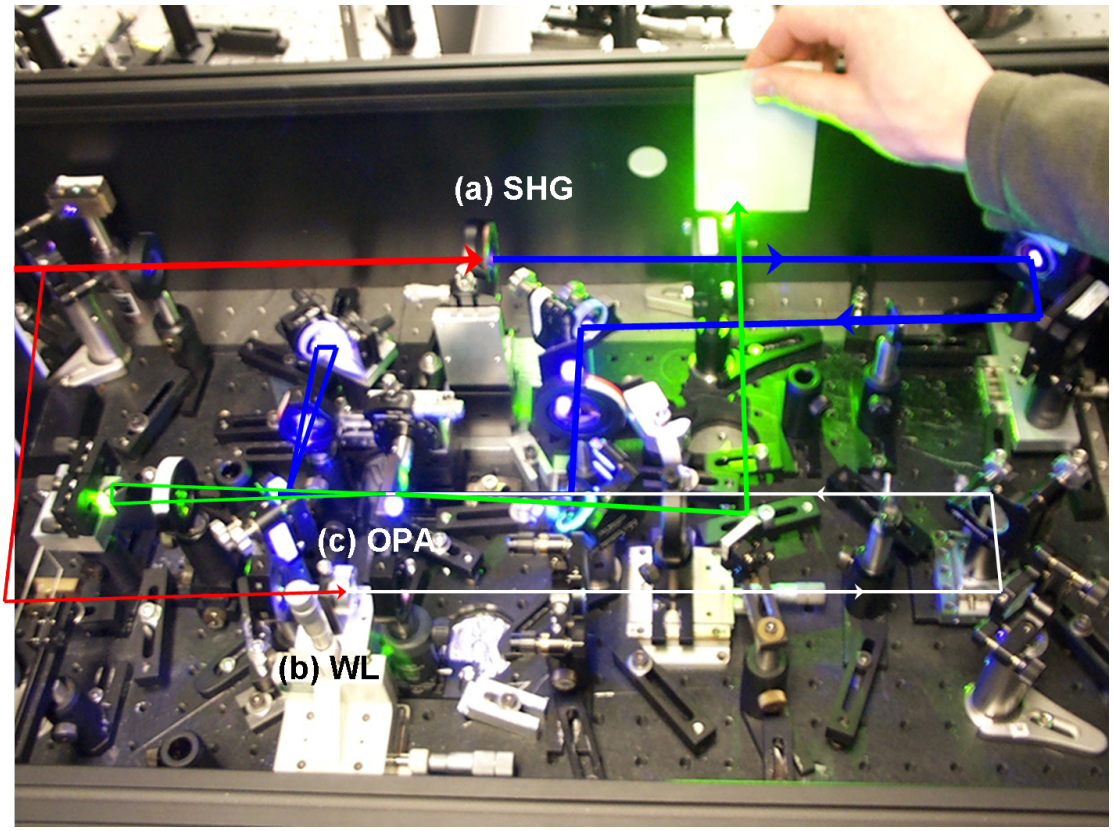

Figure 2.2: A photograph of my custom built visible optical parametric amplifier (tuned to output in the green).

for the pump pulse (a), continuum (or white-light) generation for the seed pulse (b), and parametric amplification (c) crystals are labeled on the photograph.

Figure 2.3 shows a sample of four output spectra. The overall output power is highest when operating at longer wavelengths, thanks to stronger seeding from the continuum and better phase-matching in the BBO crystal. For wavelengths longer than $\sim$ 650 nm, the average power can be over 100 mW. Tuning to less than 500 nm lowers that output to less than 20 mW. After pulse shaping, the pump pulses used in this work typically have average powers of a few milliwatts or less.

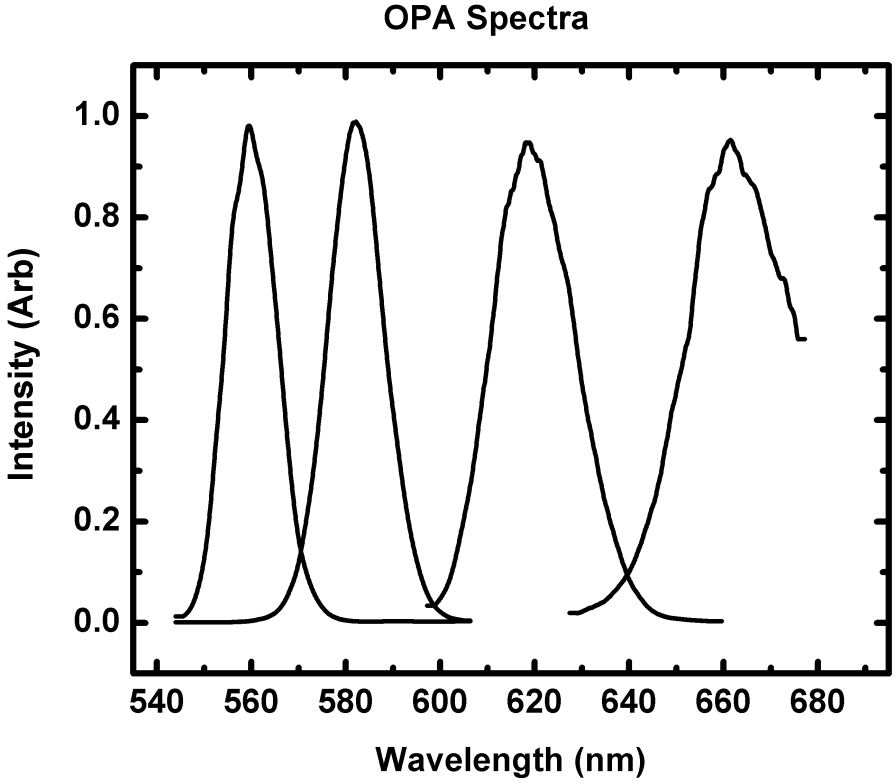

Figure 2.3: Four representative OPA spectra centered at 560, 585, 620, and 660 nm. Typical full-width half-maximum (FWHM) without any spectral shaping is 20-30 nm

2.4 Time domain terahertz spectroscopy

There are two common means of generating and detecting ultrafast optical pulses in the far-infrared: electro-optical crystals and photoconductive switches.[18,19] Photoconductive switches offer higher output power, while electro-optical crystals have the advantage of greater bandwidth.[20–23] To access the spectral ranges studied in this work, electro-optical methods are used exclusively: optical rectification to generate the terahertz pulses, and electro-optic sampling to detect them.

The principle behind optical rectification was briefly described in section 2.1, and is essentially a special case of difference-frequency generation. As an intense laser pulse passes through a crystal with a non-zero (preferably large) $\chi^{(2)}$, the frequency components of the pulse interact. If the phase velocity ($v_{ph} = c/n = \omega/k$) of the terahertz radiation matches the group velocity of the near-infrared (NIR) generation pulse, then the FIR pulse will grow in intensity as it co-propagates through the crystal.[24] The group velocity ($v_g = {}^{dk}/_{d\omega}{}^{-1}$) of the NIR pulse is critical because the nonlinear mixing is intensity driven,

therefore it is the speed of the maximum of the pulse that matters, not the phase of the underlying electric field. In the FIR, however, the electric field must remain in phase with the generation pulse, or else the generated FIR photons may interfere partially, or even totally, diminishing the overall intensity. This condition for achieving constructive rather than destructive interference is thus described by:

$$\frac{k(\omega_{\mathrm{FIR}})}{\omega_{\mathrm{FIR}}} = \left.\frac{\partial k}{\partial \omega}\right|_{\mathrm{NIR}} \tag{2.2}$$

There are two techniques for achieving this velocity matching called quasi-phase-matched and phase-matched.

2.4.1 Quasiphasematched optical rectification

In a non-linear crystal, in this case ⟨110⟩ zinc telluride (ZnTe) or ⟨110⟩ gallium phosphide (GaP), the FIR phase velocity and NIR group velocity are not perfectly matched in general. As a result, as the pulses co-propagate, they "slip" relative to each other in time. The "new" FIR photons being generated are no longer in phase with the earlier ones. If the mismatch continues for long enough, the waves will begin to cancel in amplitude, and the FIR intensity will decrease. Eventually the mismatch passes through 180° and the intensity would begin to grow again. If one imagines varying the length of the crystal, one can see that the FIR intensity upon exiting the crystal would oscillate between maxima and nulls depending on how far the phase had slipped inside the crystal.

In a "quasi-phase-matched" geometry (not to be confused with periodic poling), the thickness of the emitter crystal is carefully chosen so that the pulses exit before they begin to diminish, ideally exactly at the first maxima. Because of the natural dispersion of the crystal, the ideal thickness depends on the desired FIR frequency. The higher the bandwidth desired, the thinner the crystal must be to avoid too much dispersion. The trade-off for this higher bandwidth is lower overall FIR intensity due to the shorter interaction length.

As discussed above, the fundamental limit on the generated terahertz bandwidth is the bandwidth of the NIR laser pulse. The choice of emitter crystal poses a more practical limitation. The TO (transverse-optical) phonon of nonlinear crystals are energetically located in the terahertz range. For ZnTe, the most commonly used emitter crystal for terahertz time-domain spectroscopy, the TO-phonon is located at 5.3 THz, along with weaker acoustic phonons at 1.6 and 3.7 THz.[25] This results in both the obvious FIR absorption, but more importantly creates a strongly dispersive feature in the FIR. For a $Ti{:}Al_2O_3$ laser with a pulse duration of 130 fs, the NIR pulse bandwidth (and therefore the available THz bandwidth) is around 4 THz. Ideally then, the thickness of the ZnTe emitter crystal should be chosen so that its bandwidth is matched, in this case to less than 1 mm. In the THz spectrometer, I use a 500 μm thick ZnTe emitter crystal when studying materials in the spectral range from 0.3 to 3 THz, or roughly 1 to 12 meV photon energy.

As discussed above, however, the amplifier system was modified to operate at pulse durations as low as 42 fs. This significantly raises the upper limit on the potential terahertz bandwidth available, if a suitable nonlinear crystal can be found. A particularly useful crystal is gallium phosphide (GaP). While the $\chi^{(2)}$ of GaP is smaller than that of ZnTe, the higher phonon frequency allows a much wider spectral range of phase-matching. I utilize a 200 μm thick GaP to study the window from around 1 to 7 THz, or about 4 to 30 meV. Practically speaking, this tradeoff means that the signal to noise ratio is at least an order of magnitude smaller in this extended frequency range.

2.4.2 Phasematched optical rectification

It is also possible to exploit birefringent non-linear materials to achieve tunable phase-matching, up to very high frequencies. In this case, the effective index of refraction can be geometrically tuned via the birefringence to match near- and far-infrared propagation at a given frequency. Both ZnTe and GaP are isotropic media where the optical orientation of the NIR and FIR polarizations are determined by the $\chi^{(2)}$ tensor properties. It is not possible to achieve perfect phase-matching in such an isotropic material.[4] Gallium Selenide (GaSe), in contrast, is birefringent and allows phase-matched frequency mixing in the far- and mid-infrared. It possesses an exceptionally large nonlinearity and transparency over a wide range of infrared bandwidth.[26–28]

Phase-matched optical rectification may be understood as difference frequency generation. In a birefringent crystal, the index of refraction is different along one axis (called the extraordinary axis) compared to the other two (ordinary) axes. In type-I DFG phase-matching, the polarizations along an ordinary and extraordinary axis are mixed to produce their difference frequency. For optical rectification, the NIR generation pulse is polarized at 45° so as to provide both the ordinary and extraordinary rays.[27] Figure 2.4 diagrams the geometry. The NIR pulse propagates in the $y-z$ plane of the crystal, where the z axis is the optical axis. The ordinary ray is polarized in the x direction (index n_o), and the extraordinary ray sees an effective index $n_o < n_{eff}(\theta) < n_e$ depending on the phase-matching angle θ about the x axis.

To achieve type I phase-matching for terahertz generation ($o+o \rightarrow eo$), it can be shown that the phase-matching angle θ must satisfy:[4]

$$\frac{\omega_{\mathrm{FIR}}}{\omega_{\mathrm{NIR}}} = \frac{n^o(\omega_{\mathrm{NIR}}) - n^{eo}(\omega_{\mathrm{NIR}} + \omega_{\mathrm{FIR}}, \theta)}{n^{eo}(\omega_{\mathrm{NIR}} + \omega_{\mathrm{FIR}}, \theta) - n^o(\omega_{\mathrm{FIR}})} \tag{2.3}$$

where n^o is the ordinary index of refraction, and $n^{eo}(\theta)$ is the angle-tuned extraordinary index, given by:

$$\frac{1}{n^{eo}(\theta)} = \frac{\sin^2\theta}{(n^e)^2} + \frac{\cos^2\theta}{(n^o)^2} \tag{2.4}$$

GaSe is a micaceous mineral, meaning it cleaves very easily along the $\langle 100 \rangle$ plane, and is very brittle. Unfortunately, this makes it both delicate to work with and impractical to

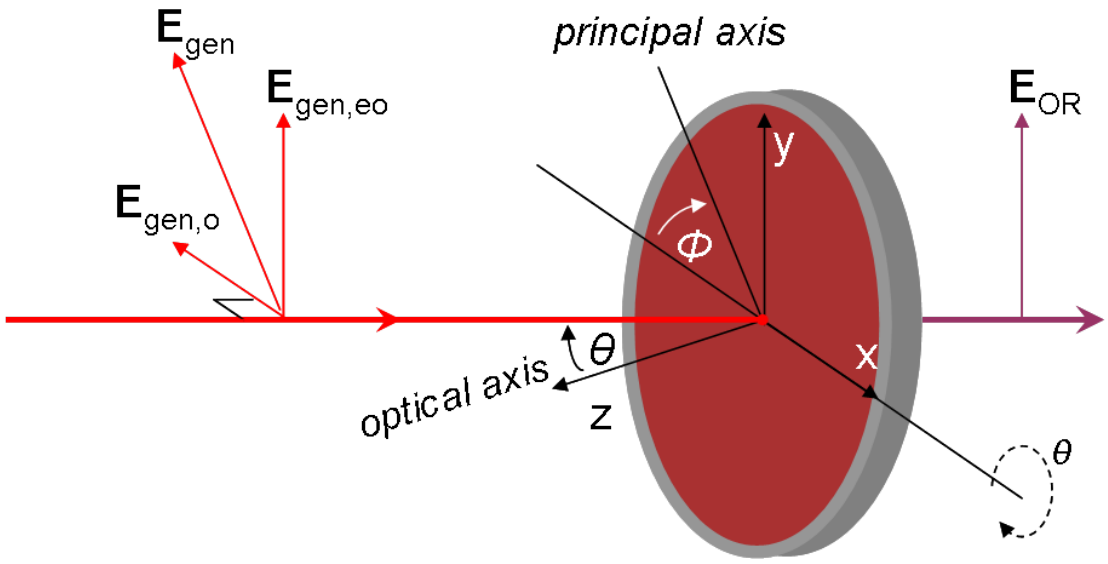

Figure 2.4: Setup for terahertz generation by phase-matched optical rectification in GaSe

cut for a specifically desired phase-matching angle. To achieve phase-matching in the FIR, very large angles ($\theta \approx 45°$) are required, and there can be significant reflection losses at the crystal surfaces. In this work, I have utilized an 80 μm thick GaSe crystal mounted on an MgO substrate for phase-matched terahertz generation at frequencies up to 25 THz ($\theta \approx 45 \sim 50°$).

Figure 2.5 shows examples of the far-infrared probe spectra available from the time-domain terahertz spectrometer. Panel (a) shows the spectrum of a pulse generated and detected in 500 μm thick ZnTe emitter and detector crystals, measured before the upgrade of the oscillator-amplifier system. Panel (b) shows the window available using 200 μm GaP crystals as emitter and detector after the upgrade. Panel (c) shows an example of a pulse attainable using an 80 μm GaSe emitter with a 10 μm ZnTe detector crystal. The phase-matching angle shown was selected to give the broadest overall spectrum, not necessarily the highest possible frequency components. Separation of the THz probe pulse from the NIR generation pulse is accomplished by means of a high-resistivity silicon wafer, chosen for its uniform transmission in the far infrared and strong absorption at the $Ti{:}Al_2O_3$ wavelengths.

2.4.3 Electro-optic sampling

Generating coherent optical terahertz transients for probing samples is of little utility without a sensitive detector. Just as was the case for generation, detection can be accomplished by exploiting either photo-conductive or electro-optical effects, with similar trade-offs. For the applications in this work, I exclusively utilize electro-optic (EO)

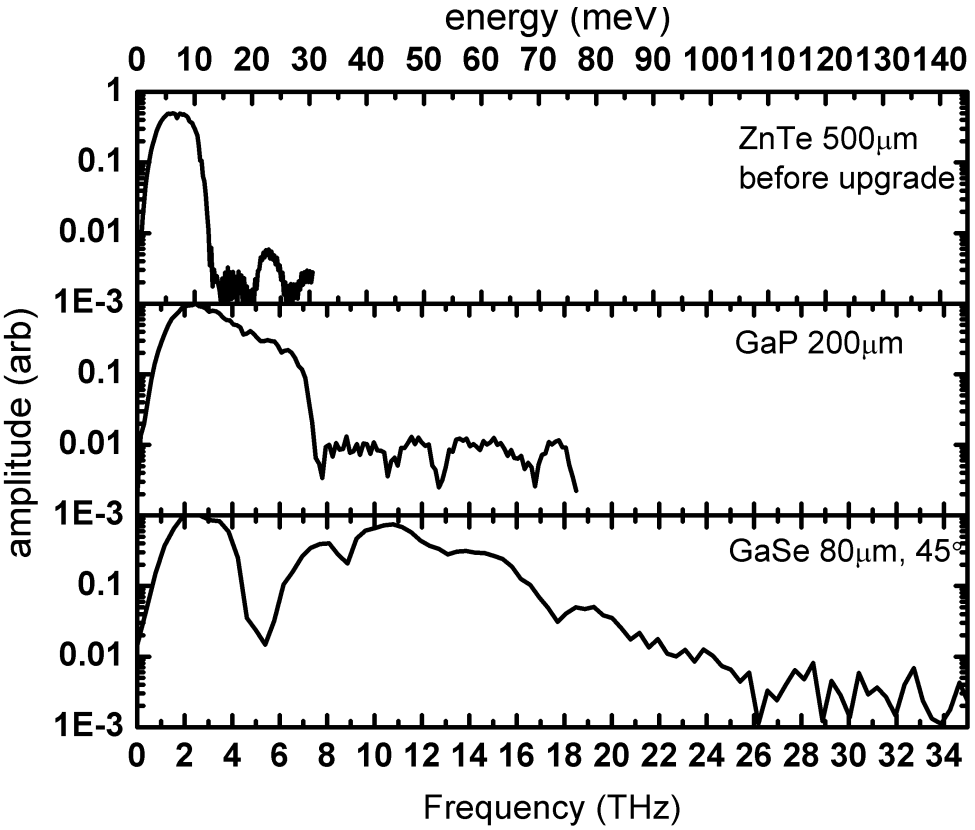

Figure 2.5: THz amplitudes for three different nonlinear crystal emitterdetector combinations: (a) 500μm free-standing $<110>$ ZnTe (both), (b) 200μm $<110>$ GaP on $<100>$ GaP (both), and (c) 80 μm GaSe on MgO emitter with 10μm $<110>$ ZnTe on $<100>$ ZnTe detector.

sampling.

Electro-optic sampling may be most simply understood as an application of the Pockels effect.[29–32] The Pockels effect is a $\chi^{(2)}$ effect in which a change in the index of refraction is introduced proportional to the applied electric field: $\delta n = n^3 r E$. The application of an external electric field thus induces a birefringence in an otherwise isotropic crystal, such as ZnTe or GaP. For free-space THz EO-sampling, the external electric field is the terahertz pulse **E**-field. If a pulse whose duration is short relative to the time-varying electric field is co-propagated through the crystal with the THz field, its polarization will be altered by the induced birefringence. Monitoring the polarization retardation $\Delta\phi$ of the short NIR pulse thus reveals the electric field of the FIR pulse ($\Delta\phi \propto E_{THz}$). By changing the relative delay between the THz pulse and NIR detection pulses, it is possible to trace the evolution of the THz field.

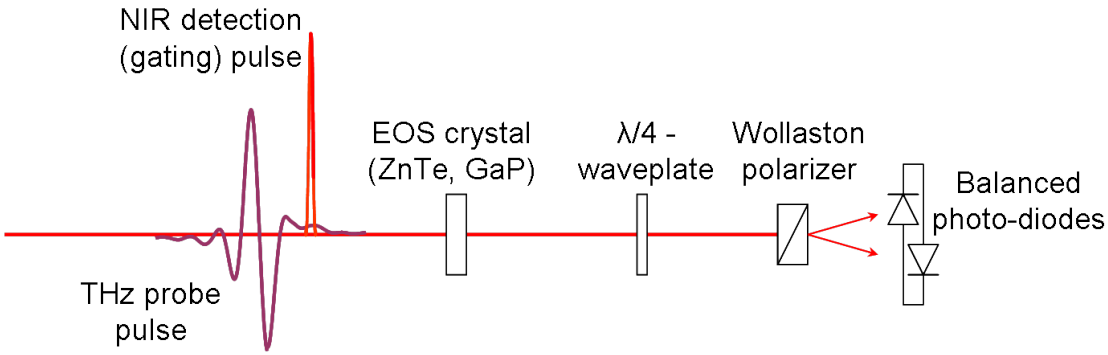

Figure 2.6: A cartoon of the electro-optical sampling (EOS) scheme. The transient THz field is read out by varying the delay between the detection and probe pulses. The balanced diode scheme provides a background free measurement.

As a $\chi^{(2)}$ effect, this scheme must fit into one of the categories discussed above: SHG, OR, DFG or SFG. In fact, this process is quantitatively understood as an inverse of the generation processes described previously. In this case, however, rather than difference frequency generation within a NIR pulse, a NIR detection pulse is up-converted by sum frequency generation with the FIR probe pulse producing a slightly rotated NIR pulse. As such, the same considerations of bandwidth and phase-matching that have been discussed for THz generation (DFG) are again applicable to detection (SFG).[24,33–35]

The time resolution of the detector is limited solely by the duration of the ultrafast detection pulse and by the phase-matching achievable in the EO-sampling detector crystal. It is for this reason that one commonly utilizes pairs of identical crystals for both generation and detection. The exception is for the case of the ultra-broadband measurements which use GaSe as an emitter crystal. In this case, I most often use a very thin (10 μm) ZnTe crystal as the EO-sampling crystal, although it is possible to use a second GaSe crystal as the detector. As a practical matter, the relative ease of the quasi-phase-matched geometry in ZnTe pays off. For a GaSe detector, the phase-matching conditions of the emitter and detector would need to be carefully iteratively optimized for a relatively small benefit each time the THz probe pulse were re-tuned. It is preferable to have a more "‘static" detector, and only tune the emitter as needed.

Practically, detection is accomplished as shown in Figure 2.6. The detection pulse is initially polarized parallel to the THz probe pulse. In the absence of any electric field, this pulse is converted to perfectly circular polarization by the quarter wave-plate to maximize sensitivity and linearize the response. The orthogonal polarization components are then separated by a Wollaston prism and focused on a pair of balanced silicon photo-diodes. Any background imbalance is removed by carefully adjusting the wave-plate.

In the presence of the probe pulse, the gating pulse polarization is rotated to an elliptical polarization by the THz field as they co-propagate through the non-linear crystal. The

polarization components, no longer exactly equal, are again separated by the Wollaston prism and focused onto the diodes. The resulting imbalance between the two polarizations induced by the THz field will read as a net photocurrent. For small angles, this photocurrent is directly proportional to the induced polarization rotation (retardance), and thus the THz electric field. The photo-current is converted to a voltage signal by a low-noise trans-impedance amplifier and measured and recorded by a lock-in amplifier, synchronized to a chopper wheel in the THz generation beam path.

By changing the delay between the THz probe and NIR detection pulse, it is possible to read out the THz electric field as a function of time. The key point is that by directly measuring the *electric field* of the probe pulse, one has immediate access to both the *amplitude* and *phase* changes induced in the probe by the sample material in the beam path. By utilizing this balanced detection scheme, it is possible to measure changes of the THz electric field with signal-to-noise ratios of greater than 10^4, or staggeringly $> 10^8$ in intensity.

The effects of multiple reflections in the crystal (Fabry-Perot interference) can cause significant restrictions on terahertz time-domain measurements. The spectral resolution of the measurement is determined by the overall length of the time window recorded. To achieve a very high frequency resolution it is necessary to measure a very long time window after the pulse. However, for a dielectric slab with a thickness of 100 μm and a FIR index of refraction of 3, the first reflection of the pulse will trail the initial pulse by approximately 2 picoseconds.

The inclusion of this reflection in the measurement can cause a number of difficulties. Failure to properly account for the reflected pulse in modeling the response of the sample creates significant artifacts due to interference. Directly accounting for the reflections, however, is generally impractical. To do so would require that the system be interferometrically stable over time, thanks to the sensitivity of the interference fringing. Even more so, to account for these reflections requires very exact knowledge of the source of the reflection. The faces of the dielectric slab are unlikely to be perfectly parallel, so that the delay may be different from one part of the spatial mode to another. In practice, it is nearly impossible to completely account for these interferometric effects.

Reflections in the beam path, therefore, must be dealt with in the measurement itself. For thin crystals, such as the 200 μm GaP emitter and detection, 80 μm GaSe emitter, or 10 μm ZnTe detector, the crystal is mounted on a much thicker substrate. If the index of refraction is sufficiently well matched, the reflection at the interface can be negligible. For ZnTe and GaP, the solution is to mount the $\langle 110 \rangle$ optically active crystal onto a $\langle 100 \rangle$ substrate of the same material. The result is a small reflection whose effects in data analysis can be ignored. GaSe is mounted on a MgO substrate, which is reasonably well matched. Even more crucial are the reflections within a sample itself. Here, the optical properties of the material may have changed significantly in the time it takes for a reflected pulse to make its round trip. Thus the substrate for a quantum well or other epitaxial film is extremely important. Similarly, the thickness of the low-temperature cuvette created for holding nanocrystals in solution turns out to be a key experimental parameter.

To the extent that one or more of these reflections cannot be sufficiently suppressed or accounted for computationally, they must simply be "windowed" out of the measurement. This imposes a significant restriction on the measurement of sharp spectral features in the terahertz. For the example given above, a reflection trailing by only 2 picoseconds would reduce the measurement resolution to only 0.5 THz if it is necessary to remove it by windowing the pulse in time.

2.5 Pump-probe techniques

In pump-probe spectroscopy, the sample is optically excited with an optical pulse, a.k.a the "pump." Subsequently, a time-delayed pulse probes the time-dependent properties (such as the complex dielectric constant) to determine the sample dynamics. In this work, the pump pulses are either near-infrared or visible pulses shaped to resonantly pump interband transitions. The probes are far-infrared terahertz pulses which explore the internal structure of the pump-generated quasiparticles directly.

The pump-probe technique used extensively in the following chapters is best visualized as a stroboscopic measurement. The sample under test is perturbed away from its equilibrium state, then at a later time, a "snapshot" is taken of its state and compared to the equilibrium. The first key factor is that the "camera flash" be faster (shorter in time) than the lifetime of the change being observed. A typical camera flash is not short enough to "freeze" a bullet passing through an apple, but a high-speed strobe flash is. In these measurements, the strobe is the laser probe pulse, and it must be as fast or faster than the electronic response or relaxation being observed. If not, to stick with this analogy, the picture will be blurry, if you can even see the bullet at all.

Secondly, the perturbation of the sample must relax back to the ground state before the next excitation pulse arrives. Analogizing to the famous apple shot again, it would be as though instead of replacing the apple between shots, one were to keep shooting the same apple over and over again. If the repetition rate of the excitation pulse (time between bullets fired) is shorter than the relaxation time (time it takes to replace the apple), then clearly after the first shot one is no longer taking the same picture.

This is also a key failing of the analogy; in my photographic example, there is no rush to replace the apple between shots. Once a single good picture has been taken, the job is finished. In practice, the picture is very faint and noisy, and so it is repeated over and over again every few microseconds and averaged together. This is why it is important that every picture be as identical as possible save for the noise, which will diminish as one over the square-root of samples averaged. This problem is most often observed as a background signal appearing at "negative" times before the excitation pulse has arrived. The most common example here being a thermal signal resulting from the pump pulse dumping excessive heat into the sample, which takes longer than the available microseconds to dissipate.

Chapter 3

Charge density measurements in $Ga_{1-x}Mn_xP$

In this chapter, I present a study of the equilibrium free carriers density in the hole-mediated ferromagnetic semiconductor gallium manganese phosphide ($Ga_{1-x}Mn_xP$).

3.1 Introduction

In modern information technology, there are two primary tasks to be performed: processing and storage. The technologies used to perform these tasks have diverged along two very different paths: electronic computation and magnetic recording. The silicon transistor, which makes up the backbone of the information superhighway, utilizes the charge of electrons to carry information and perform logical operations. Unfortunately, this technology, while allowing for the performing of tremendously fast calculations, is nearly useless for long term and persistent storage of information. For this reason, recording of information for retrieval at an arbitrary later time has been performed by aligning the spin of electrons rather than utilizing their charge. Naturally occurring ferromagnetism has been a well known and studied phenomenon for centuries and is extremely stable at reasonable temperatures. As computing has taken on an ever larger role in our lives, it is a very natural question to ask why must these two technologies, requiring very different materials and manufacturing processes, remain segregated? Are there efficiencies and benefits to be gained by moving to a paradigm where both the charge and spin degrees of freedom are manipulated together, where processing and storage are merged?

3.2 Gallium manganese phosphide - a ferromagnetic semiconductor

III-V semiconductors have long been of interest to researchers in both academia and industry for their possibilities in band-gap engineering, high mobility, and opportunities in opto-electronics. The discovery that these materials may become ferromagnetic when doped with only a few percent of magnetic ions spurred a burst of new research into the underlying physics and possibilities for application.[36] The most intensively studied material, $Ga_{1-x}Mn_xAs$, has been observed to exhibit ferromagnetic behavior at temperatures up to 170 Kelvin.[37] This is still well below room temperature, and far below the T_C of materials regularly used today in magnetic storage technologies.

One limitation, however, in designing new ferromagnetic semiconducting alloys such as GaMnP is the solubility limit of the heavy Mn ions in the GaP lattice. Beyond a certain limit, attempts to add further Mn content results in the formation of undesired second phases rather than substitution.

In this study, I examine material produced by a process which seeks to circumvent this limitation, called ion implantation and pulsed laser melting (II-PLM), which was pioneered by the Dubon Group at the University of California at Berkeley and Lawrence Berkeley National Laboratory.[38] In this process, manganese ions are implanted into a GaP substrate at densities much greater than the equilibrium solid solubility limit. This results in severe damage to the crystal structure, and the Mn is not substitutionally incorporated into the lattice. Conventional annealing techniques at this point would facilitate the formation of a stable second phase rather than incorporation of Mn into the group-III sublattice. However, by exposing the implanted surface to a very short (nanosecond) laser pulse, the crystal can be briefly melted, allowing the lattice to heal and incorporate the implanted ions. Because the heating is very shallow (nanometers in depth), the excess energy is quickly conducted to the substrate, resulting in a rapid cooling and recrystallization from the substrate back to the surface. In fact, this submicrosecond cooling and regrowth process results in the trapping of Mn in an epitaxial, single-crystalline matrix at levels far in excess of the solid solubility limit. This process allows for the study of these materials and their physics in regimes inaccessible by more traditional molecular beam epitaxy techniques.

As in the prototypical dilute magnetic semiconductor $Ga_{1-x}Mn_xAs$, the ferromagnetic order in $Ga_{1-x}Mn_xP$ is mediated by holes. In both GaAs and GaP, the Mn may replace substitutionally Ga in the lattice in the 3+ oxidation state where it acts as an acceptor. The hole created mediates the ferromagnetic exchange among Mn atoms. In the absence of holes, the direct interaction between neighboring Mn atoms is anti-ferromagnetic.[39]

It may be useful to first discuss the case of $Ga_{1-x}Mn_xAs$. In $Ga_{1-x}Mn_xAs$, the substitutional manganese acts as a relatively shallow acceptor with a moderate binding energy of ~ 110 meV.[40,41] As a result, ferromagnetic $Ga_{1-x}Mn_xAs$ samples show metallic conduction. Their magnetic behavior, however, is very different than in the case of traditional magnetic metals. It is important to note that the manganese dopants play a dual role in this system:

they provide both the localized spins ($\frac{5}{2}$) as well as the delocalized holes. The delocalized holes mediate the long-range interaction between highly localized manganese spins, giving rise to the long-range magnetic order, and are also responsible for electrical conduction.

Compared to $Ga_{1-x}Mn_xAs$, the acceptor levels of the Mn lie much deeper within the bandgap of GaP, forming an acceptor impurity band (~ 0.4 eV above the valence band edge). Because the holes are highly localized, $Ga_{1-x}Mn_xP$ is always non-metallic for $x < 4\%$, in sharp contrast to the GaAs system. So while in $Ga_{1-x}Mn_xAs$ we have delocalized holes mediating the long range ferromagnetic order, in the case of GaMnP this order is mediated by localized holes. This leads to a natural question: what mediates the observed long-range ferromagnetic order, if not delocalized carriers?

Because the Mn acceptor levels in $Ga_{1-x}Mn_xP$ are energetically much deeper than $Ga_{1-x}Mn_xAs$, only hopping transport is possible. In $Ga_{1-x}Mn_xP$, the partially occupied Mn $3d$ orbital (4 electrons while in the 3+ state) is split by the crystal field into a fully occupied doubly degenerate $e_\uparrow$ state and a partially occupied triply degenerate $t2_\uparrow$ state. The exchange interaction between neighboring Mn^{3+} ions involves transfer between the $t2_\uparrow$ states, which is only energetically likely for the case of ferromagnetic ordering. This interaction can be described as the hopping of localized holes in the $t2_\uparrow$ state of the manganese d shell.[42]

3.3 Terahertz transmission of $Ga_{1-x}Mn_xP$

Conventional electrical techniques for measuring carrier concentrations in semiconductors suffer from the need to achieve a good physical contact with the sample. Such measurements are extremely sensitive to the surface of the sample, e.g. they can be affected by a thin insulating layer or other non-Ohmic contact, and the probes themselves may perturb the electronic state of the sample. Depending on the sensitivity of the measurement, these contact effects can dominate over the desired signal. In this study, I apply the techniques of time-domain terahertz spectroscopy to perform a contact-free measurement of the carrier density of GaMnP films.

The sample films of $Ga_{1x}Mn_xP$ studied here were synthesized by II-PLM as described above and in publications of the Dubon group.[43] GaP $\langle 001 \rangle$ wafers were implanted with 50 keV Mn^+ doses of 4.5×10^{15} to 2×10^{16} cm^{-2}. Samples measuring approximately 5 mm on a side were then cleaved along $\langle 110 \rangle$ directions and irradiated in air with a single, spatially homogenized 0.44 J/cm^2 pulse from a KrF ($\lambda = 248$ nm) excimer laser having full width at half maximum (FWHM) of 18 ns. Prolonged etching in concentrated HCl was used to remove a highly twinned layer as well as any surface oxide phases. After processing the $Ga_{1x}Mn_xP$ films have a thickness on the order of 100 nm and exhibit a Mn concentration profile that peaks a few tens of nanometers below the surface. The T_C in these samples was previously observed to be around 50 K.

First, the terahertz pulse is thoroughly characterized propagating in free space as a reference. The amplitude and phase of the oscillating electrical field is sampled as described

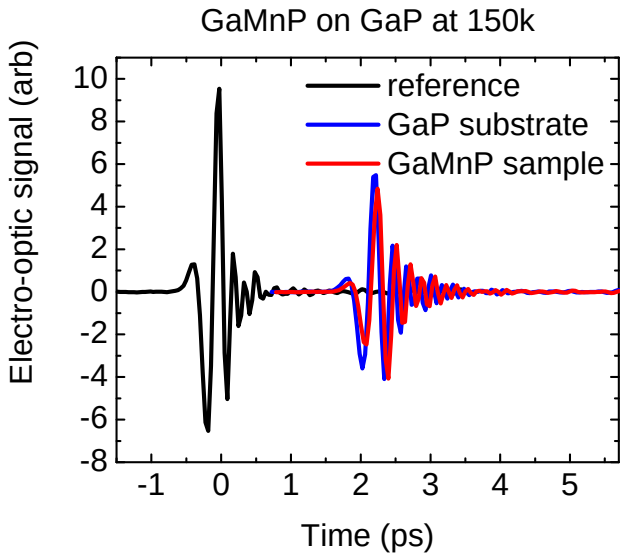

Figure 3.1: THz electric-field transients measured after transmission through vacuum, a GaP substrate, and a GaMnP film on GaP, as indicated. The sample temperature is 150 K.

in section 2.4. The THz transient is then re-measured after being passed through an unprocessed piece of GaP wafer from which the GaMnP samples were made. Finally, the GaMnP on GaP sample is measured. Using knowledge of the sample geometry, it is then possible to directly extract the complex dielectric function of the substrate and then sample films. Figure 3.1 shows an example of these three electric field transients measured at a temperature of 150 K.

These electric field transients are Fourier transformed into the frequency domain and characterized in both amplitude and phase. Figure 3.2 shows the electro-optic signal amplitude as a function of frequency. The probe pulse extends from approximately 0.5 to 3 THz, or 16 to 100 cm^{-1}. The large amplitude drop between reference and substrate measurements is due to the strong surface reflections at the air-GaP interfaces due to the large refractive index of the crystal.

Let us make a few qualitative observations about these transients and spectra before further model analysis. First, there are no sharp spectral features, as evident in the transient (no ringing or dramatic reshaping of the pulse features) as well as the amplitude spectrum. Secondly, thanks to the slight frequency chirp of the probe pulse, I can see that the amplitude decrease between substrate and sample film is more noticeable for the lowest frequency components (earlier times, in the case of the transient). This points to a rather broad low frequency absorption in the GaMnP film.

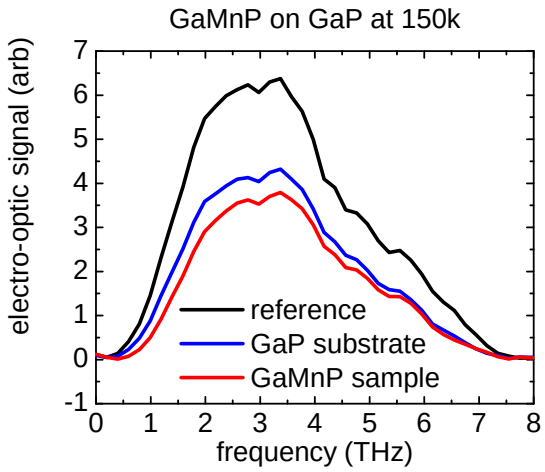

Figure 3.2: Amplitudes of terahertz probe pulse after transmission through vacuum, GaP substrate, and a GaMnP film on GaP substrate.

3.4 Temperature dependence

Using the optically accessible cryostat, the far-infrared transmission was measured over a range of temperatures. As shown in Figure 3.3, the transmission increases with decreasing temperature. For temperatures below 100 K the absorption of the film is too low to accurately distinguish from the substrate.

Because I measure the full transient electric field of the FIR pulse, I can directly calculate the complex optical conductivity over the measurement range without resort to the Kramers-Kronig relation. The sample under test is modeled as a series of two dielectric slabs representing the substrate and film, through which the measured free-space Terahertz pulse is propagated. Figure 3.4 shows the result of the calculation.

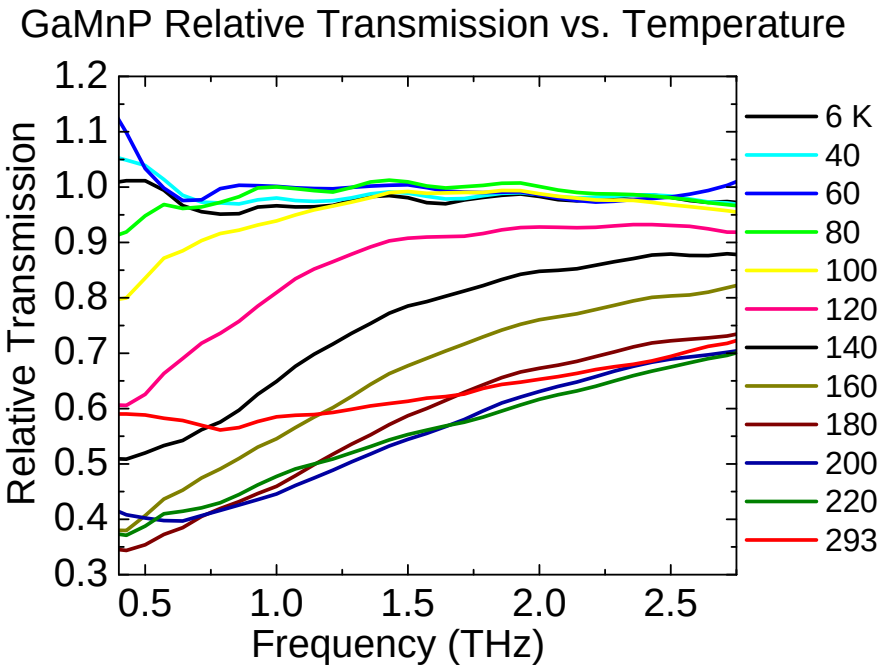

Figure 3.3: Amplitude transmission of GaMnP/GaP relative to the GaP substrate, for different temperatures as indicated.

One should note that while this model treats the $Ga_{1-x}Mn_xP$ film as being uniform with an effective thickness, in reality the implanted manganese has a density distribution as a function of depth. It is possible to attempt to refine this simple model to better account for the density variation over the depth of the film, treating, for example, the carrier density as having a normal distribution. In practice, however, this added computational complexity adds little to the analysis. The overall thickness of the Mn doped film is orders of magnitude smaller than the wavelength of the far-infrared light being used to probe it. The discrepancies between the geometrical models would primarily express themselves as interference effects far outside the measurement window. For the following calculations, I have used an effective thickness of 300 nm based on measurements by the sample grower.

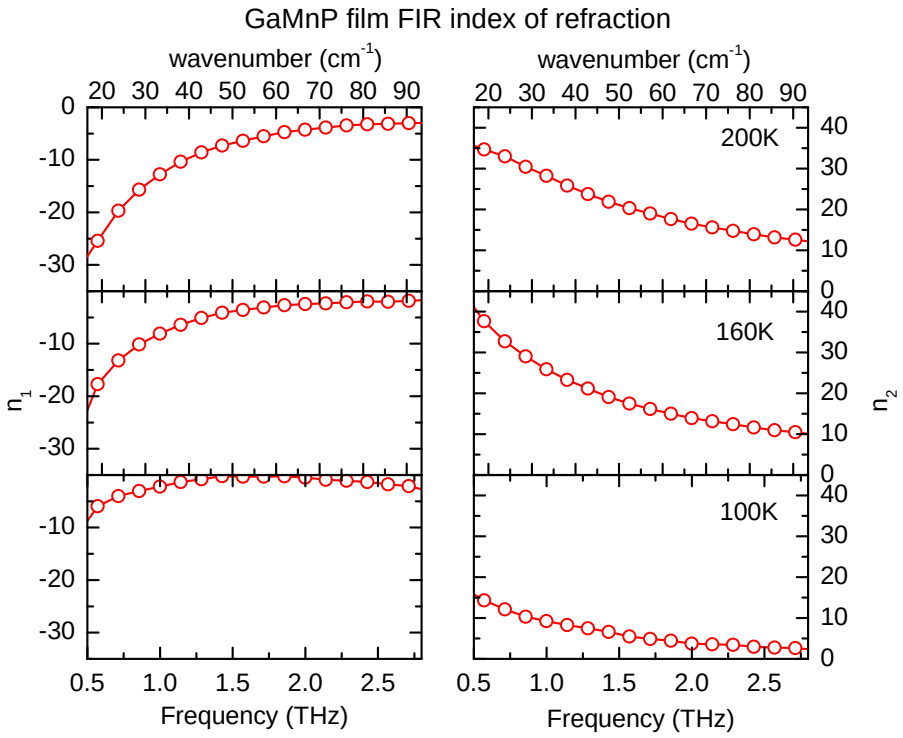

Figure 3.4: Complex refractive index ($n(f) = n_1(f) + in_2(f)$) of the GaMnP film for selected temperatures.

3.5 Modeling

At frequencies below the optical phonon, the far-infrared transmission of gallium manganese phosphide at room temperature is dominated by the presence or absence of free carriers. The optical response of free carriers in a semiconductor can be modeled as a classical electron gas. The primary assumptions of this model, the Drude model, is that there is an average relaxation time by which the system characteristically returns to equilibrium, that is, the zero total momentum state. For an electron gas under the influence of an electric field, this may be stated as:

$$\frac{d}{dt} < \mathbf{p} >= -\frac{< \mathbf{p} >}{\tau} - e\mathbf{E} \tag{3.1}$$

If the external electric field $\mathbf{E}$ is a propagating wave of the form $\mathbf{E_0}e^{-i\omega t}$, then $\mathbf{p} = \mathbf{p_0}e^{-i\omega t}$. Inserting this solution into equation 3.1 and solving for $\mathbf{p_0}$ yields:

$$\mathbf{p_0} = e\tau\mathbf{E_0} \cdot \frac{i\omega\tau}{1 + \omega^2\tau^2} \tag{3.2}$$

This momentum can be readily expressed as a current $\mathbf{J} = \frac{-Ne\mathbf{p}}{m^*}$, and because $\mathbf{J} = \sigma\mathbf{E}$, I

can write down the conductivity:

$$\sigma = \frac{Ne^2\tau}{m^*} \cdot \frac{1 + i\omega\tau}{1 + \omega^2\tau^2} \tag{3.3}$$

where:

- N is the carrier density
- e is the charge of an electron
- m^* is the carrier effective mass
- τ is the relaxation time

This result is a simple Lorentzian centered at zero frequency with a width given by the relaxation time and a zero-frequency amplitude $\sigma_{dc} = \frac{Ne^2\tau}{m^*}$ determined by both the density and relaxation time of the carriers. As discussed in the introduction (section 1.3.1), the area under σ_1 is directly linked to the carrier density and effective mass:

$$\int_0^\infty \sigma_1(\omega)d\omega = \frac{Ne^2}{m}\int_0^\infty \frac{\tau d\omega}{1 + \omega^2\tau^2} \tag{3.4}$$

$$= \frac{\pi}{2}\frac{Ne^2}{m^*} \tag{3.5}$$

$$= \frac{\pi\epsilon_0\omega_p^2}{2} \tag{3.6}$$

where $\omega_p \equiv \sqrt{\frac{Ne^2}{\epsilon_0 m^*}}$ is defined as the plasma frequency.

The least-squares fit of the observed complex index of refraction may be found by varying the plasma frequency ω_p and relaxation time τ. Note because the Drude model only makes statements about the average momentum, one cannot independently fit the density and effective mass of the charge carriers. However, one would expect that the effective mass will have a much weaker temperature dependence than the carrier density. Therefore, I choose to fix the effective mass to the GaP hole DOS effective mass $m_h^* = 0.83m_0$ and use the carrier density N as the fitting parameter. This represents a lower bound on the actual hole effective mass, and thus the fitted carrier density should also be viewed as a lower bound.

As shown in figure 3.5, both real and imaginary parts of the refractive index are extremely well described by this simple model, for intermediate temperatures (100–200 K). At very low temperatures, including temperatures at or below the Curie temperature of the sample, the conductivity of the GaMnP film becomes too small to be observed directly. Above 200 K, I observe a deviation from simple Drude behavior. This is qualitatively observable in Figure 3.3, and corresponds to the deviation from the Arrhenius fit in Figure 3.7.

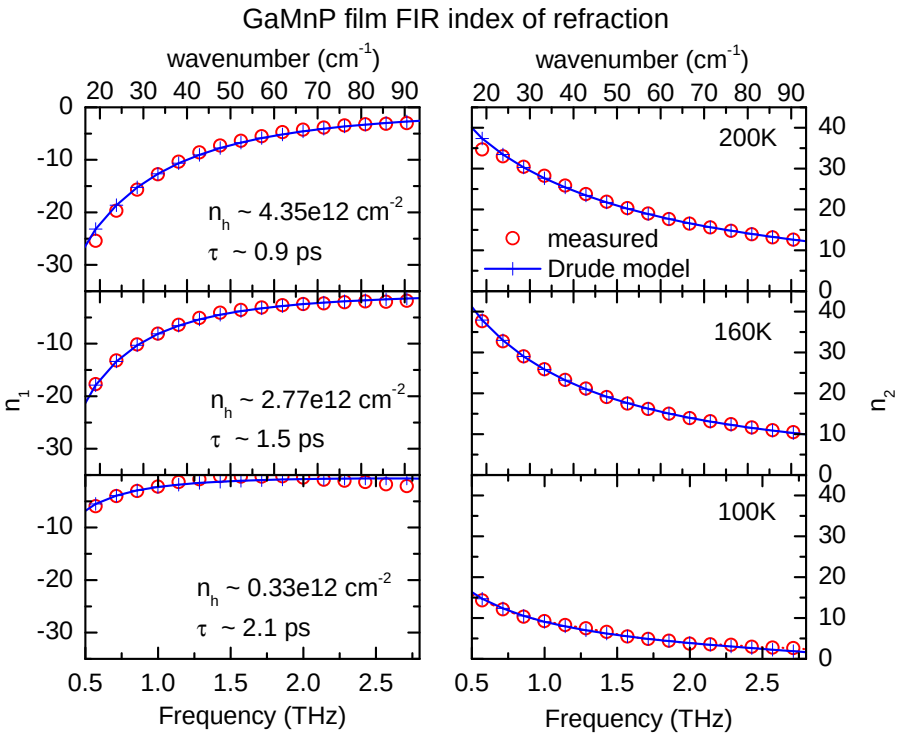

Figure 3.5: Complex refractive index of the GaMnP film with Drude fits.

Figure 3.6 shows plots of the best fit carrier density and relaxation time as a function of temperature. As expected, the mean relaxation time decreases as the lattice temperature increases. The carrier density decreases with decreasing temperature, which can be modeled with an activation energy. Figure 3.7 shows an Arrhenius plot of the carrier density. The slope indicates an activation energy of 42.5 meV.

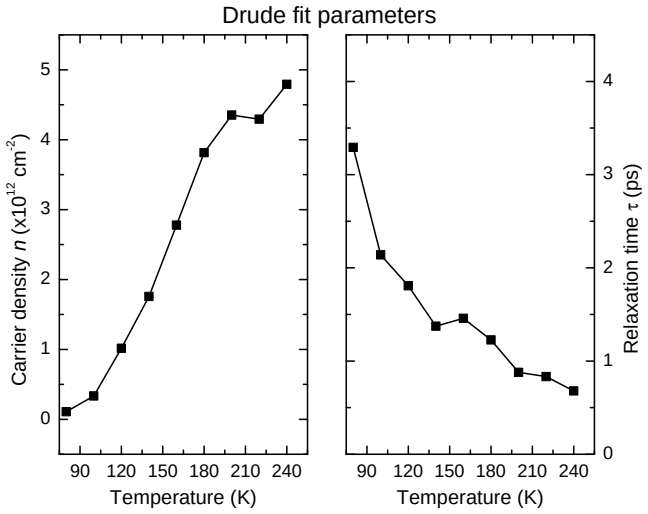

Figure 3.6: Drude fit parameters N and τ as functions of temperature, as obtained from fits to the THz spectra of the GaMnP film.

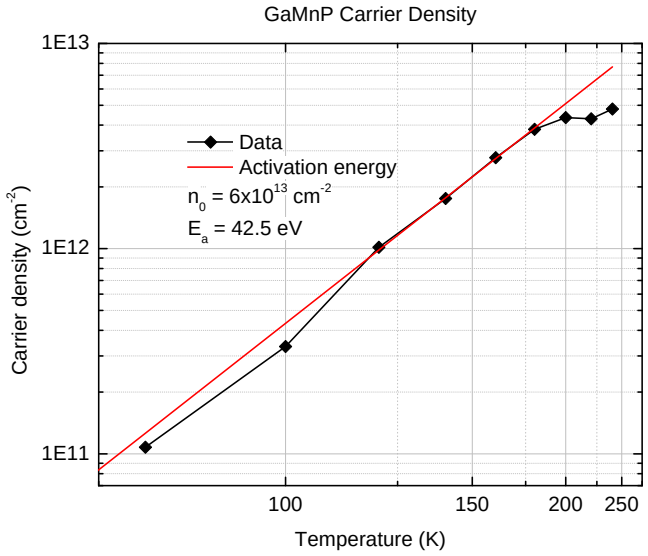

Figure 3.7: Comparison of THz derived carrier densities to a model of thermal activation of carriers in the GaMnP film

3.6 Conclusions

Extrapolating to below the Curie temperature (< 50 K), this predicts a concentration of free carriers within the ferromagnetic film of less than 10^{18} cm^{-3}. This is at least two

orders of magnitude smaller than for a GaMnAs film of similar T_C. The activation energy extracted from these measurements is somewhat larger than measured in sheet resistivity and photo-conductivity experiments ($\simeq$ 31 meV).[44] This activation energy is generally attributable to excitation of holes between the manganese impurity band and the valence band.

In conclusion, contact-free measurements of free carrier concentrations in GaMnP films created by ion-implantation and pulsed laser melting have been performed by time-domain terahertz spectroscopy. I observe insulating behavior at temperatures below T_C, and extract an activation energy of $\simeq 42.5$ meV from the temperature dependence of the carrier concentration. These observations corroborate the picture of ferromagnetism mediated by localized holes in this system.

Chapter 4

Excitons at high densities

In this chapter, I present a study of the dynamics of excitons at high densities, as observed in quantum wells.

4.1 GaAs quantum wells

Gallium Arsenide (GaAs), considered the successor to silicon technology for many years thanks to its superior mobility and potential for extremely high frequency circuit designs, has been an extensively studied material for decades.[45–49] Its band structure and basic properties are very well understood. While silicon has remained firmly entrenched as the overwhelming choice for integrated circuits (thanks in no small part to its oxide, SiO_2), GaAs has ultimately found its own niches. Most important of these have been opto-electronics and band-gap engineering.

Unlike silicon, GaAs is a direct-gap material: the valence band maximum and conduction band minimum coincide in momentum space at the Γ point (zero momentum) in the Brillouin zone. The low temperature energy gap is 1.519 eV. The bands are well described near the Γ point in the effective mass approximation. Conduction band electrons exhibit s-like symmetry, while the valence band is p-like. The optical absorption edge, therefore, corresponds to dipole transitions at the center of the Brillouin zone. Spin-orbit coupling causes two of the six p-like hole states ($|P_{1/2}\rangle = |J = 1/2, m_j = \pm 1/2\rangle$) to energetically "split off" from the remaining four "light" ($|J = 3/2, m_j = \pm 1/2\rangle$) and "heavy" ($|J = 3/2, m_j = \pm 3/2\rangle$) hole states by ≈ 340 meV. The "light" and "heavy" holes are so named for their relative effective masses $\frac{\hbar^2 k^2}{2(E(\Gamma)-E(k))}$, where $E(k)$ is the band energy in the region around the Γ point. The effective mass of the electron is $0.067m_0$, and the (averaged) isotropic hole effective masses are $0.08m_0$ (light-hole) and $0.5m_0$ (heavy-hole).

Extremely high quality gallium arsenide crystals have historically been grown by molecular beam epitaxy (MBE). Thanks to amazing advances in materials science, it is possible to "grow" different layers of semiconductors on a substrate with the precision of a single atomic layer. This has allowed for the creation of entirely new types of materials, where

the composition and properties can be controlled on an unprecedentedly small scale. These heterostructures can have new properties quite different, and in some sense independent of, their constituent parts.

The alloy aluminum gallium arsenide ($Al_xGa_{1-x}As$) has the important properties of being both extremely well lattice-matched to GaAs (to well under 1%) and having a larger bandgap. This means that alternating layers of small and large bandgap semiconductor can be readily grown with an extremely high degree of precision.

By far the most common and important GaAs heterostructure is the quantum well. In this system, a layer of GaAs a few nanometers wide is sandwiched between two AlGaAs barriers, creating a potential well in both the valence and conduction bands. Electrons in the conduction band are confined in the growth (z) direction by the conduction band offsets between AlGaAs and GaAs (ΔE_c). Similarly holes are confined by the valence band offset ΔE_v. If the width of the well (GaAs layer) is sufficiently small (relative to the exciton Bohr radius, for example), the electronic properties can be modified in a number of significant ways.

4.2 Wannier excitons

In semiconductors, the fundamental optical transition is the excitation of an electron across the bandgap, generating an electron-hole (e-h) pair. The oppositely charged quasiparticles are mutually attracted to each other through the Coulomb interaction. The potential is scaled by the (relatively large) dielectric constant of the crystal so that $V = -e^2/(\epsilon r_{eh})$, where ϵ is the dielectric constant and r_{eh} is the spatial separation of the electron and hole. In a bulk semiconductor, this attraction is in many ways directly analogous to the hydrogen atom (or perhaps positronium, which can similarly annihilate), as long as the interaction potential varies slowly compared to the crystal lattice constant. The result is a slowly varying envelope function over the Bloch functions of the constituent quasiparticles. The bound electron-hole pair is called an exciton.[50]

Focusing on a single electron-hole pair, the bound states of this quasiparticle interaction can be described with the hydrogenic picture in the renormalized vacuum of the crystal lattice. The Rydberg is scaled by the reduced mass of the electron-hole pair and the dielectric constant of the crystal. Thus the bound state energies may be written:

$$R_y^* = \frac{\mu}{2}\left(\frac{e^2}{4\pi\epsilon\hbar}\right)^2 \tag{4.1}$$

$$E_n = E_g - \frac{R_y^*}{n^2} \tag{4.2}$$

where E_g is the bandgap and n is the principal quantum number. In bulk GaAs, R_y^* is approximately 4.8 meV, compared to 13.6 eV for hydrogen. This difference in binding energy means that while for hydrogen the Lyman series (transitions to/from the 1s ground

state to higher bound states) occurs in the ultraviolet, the analogous series for a bulk exciton in GaAs is in the far-infrared. Also, it means that excitons in bulk GaAs are thermally ionized at room temperature ($k_BT \approx 25$ meV).

In a quantum well, the interaction between electron and hole is further modified by the quasi-two-dimensional (2D) confinement. In the strict 2D limit, it has been shown that the energy levels are given by the series:[51,52]

$$E_n = E_g - \frac{R_y^*}{(n - 1/2)^2} \tag{4.3}$$

More exact descriptions of excitons confined in quantum wells of finite thickness are described in the literature.[53–58]

This picture assumes, however, that only the electron-hole pair are interacting amidst the background of the crystal lattice. No account for any exciton-exciton interactions is made. Interestingly, excitons are composite bosons, since they are comprised of an even number of fermions.

There has been a tremendous amount of research into cold, dense exciton gases, looking for evidence of Bose-Einstein condensation (BEC). The critical temperature is inversely proportional to the mass of the boson being "condensed." Thus, for excitons, with effective masses orders of magnitude lighter than any atom, the critical temperatures could potentially be as high as a few Kelvin. The opportunity to create a quantum-mechanical system with macroscopic coherence is too exciting to miss, especially given the advanced state of semiconductor manufacturing technology.

The spatial extent of an exciton in semiconductors with a large dielectric constant, such as GaAs, is relatively large, covering many lattice constants. As a result, the interaction of two excitons closer together than roughly a Bohr radius tends to be controlled by the constituent electrons and holes, and thus be fermionic in nature. Also, as the name implies, excitons are themselves an excited state of the crystal. They are generally subject to radiative decay and have relatively short lifetimes. Thus creating a cold, dense excitonic gas obeying Bose-Einstein statistics has posed a great challenge, with multiple claims of experimental success followed by alternative explanations of the observed phenomena.

These questions, among others, have spurred significant interest in the general phase diagram of excitons, even outside the realm of BEC. Figure 4.1 shows a cartoon of the various phases of electron-hole gases in semiconductors. On the far left, in the dilute limit, one expects to observe non-interacting excitons well described in the hydrogenic model.

As the density increases, excitons begin to interact with each other, forming excitonic molecules (called biexcitons, analogous to H_2), and leading to X-X scattering. At sufficiently low temperatures, BEC is the predicted ground state. Finally, when the inter-exciton distance shrinks smaller than the exciton Bohr radius, the hydrogenic picture breaks down, and an electron-hole plasma is observed. At very low temperatures, the plasma may even form electron-hole droplets.

In this work, I seek to explore the transition from a dilute exciton gas to higher densities well away from either BEC or e-h droplets.

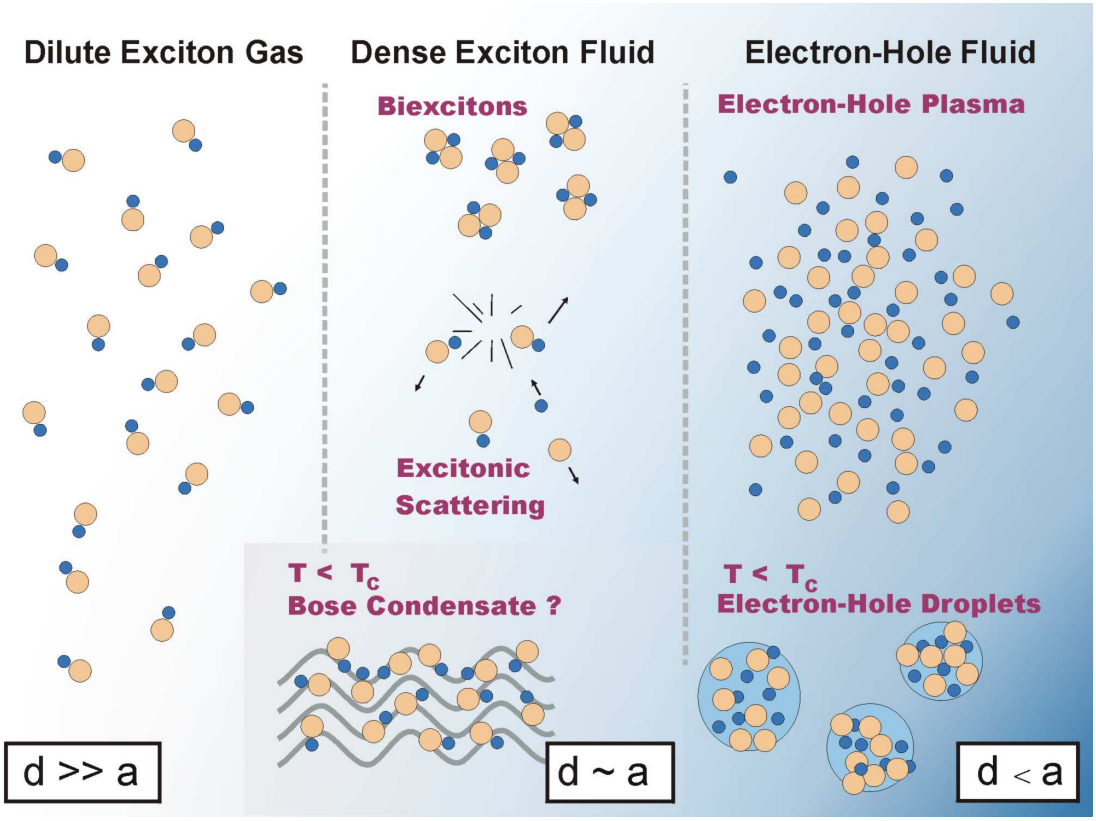

Figure 4.1: Cartoon showing various electron-hole phases in semiconductors (exciton gases and fluids, and electron-hole fluids) with varying inter-particle distance (horizontal) and temperature (vertical).

4.3 Quasi-2D excitons in the dilute limit

Even at small densities, the interaction between photoexcited quasiparticles can be quite complex. The interactions of the excited quasiparticles with each other and with other fundamental excitations of the dense atomic system of the crystal lattice can lead to complex many-body behaviors.

The physics of excitons has been extensively studied using ultrafast optical techniques such as ultrafast NIR pump-probe, time-resolved photoluminescence, and four wave mixing, for example. These techniques, however, are all constrained by momentum conservation to be directly sensitive only to excitons with a negligible center-of-mass momentum. This is because these interband techniques all involve the creation or destruction of an exciton through the emission or absorption of a photon whose momentum is small compared to the Brillioun zone dimension π/a (where a is the lattice constant).

By exploiting the fine structure of the interaction between the quasiparticles, it is possi-

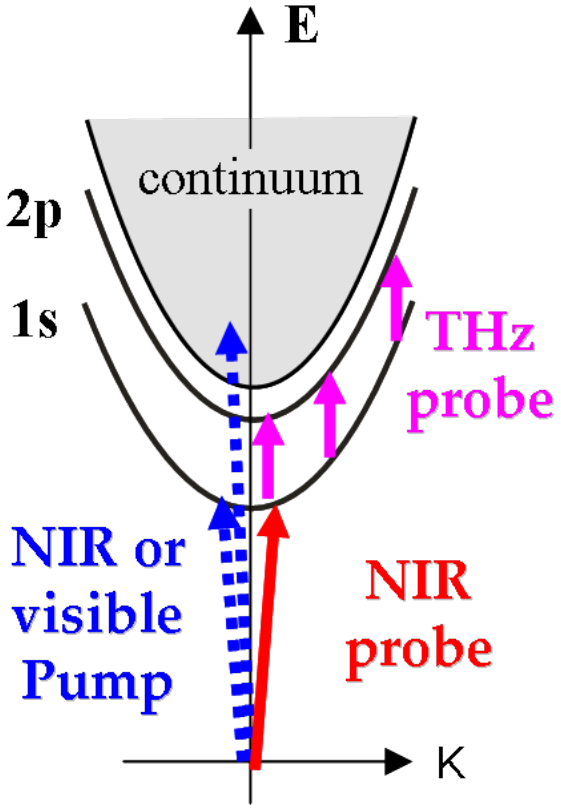

Figure 4.2: Energy dispersion of e-h pairs versus the center-of-mass momentum. Interband optical transitions are restricted to the small cone of center-of-mass momenta around K=0. Internal excitonic transition, on the other hand, are possible for all momentum states of the exciton.

ble to circumvent this restriction. Rather than probing the interband transitions associated with creation and annihilation of excitons, one can probe the internal transitions of the excitons in the far-infrared. This is shown schematically in Figure 4.2. Even for excitons with large center of mass momenta, there is no momentum restriction on exciting the exciton to a higher energy state. This opens up many new opportunities to study low energy excitation dynamics, from the build-up of Coulomb screening in an electron-hole plasma to the study of transient conducting and insulating phases in e-h gases.[59,60]

Figure 4.3 shows an example of the far infrared properties of excitons in this system.[59] The top panels show the real conductivity (left) and real dielectric function (right) of an excitonic gas. The relations between the conductivity and dielectric function were reviewed in section 1.3.1. Because excitons are charge neutral, this gas is insulating, as seen by the real conductivity trending toward zero at zero frequency. The lower panels show a photoexcited electron hole gas at room temperature, where thermal ionization prevents

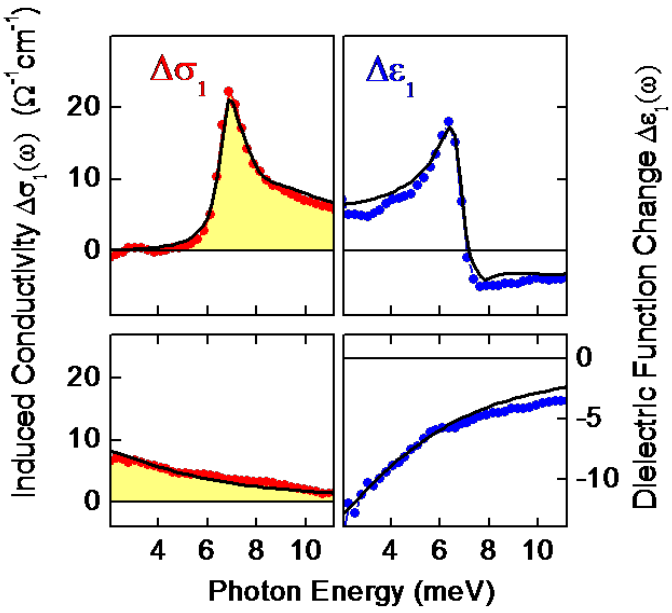

Figure 4.3: Induced complex conductivity of a dilute exciton gas in multiple GaAs quantum wells by Kaindl, et al.[59]

the formation of bound excitons. Here, the data is well described by a conducting Drude model, as one would expect. The insulating and conducting phases are well discriminated in this technique. This demonstrates the power and sensitivity of terahertz spectroscopy to the interaction between the quasiparticles. At low lattice temperatures, a conducting electron-hole gas created by photoexciting e-h pairs into the continuum will cool to form an insulating exciton gas in around 1 ns. It is also important to note that these conducting and excitonic phases are not independent. Even at very early times, the excited electron-hole gas shows evidence of Coulomb correlation between the quasiparticles. The result is a complex evolution of a many-body system toward its excitonic ground state.

4.4 Excitons at high densities

4.4.1 Introduction

For a many-particle electron-hole (e-h) system in a photoexcited semiconductor, density-dependent Coulomb interactions determine the spectrum of its lowest-energy elementary excitations. At sufficiently low densities and temperatures, charge-neutral excitons form whose ground state excitation is the transition from $1s$ to $2p$ levels. These bound states

are modified by many-body effects at high densities.[61] An important phenomenon in this context is the excitonic Mott transition: driven by decreasing interparticle distance, excitonic bound states ultimately cease to exist such that a conducting plasma of unbound e-h pairs prevails.[52,62–64] Quasi-2D excitons in quantum wells, due to large binding energies and sharp optical resonances, are particularly suitable to study high-density many-particle effects of excitons.[65,66]

Numerous studies have investigated the near-infrared excitonic resonances just below the semiconductor band edge, and their broadening, bleaching, and energy shift due to photoexcited e-h pairs.[67–75] Broadening occurs via collisional interactions.[67] The energy shift is more subtle: with increasing density, phase-space filling and screening induce both a renormalization of single-particle states (and thus the band gap) as well as a reduction of the exciton binding energy.[68,69] These two contributions counteract and cancel exactly in the three-dimensional case, where no shift of the exciton line is observed.[70] In quasi-2D systems, a small "blue" or "red"-shift remains depending on the conditions.[71–74] Hence, it is difficult to determine the density dependence of the exciton binding energy from such measurements.

Terahertz (THz) spectroscopy constitutes a fundamentally different approach to study many-particle states. As mentioned above, transitions between internal states of excitons occur in this spectral region, providing a direct measure of exciton densities and binding energies.[76–82] A recent THz study investigated the transient conducting and insulating phases that occur upon formation and ionization of excitons.[80] Furthermore, THz radiation is equally sensitive to the ultrafast dynamics of many-body correlations of unbound e-h pairs.[83] Thus, the interplay between optically generated excitons and unbound e-h pairs becomes directly observable. Until now, however, THz studies investigated a dilute exciton gas, while density-dependent modifications of the pair correlations were not reported.

In the following, I discuss an experiment which employs broadband THz spectroscopy to probe the internal $1s$-$2p$ transition of resonantly photogenerated excitons at high densities.[84] This gives direct access to the low-energy complex dielectric function of the dense electron-hole ensemble. I will show that I observe a strong shift and broadening of the THz exciton resonance with increasing pair density. The response is reproduced by an analytical model that quantitatively determines the densities of excitons and unbound e-h pairs. At high pump powers, excitonic resonances are absent and the response of the system is that of a conducting state. Comparing the THz spectra with the near-infrared response, I find a significantly enhanced energy shift and broadening of the intra-excitonic resonance.

4.4.2 Sample and experiment

The sample consists of a stack of ten undoped 14-nm-wide GaAs wells separated by 10-nm-wide $Al_{0.3}Ga_{0.7}As$ barriers. All measurements are performed at low temperatures ($T = 6$ K). The near-infrared absorption spectrum, shown in Figure 4.4(a), is dominated by the $1s$ heavy-hole (HH) exciton line at 1.540 eV. Its linewidth is 0.8 meV (full width at half maximum, FWHM), pointing to a high sample quality. With increasing energy, the

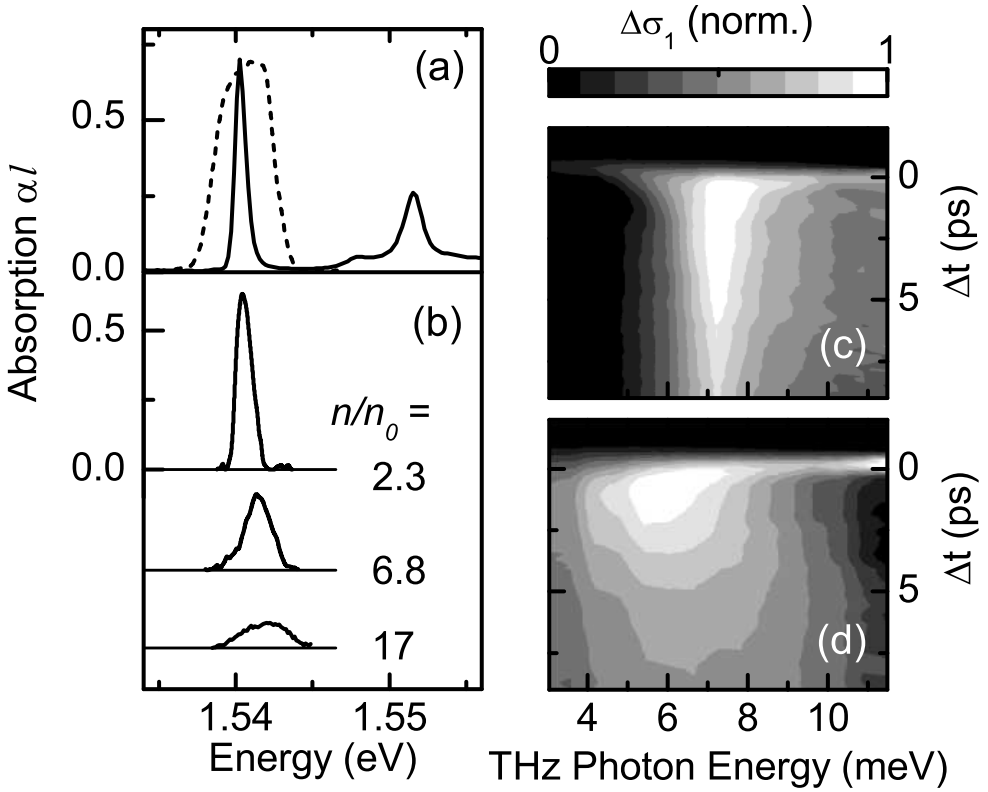

Figure 4.4: (a) Solid line: near-infrared, equilibrium absorption spectrum of the quantum well sample. Dashed curve: spectrum of the pump pulses. (b) Corresponding absorption spectra at delay time $\Delta t = 2.5$ ps after resonant $1s$ HH excitation, for several densities n (where $n_0 \approx 1 \times 10^{10}\text{cm}^{-2}$). The lattice temperature is $T_\text{L} = 6$ K. (c,d) Ultrafast dynamics of the THz conductivity $\Delta\sigma_1(\omega)$ after resonant $1s$ HH excitation for initial pair densities (c) $n \approx 2 \times 10^{10}\text{cm}^{-2}$ and (d) $n \approx 14 \times 10^{10}\text{cm}^{-2}$.

$2s$ HH and the $1s$ light-hole exciton appear, followed by transitions into the band-to-band continuum.

Heavy-hole excitons are excited via spectrally-shaped near-infrared pulses derived from a 250 kHz $Ti{:}Al_2O_3$ amplifier. In order to inject high pair densities, the pump spectrum [dashed line, Figure 4.4(a)] is tailored to a width (4 meV FWHM) distinctly larger than the low-intensity absorption line. This allows for continued overlap as the line broadens at higher densities. Figure 4.4(b) shows absorption spectra for several densities, monitored via near-infrared probe pulses transmitted through the sample after a delay time of $\Delta t =$ 2.5 ps. At elevated pump fluences, I observe broadening, bleaching, and a slight blue shift of the near-infrared $1s$ absorption line. These changes are explained by the joint effects of phase-space filling and screening.[68–74]

To probe the internal response of the bound e-h pairs, I employ broadband THz probe

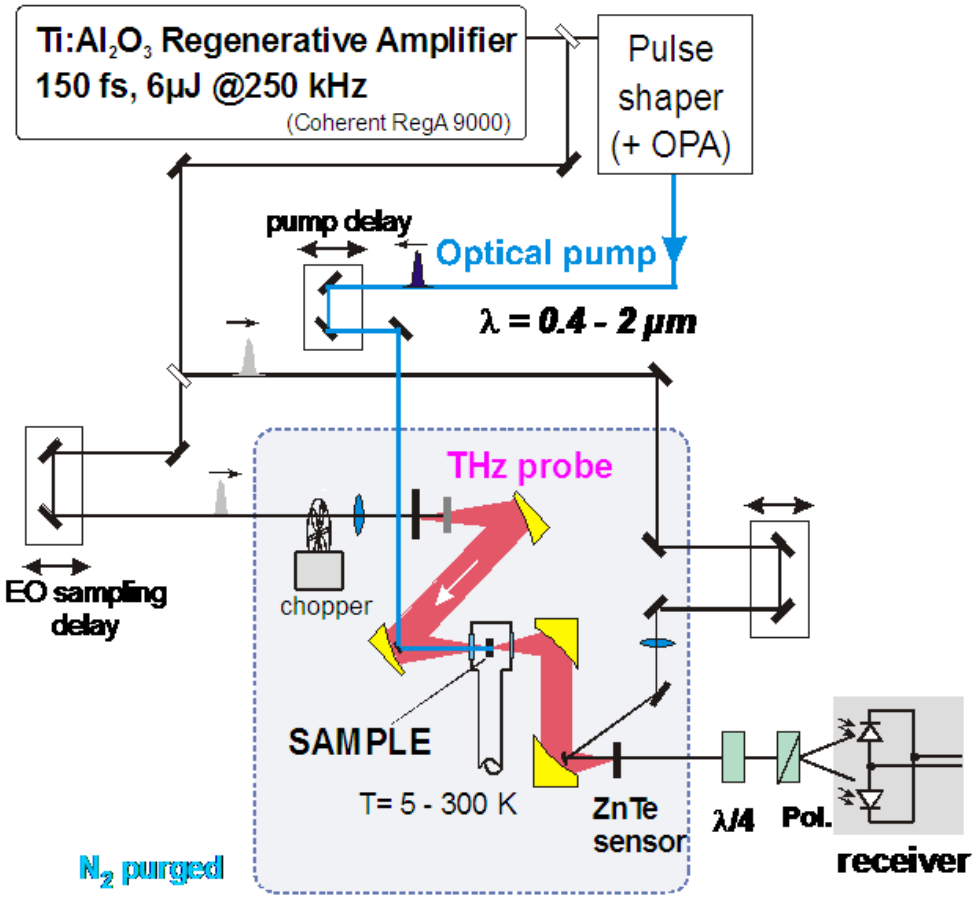

Figure 4.5: A cartoon of the terahertz time-domain spectrometer. The pump is provided by pulse-shaping of the amplifier output. The probe pulse is generated and detected in a pair of ZnTe non-linear crystals.

pulses generated by optical rectification. The experimental setup is sketched in Figure 4.5. The real-time evolution of the THz electric field is detected by electro-optic sampling in a 500-μm-thick ZnTe crystal. I measure both the field transmitted through the sample in equilibrium, and its pump-induced change at a fixed pump-probe delay time Δt. From this, the complex optical conductivity $\tilde{\sigma}(\omega)$ and its transient change is obtained. The retrieval algorithm takes into account the multi-layer quantum well structure.[80] In the following, I will express the full THz dielectric response as $\tilde{\sigma}(\omega) = \sigma_1(\omega) + i\omega\epsilon_0[1 - \varepsilon_1(\omega)]$. The real part of the optical conductivity $\sigma_1(\omega)$ is a measure of the absorbed power density, while the real part of the dielectric function $\epsilon_1(\omega)$ provides a measure of the out-of-phase, inductive response.

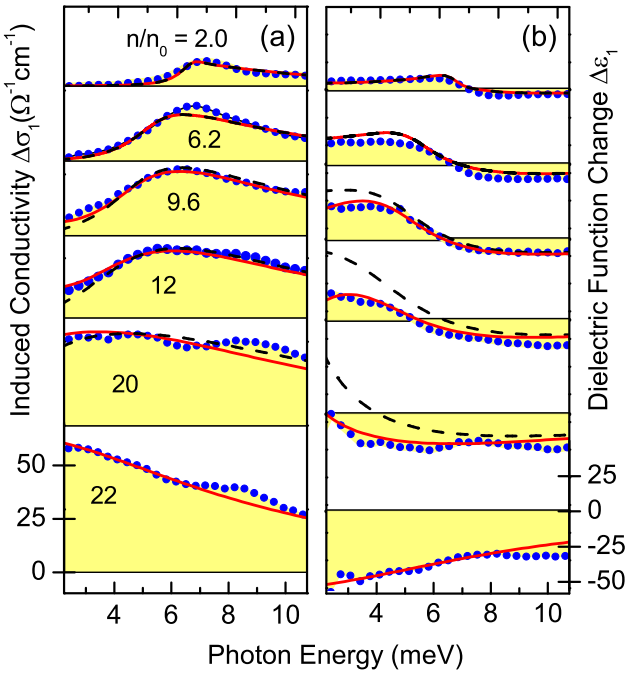

Figure 4.6: Photoinduced THz conductivity spectra $\Delta\sigma_1(\omega)$ [left panels] and dielectric function changes $\Delta\epsilon_1(\omega)$ [right panels] for various excited e-h pair densities n (given in units of $n_0 = 10^{10}\text{cm}^{-2}$). Experimental data (solid dots) are measured at pump-probe delay $\Delta t = 2.5$ ps. Dashed lines: quasi-2D exciton model, solid lines: sum of exciton and Drude components, as explained in the text. At the two lowest densities, the free carriers vanish and the models coincide, while the model curve at the highest density shows a pure Drude response. Curves in each panel are shifted vertically for clarity, and are equally scaled.

4.4.3 Results and observations

Ultrafast transient changes in the THz conductivity $\Delta\sigma_1$ after near-infrared excitation are displayed in Figures 4.4(c,d) as a function of the photon energy of the THz probe pulses and the pump-probe delay time Δt. These data, which are shown for two representative pump fluences, demonstrate a strong density dependence of the THz response. In the following, I will concentrate on features that emerge within the time resolution of the experiment of about 1 ps.

Figure 4.6 shows the THz response (solid dots) for various excitation densities n at delay time $\Delta t = 2.5$ ps. For the lowest density of $n = 2 \times 10^{10}$ cm^{-2}, a narrow asymmetric peak in $\Delta\sigma_1(\omega)$ at $\hbar\omega = 7\,\text{meV}$ demonstrates the existence of bound e-h pairs.[80] The maximum arises from the internal transition from $1s$ to $2p$ bound states, while the high-energy shoulder corresponds to transitions from $1s$ into higher bound and continuum states.

The conductivity vanishes at low frequencies, which corroborates the insulating nature of this dilute exciton gas. The dispersive zero crossing of $\Delta\epsilon_1$ at a photon energy of 7 meV is characteristic of the well-defined intra-excitonic oscillator.

With increasing excitation density, three profound changes occur in the THz response as revealed in Figure 4.6: (*i*) The area enclosed by the conductivity curve $\Delta\sigma_1(\omega)$ increases, while the near-infrared exciton line shown in Figure 4.4(b) bleaches. Thus, with rising excitation density, oscillator strength is increasingly transferred from interband to intraband transitions. (*ii*) The width of the observed THz features strongly increases. (*iii*) Both the spectral maximum of $\Delta\sigma_1(\omega)$ and the zero crossing of $\Delta\epsilon_1(\omega)$ shift to lower frequencies. At the highest excitation density, the conductivity rises monotonically towards lower frequencies and a zero crossing of the dielectric function is not observed. This behavior is indicative of a conducting phase in the absence of excitonic resonances.

4.4.4 Two-component model analysis

For a quantitative analysis, I model the experimentally determined THz response (Figure 4.6) via the low-energy dielectric function of two-dimensional excitons

$$\epsilon_{\mathrm{X}}(\omega) = \epsilon_\infty + \frac{n_{\mathrm{X}} e^2}{\epsilon_0 m} \sum_q \frac{f_{1s,q}}{(\omega_{1s,q}^2 - \omega^2) - i\omega\Gamma_{\mathrm{X}}} \tag{4.4}$$

where ϵ_∞ and ϵ_0 are the background and vacuum dielectric constants, respectively, and e and m are the elementary charge and the reduced exciton mass. The oscillator strengths $f_{1s,q} = (2m\omega_{1s,q}/\hbar)|\langle\psi_{1s}|\mathbf{r}|\psi_q\rangle|^2$ for internal transitions from $1s$ to higher bound and unbound states are calculated using two-dimensional exciton wavefunctions ψ_i.[85,86] I vary the exciton density n_{X}, the energy position $E_{1\mathrm{s}\rightarrow 2\mathrm{p}} = \hbar\omega_{1\mathrm{s},2\mathrm{p}}$, and the phenomenological exciton broadening parameter Γ_{X} to fit the measured conductivity curves. The results are shown as dashed curves in Figure 4.6.

At low densities, good agreement with the experimental THz response is obtained. With increasing pump power, however, the model does not simultaneously reproduce both $\Delta\sigma_1$ and $\Delta\epsilon_1$. For parameters that optimally fit the measured conductivity (dashed lines in Figure 4.6), the corresponding model $\Delta\epsilon_1$ deviates strongly from the experimental result. These problems can be resolved by considering additional low-frequency spectral weight, in the form of a coexisting plasma of unbound *e*-*h* pairs. The response of this two-component system is obtained by adding a Drude term to the dielectric function ϵ_{X} of Eq. 4.4:

$$\epsilon(\omega) = \epsilon_{\mathrm{X}}(\omega) - \frac{n_{eh} e^2}{\epsilon_0 m} \frac{1}{\omega^2 + i\omega\Gamma_D} \tag{4.5}$$

where n_{eh} is the density of unbound *e*-*h* pairs, and Γ_D is a phenomenological scattering rate. By including such unbound pairs, excellent agreement with the experiment is obtained even at high densities (solid curves in Figure 4.6). The optimum values of the parameters are constrained by the different spectral responses of excitons and unbound *e*-*h* pairs, and by

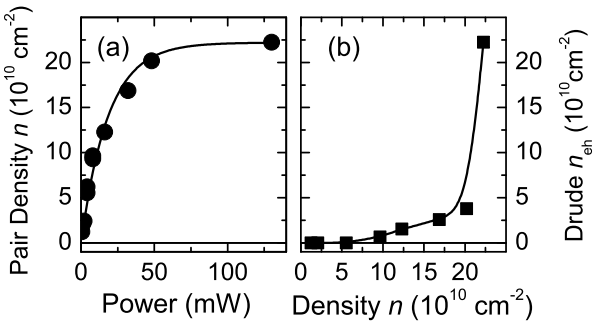

Figure 4.7: Pair densities from the two-component model explained in the text. (a) Total excited pair density as a function of pump power. (b) Free carrier density as a function of the total pair density. Lines are a guide to the eye.

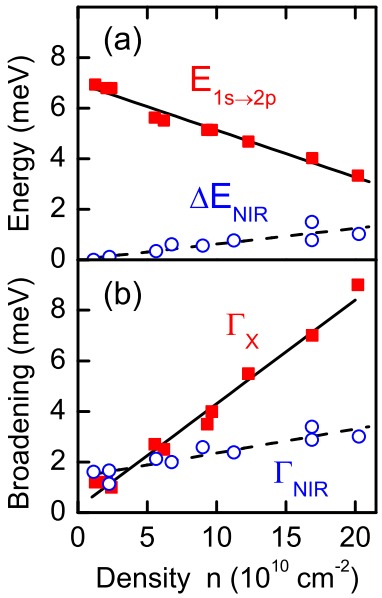

Figure 4.8: (a) Excitonic level spacing $E_{1s\rightarrow 2p}$ (filled squares) measured via THz spectroscopy, and density-induced energy shift ΔE_{NIR} (open circles) of the interband resonance. (b) Width Γ_{X} (filled squares) of the intra-excitonic $1s \rightarrow 2p$ resonance as fitted via the two-component model of Eq. 4.5, corresponding to the solid curves in Figure 4.6. Open circles: width Γ_{NIR} (FWHM) of the near-infrared band edge absorption. Solid and dashed lines: linear fits to the data.

the requirement to reproduce both functions, $\Delta\sigma_1(\omega)$ and $\Delta\epsilon_1(\omega)$, simultaneously and over a broad spectral range.

The resulting fit parameters reveal details in the evolution of the complex many-body system with increasing excitation density. Figure 4.7(a) shows the total density $n = n_X + n_{eh}$ of excitons and unbound e-h pairs as a function of the pump power. Clearly, a strong saturation at high powers is observed as expected due to bleaching of the near-infrared $1s$ HH line. In the dilute limit, the pair densities can also be estimated from the pump powers (linear near-infrared response). These values agree to within 50% with n obtained from the THz model. In Figure 4.7(b), I plot the density of unbound e-h pairs as a function of the total pair excitation n. At lower densities ($n < 5 \times 10^{10}$ cm^{-2}), only excitons are generated. With increasing n, the population share of unbound carriers becomes more significant. Beyond a critical density $n_C \approx 2 \times 10^{11}$ cm^{-2}, photoexcitation results primarily in a population of unbound e-h pairs. An excitonic resonance is absent and the THz response can be fully explained by a Drude model alone.

4.4.5 Discussion and conclusion

I emphasize that the transition observed here cannot be unambiguously identified with a Mott transition driven purely via decreasing inter-particle spacing. Rather, at the highest densities the near-infrared exciton line broadens and shifts, leading to an intrinsic merging with the continuum and thus a simultaneous photoexcitation of unbound carriers. Nevertheless, n_C compares well to values of the Mott density deduced from excitonic and interband photoluminescence after nonresonant excitation.[64] The THz spectra in Figure 4.6 underscore the utility of low-energy probes to study the crossover between insulating and conducting phases of e-h pairs, pointing the way towards THz studies of purely density-driven Mott transition phenomena.

A key aspect of this study concerns the renormalization of the excitonic fine structure with increasing photoexcitation density. Figure 4.8 illustrates the changes in resonance energy and scattering rate, via direct quantitative comparison between the THz and the near-infrared response. It shows (filled squares) the energy $E_{1s\rightarrow 2p}$ and width Γ_X of the THz exciton transitions. These curves reveal a striking red-shift and broadening that occurs in the $1s$-$2p$ intra-excitonic oscillator with increasing density. For comparison, the energy shift of the near-infrared $1s$ HH resonance is also indicated [open circles, Figure 4.8(a)]. The net shift is given by the counteracting effects of band gap renormalization and reduced exciton binding energy–its interpretation is thus elusive and requires model assumptions. In contrast, the intra-excitonic transitions observed here at THz frequencies are unaffected by bandgap shifts, and directly gauge the weakening of the binding energy.

From the near-infrared $1s$ HH absorption band one may evaluate the width Γ_{NIR} as a function of the excitation density [circles in Figure 4.8(b)]. In addition to the spectrometer resolution, the finite optical thickness of the sample leads to a slight inhomogeneous broadening. The measured values of Γ_{NIR} are, however, a good upper bound for the width of the $1s$ HH resonance. The density-dependence is well fitted by the relation $\Gamma_{NIR}(n) = \Gamma_0 + \gamma_{NIR} n$ [dashed line in Figure 4.8(b)] with $\gamma_{NIR} = 1.0 \times 10^{-11}$meVcm^2, in quantitative agreement with literature values.[67] Remarkably, the density-dependent broadening of the THz re-

sponse $\gamma_{\mathrm{X}} = 4.1 \times 10^{-11}\mathrm{meVcm}^2$ (solid line) is about four times larger. I suggest that this results from enhanced sensitivity of the $2p$ exciton, not visible in near-infrared spectra, to screening and scattering: its radial extent (expectation value $\langle r_{2p} \rangle = 58\,\mathrm{nm}$, obtained from the exciton model in the dilute limit) is six times that of $1s$ excitons. The combination of near-infrared and THz probes allows for a first direct observation of this enhancement.

In conclusion, in this chapter I have discussed broadband terahertz studies of a high-density exciton gas in GaAs/AlGaAs multiple quantum wells. With increasing excitation density, the far-infrared complex conductivity of this many-body system reveals a distinct red-shift of the intra-excitonic $1s$-$2p$ transition and a strong broadening of the $2p$ bound state, finally leading to the disappearance of the resonance. THz spectroscopy thus provides a direct gauge of bound and unbound pair densities, and enables the observation of the excitonic fine structure as it evolves under high-density conditions. Beyond the scope of this dissertation, this approach may prove valuable in future studies of dense spatially-indirect excitons or interactions of strongly confined carriers in quantum dots.

Chapter 5

Stimulated terahertz emission from internal exciton transitions

5.1 Introduction

As discussed in previous chapters, excitons are often seen as the low-energy counterpart of the hydrogen atom. This picture has been successfully invoked to describe the complex many-body problem of a photoexcited semiconductor in the dilute limit.[52,87] The analogy to atoms has also motivated the search for macroscopically ordered states and Bose-Einstein condensation of excitons in two-dimensional nanostructures[88] or bulk cuprous oxide (Cu_2O).[89,90]

Nevertheless, there are significant limitations to the atomic-like description of excitons. These quasiparticles are complex many-body states embedded in the background of a crystal lattice, which interact via scattering, phase-space filling, and screening. They generally exist in a mixture with unbound charge carriers. Unlike atoms, excitons are transiently photogenerated, associated with an initial interband coherence, and unstable due to recombination. Testing the concept of excitons has thus been an important focus in semiconductor physics.[66]

Most of the spectroscopic information has been extracted from optical techniques probing interband transitions. However, such experiments provide only indirect access to the internal exciton structure. A most direct approach to investigate intra-excitonic absorption requires studies in the mid to far infrared spectral domain.[59,90,91] In recent years, various sources for terahertz (THz) radiation have been developed.[92] THz spectroscopy has evolved into a powerful tool for probing low-energy excitations in semiconductors with ultrafast temporal resolution.[59,60,93,94] As I have discussed earlier, absorption of THz photons promoting ground state excitons into higher bound energy levels was used to explore exciton formation.[59] The previous chapter showed how the low-energy response, including the intra-excitonic absorption, evolve with increasing phase space filling in GaAs quantum wells.

Theoretical studies suggest how the underlying elementary quantum processes could be effectively reversed to induce THz gain from an inverted exciton population.[95,96] However, nonradiative relaxation of the excited states to the lowest bound exciton level by ultrafast scattering with phonons, excitons, and free carriers are expected to occur. These processes, in addition to THz absorption into bound states and the continuum, can strongly compete with stimulated emission and are poorly understood. Up to now, emission of electromagnetic radiation connecting internal exciton levels has not been observed.

In this chapter, I present the first direct observation of stimulated emission of electromagnetic radiation from intra-excitonic transitions. After resonant photoexcitation of $3p$ excitons in the semiconductor Cu_2O, I use broadband THz pulses to induce internal dipole transitions to the $2s$ state. This process manifests itself via a negative change of the absorption coefficient at the resonant photon energy of 6.6 meV. Incoherent population inversion and coherent resonant Raman scattering both contribute to this effect. Furthermore, I observe significant THz emission at the same photon energy when the visible pump pulse covers both dipole-active $3p$ and optically-dark $2s$ states.

5.2 Excitons in cuprous oxide

Cuprous oxide, despite being one of the earliest known semiconductor materials, has remained a subject of intense research interest up to the present. The reason is the unusual opto-electronic properties of the crystal: because the valence and conduction band have the same parity, optical (dipole) transitions are forbidden. Additionally, the exciton is very tightly bound ($R_y^* \sim 130$ meV) and thus quite stable against thermal ionization. This results in an unique opportunity to study a well defined exciton series with an extremely long lived ground state. Many groups have studied and manipulated this system in search of a Bose-Einstein condensate of excitons, as well as other studies of the quantum optics of excitons.[97–100]

Unlike the case of GaAs, the highest quality crystals of cuprous oxide have traditionally been found in nature. In natural Cu_2O crystals, lifetimes of the lowest energy excitonic state have been observed to be on the order of microseconds at low temperature.[101] In contrast, the lifetime of excitons in GaAs quantum wells is around a nanosecond.[59]

The bandgap minimum of Cu_2O occurs at the Γ point and is direct. As mentioned above, both the valence and conduction bands have positive parity, leading to the first single-photon absorption being the odd parity exciton states. Figure 5.1 shows an example of (a) linear absorption and (b) two-photon absorption spectra of cuprous oxide. In the study presented here, I will be concerned primarily with the $3P$ and $2S$ states of the so-called "yellow" series of excitons. There exist several higher energy excitonic series associated with higher energy valence and conduction bands, of which the $1S$ "green" peak visible in the plot is a member.

Direct one-photon access to the P excitons makes Cu_2O an ideal system to search for THz stimulated emission. One can immediately create excitons in an excited state by

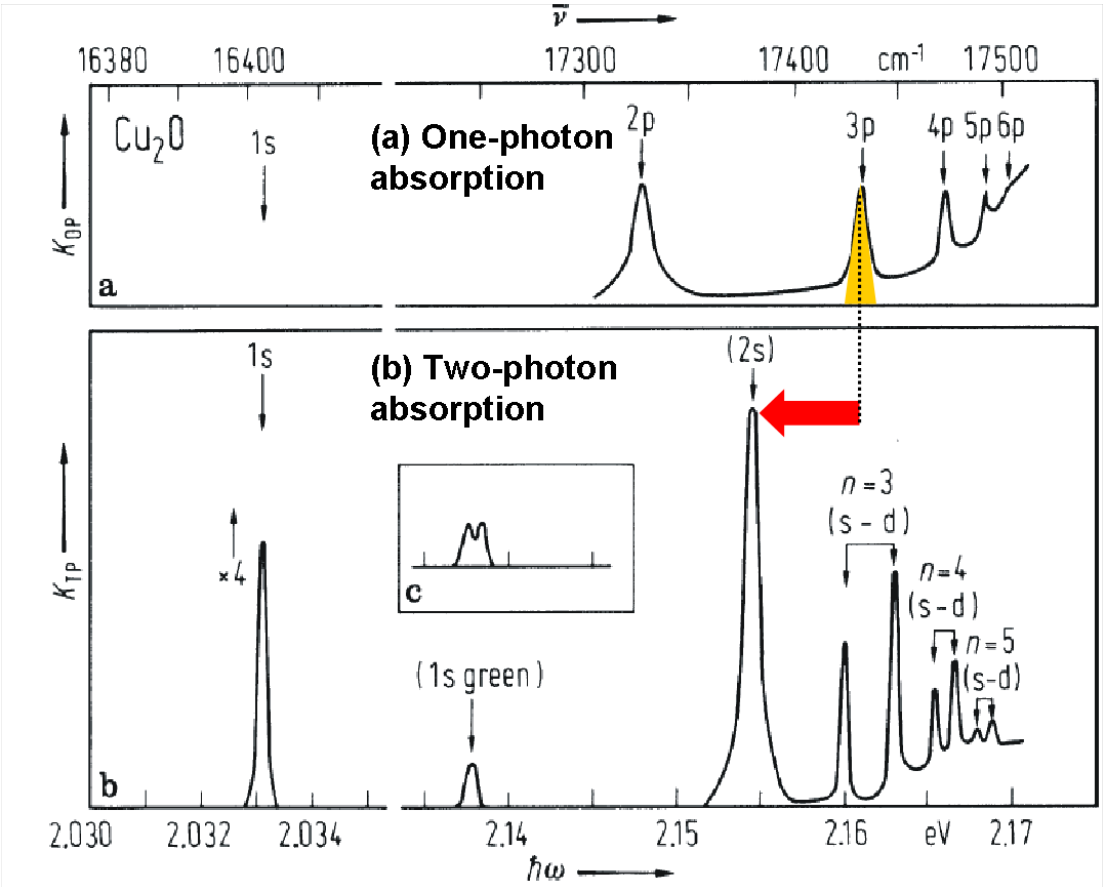

Figure 5.1: Low temperature one- and two-photon absorption spectra in Cu_2O, from literature.[102] Only the p states are accessible by linear absorption. The large binding energy of the exciton is also evident.

one-photon absorption and probe the downward transition with a THz photon. In GaAs quantum wells, by contrast, only the S excitonic states are available, making the control of the excitonic population for this search far more challenging to the point of impracticality.

5.3 Stimulated emission from internal transitions

5.3.1 Sample and experiment

All experiments are performed at low temperature ($T = 6$ K) in a 330-μm-thick, high-quality Cu_2O crystal. The visible absorption spectrum (Figure 5.2) is dominated by a series of sharp lines originating from the $2p$, $3p$, $4p$, and $5p$ excitons (yellow series), followed by the continuum of unbound states. Owing to the positive parity of the valence and con-

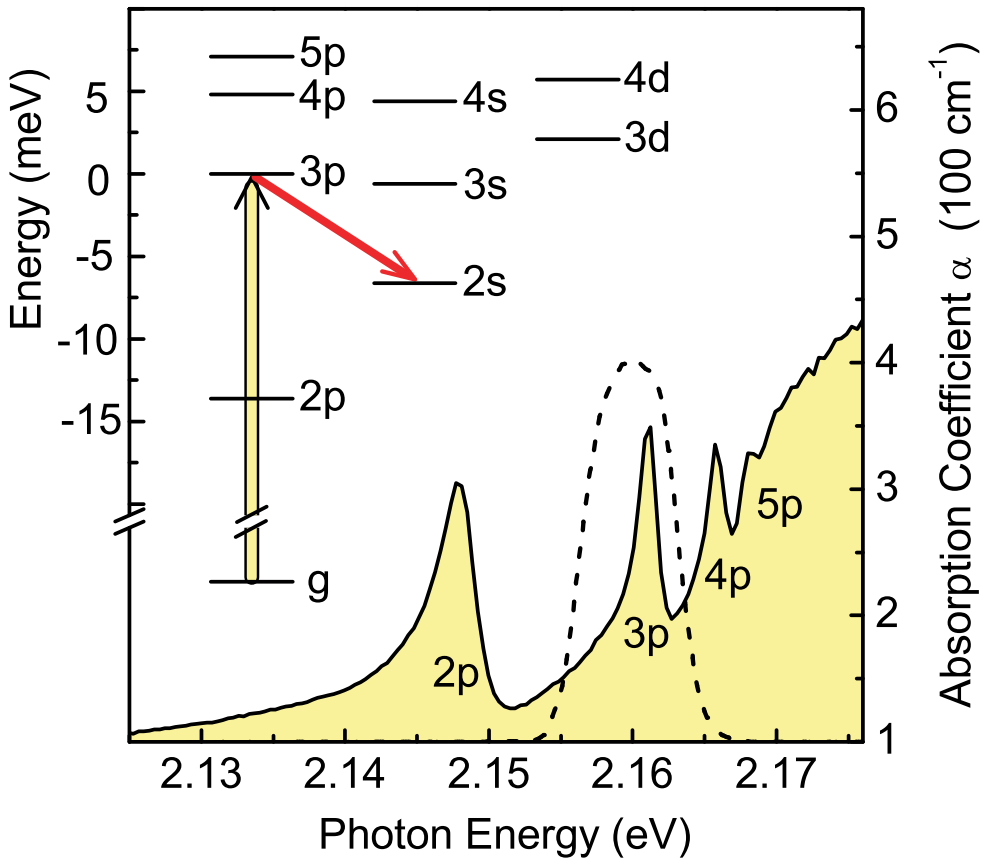

Figure 5.2: Optical absorption spectrum of the Cu_2O crystal studied in this work, at $T = 6$ K. Exciton absorption lines exhibit widths of 3.6 meV ($2p$) and 1.8 meV ($3p$). The term scheme indicates the yellow exciton series, with energy differences given with respect to the $3p$ exciton level.[102] Resonant excitation of $3p$ excitons is indicated by the thick upward arrow (a corresponding typical pump spectrum is shown by the dashed curve). Internal exciton transitions from p- to s- or d-states are dipole allowed (solid arrow).

duction band minima at the Brillouin zone center, even parity s- and d-excitons are dipole forbidden.[102] The asymmetry of the absorption line may be understood as an example of Fano interference, in which a discrete state couples to an energetically degenerate continuum, in this case the phonon bath.[103,104] Figure 5.2 shows a detailed exciton term scheme, with the energy difference to the $3p$ level given on the left.

Far infrared transmission [Figure 5.3] measurements confirm the unexcited sample to be transparent with no absorption features in the window between 1 and 12 meV. This broadband characterization was performed utilizing the GaP emitter-detector pair described in section 2.4. The phonon is clearly resolved at 18 meV and will not impact characterization focused on the $3p$-$2s$ transition studied hereafter.

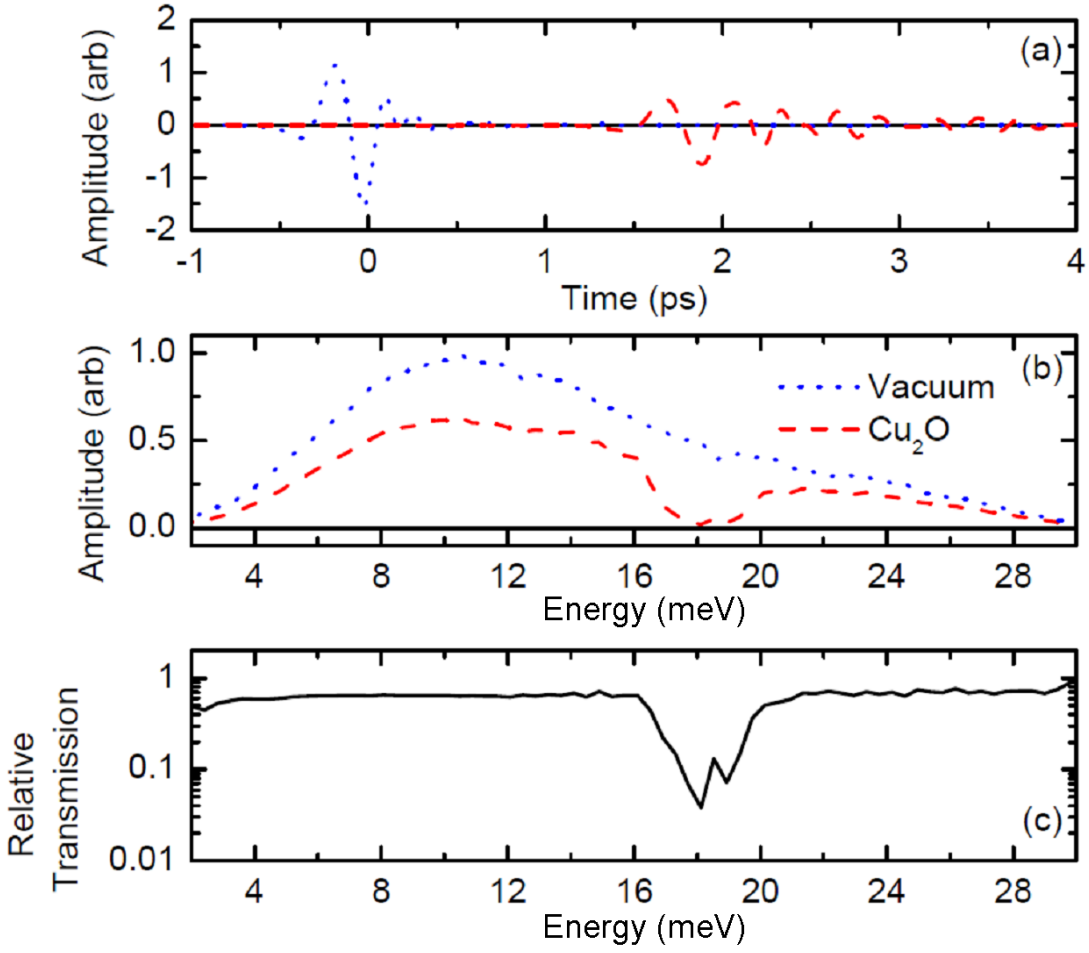

Figure 5.3: Far-infrared transmission of unexcited cuprous oxide: (a) Electric field transients after transmission through vacuum (dotted) and through the sample (dashed). (b) Amplitude spectra. (c) Relative transmission spectrum.

The experimental scheme is based on the previously described ultrafast regenerative $Ti{:}Al_2O_3$ amplifier operating at 250 kHz repetition rate, which delivers 42 fs light pulses at a center wavelength of 800 nm. Near-bandwidth-limited light pulses tunable around 575 nm wavelength are obtained by subsequent optical parametric amplification as described in section 2.3. I use a grating-based pulse shaper to tailor the energy and width of these visible pulses, in order to selectively photoexcite specific bound exciton states or the continuum of unbound electron-hole (e-h) pairs. A resulting typical pump spectrum is indicated by the dashed curve in Figure 5.2. Ultrashort THz probe pulses are obtained by difference frequency mixing within the broad spectrum of a second branch of the near-infrared laser output. This process of optical rectification is achieved in a 500-μm-thick ZnTe crystal

exploiting its large second order nonlinearity $\chi^{(}2)$.[92] The real-time electric field trace $E_{\mathrm{THz}}(t)$ of the transmitted THz pulse is recorded by means of electro-optic sampling with a large signal-to-noise ratio of 10^5. Owing to THz field measurement directly in the time-domain, both real and imaginary parts of the optical response are obtained on equal footing.

In a first set of experiments, I resonantly excite the Cu_2O sample at specific exciton absorption lines and follow the subsequent transient changes in the far-infrared response via a time-delayed THz pulse. Figures 5.4(a)-(c) show the transmitted THz field $E_{\mathrm{THz}}(t)$ without photoexcitation (thin lines, down-scaled by a factor of 500), and its transient change $\Delta E_{\mathrm{THz}}(\Delta t, t)$ (thick lines) induced by photoexcitation at three characteristic wavelengths. The temporal delay between the yellow pump pulse and the electro-optic gating pulse is kept fixed at $\Delta t = 1$ ps. Differential transmission spectra $\Delta T/T$ corresponding to each case are shown in the right panels of Figure 5.4. The response reveals a critical wavelength dependence: excitation in the continuum [Figs. 5.4(a),(d)] or at the $2p$ resonance [Figs. 5.4(c),(f)] induces electric field transients that resemble the reference pulse with a phase offset. A featureless broadband decrease of transmission results. In contrast, resonant excitation of $3p$ excitons shows a very different shape of the induced field and a strongly structured transmission change [Figures 5.4(b),(e)]. In particular, I find a remarkable increased transmission around 6.6 meV photon energy.

5.3.2 Results and observations

One may now use the full knowledge of the THz electric fields in both amplitude and phase to determine directly the change of the complex refractive index $\tilde{n}(\omega) \equiv n(\omega) + i\frac{c}{2\omega}\alpha(\omega)$, where n denotes the real part of the refractive index and α is the absorption coefficient. Since the excitation density decays exponentially along the propagation length z inside the crystal, I express the locally induced change as $\Delta\tilde{n}(z,\omega) = \Delta\tilde{n}(\omega)\ \exp\{-\alpha_{\mathrm{vis}} z\}$. Here, α_{vis} is the absorption coefficient in the visible (Figure 5.2) and $\Delta\tilde{n}(\omega)$ refers to the pump-induced change at the entrance face of the crystal. Based on this information and including the known refractive index of Cu_2O,[105] the complex transfer function of the photo-excited sample may be calculated via the well-established Fresnel matrix formalism. In turn, I directly obtain the induced change of the refractive index and absorption at each frequency by varying $\Delta\tilde{n}(\omega)$ and fitting the resulting response function to the experimental data. Sample Matlab code is included in Appendix B.1 for reference. All relevant results discussed in the following are insensitive to the exact parameters used in the analysis.

Figure 5.5 displays the differential changes Δn and $\Delta\alpha$ obtained from the traces in Figure 5.4. Continuum excitation [topmost curves in Figures 5.5(a-b)] results in a predominantly inductive THz response, well explained by the Drude theory (dashed-dotted lines) of a conducting e-h gas. In contrast, resonant $2p$ excitation induces only small changes in the refractive index (lowest curves in Figure 5.5) as expected for insulating, bound states.

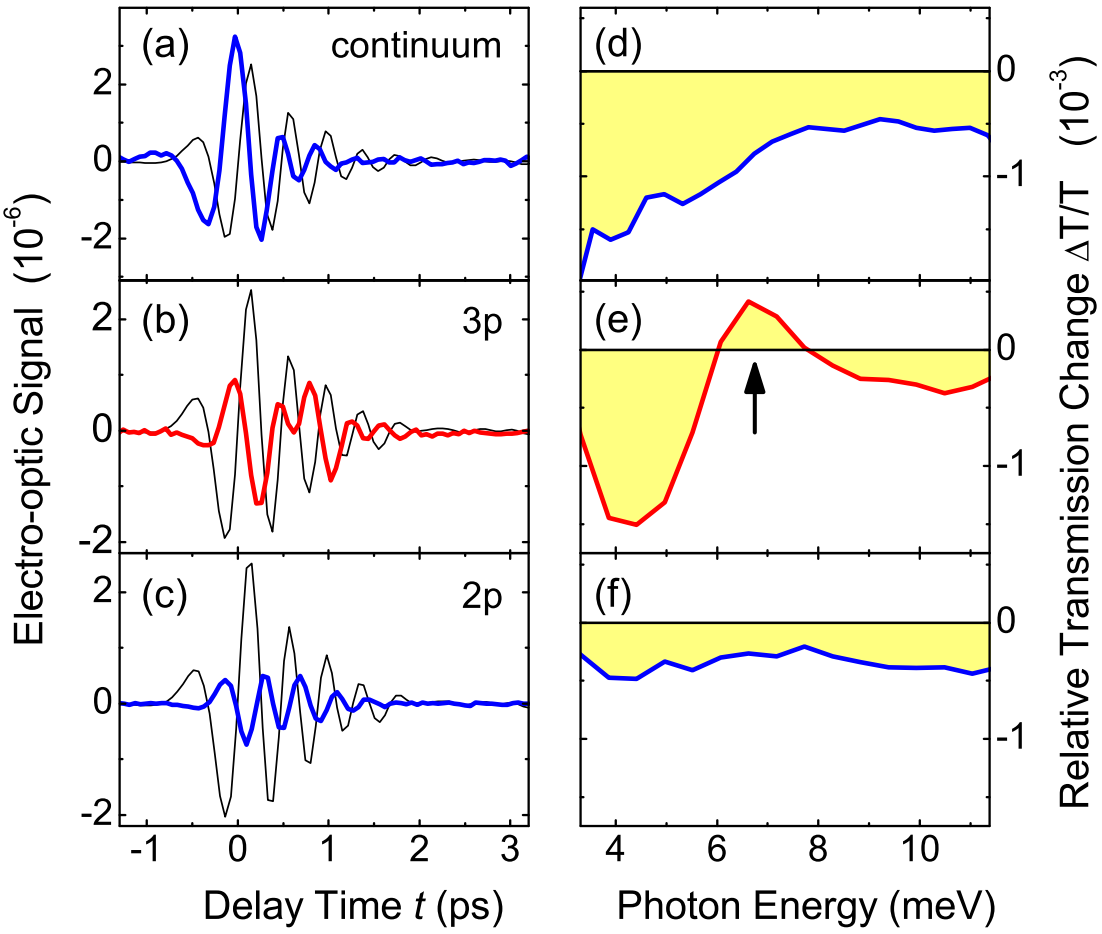

Figure 5.4: (a)-(c) Pump-induced changes ΔE_{THz} (thick lines) at $\Delta t = 1$ ps after excitation, and reference THz fields E_{THz} (thin lines, down-scaled by a factor of 500 for better visibility) without excitation. Pump spectra are centered (a) in the continuum at 2.206 eV, (b) at the yellow $3p$ exciton line, and (c) at the $2p$ exciton line. (d)-(f) Corresponding relative transmission changes $\Delta T/T$. Arrow: enhanced transmission at 6.6 meV.

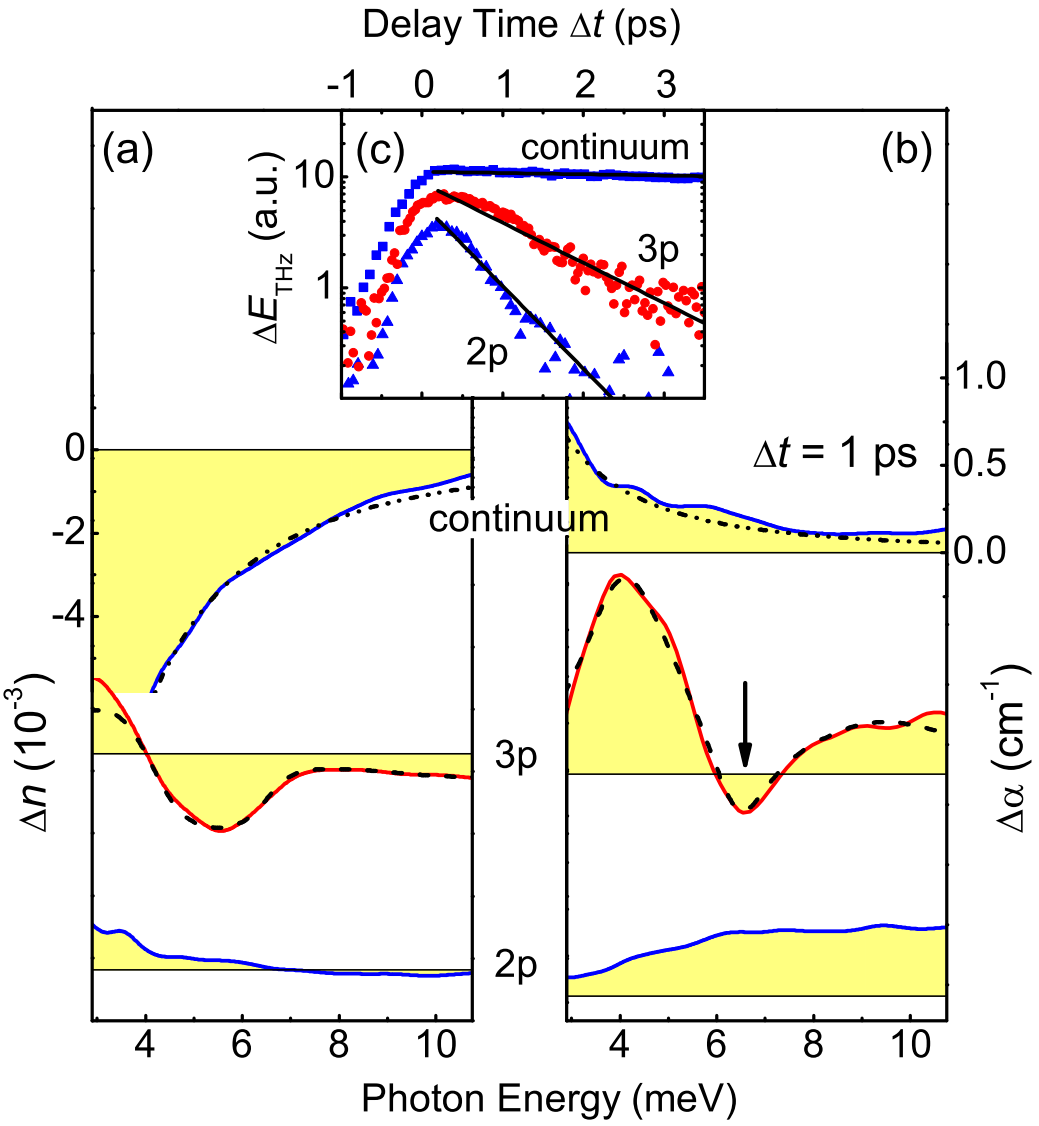

Figure 5.5: THz response at $\Delta t = 1$ ps after excitation of $2p$ or $3p$ excitons, or the continuum. (a),(b) Changes of refractive index Δn and absorption $\Delta\alpha$ (solid lines, offset vertically for clarity). Dash-dotted lines: a Drude response (topmost curves) with screened plasmon energy $\hbar\omega_{\rm pl} = 0.3$ meV and damping $\Gamma/2\pi = 0.4$ meV. Dashed lines: model of three oscillators (lower curves) with energies (and linewidths) $E_1 = 4.5$ meV (2.5 meV), $E_2 = 6.6$ meV (1.6 meV), and $E_3 = 9.5$ meV (4 meV), and relative oscillator strengths as given in the text. The vertical arrow marks the negative absorption change occurring around 6.6 meV. (c) Ultrafast pump-probe dynamics of the induced change of the THz field at corresponding pump energies.

The most striking response is obtained after selective excitation of the $3p$ interband resonance, yielding a pronounced spectral structure in both $\Delta\alpha$ and Δn. With increasing frequency, a peak of enhanced absorption occurs at 4.5 meV, followed by a narrow minimum of $\Delta\alpha$ at 6.6 meV. Indeed, here the induced absorption becomes negative. I emphasize three key aspects of this observation: (*i*) unexcited Cu_2O shows no discernible THz absorption in this frequency range as shown above, (*ii*) the minimum with $\Delta\alpha < 0$ appears exclusively after resonant excitation of $3p$ excitons, and (*iii*) the observed resonance energy of 6.6 meV is precisely identical with the $3p$–$2s$ level spacing (Figure 5.2). Hence, I can identify the negative absorption peak as *stimulated emission* of THz radiation via the $3p \rightarrow 2s$ intra-excitonic transition.

For further analysis, I model the lineshape of the THz response upon $3p$ excitation. A faithful representation of the experiment is achieved with a model of three oscillators (dashed lines, Figure 5.5). By comparison with the term scheme of Figure 5.2, I attribute the lowest-frequency oscillator centered at 4.5 meV to the joint effects of $3p \rightarrow 4s$ and $3p \rightarrow 4d$ transitions. The center oscillator at 6.6 meV exhibits a negative oscillator strength, in accordance with the $3p \rightarrow 2s$ stimulated emission. Finally, a component at 9.5 meV phenomenologically describes all transitions to higher bound states. The relative oscillator strengths f_1:f_2:f_3 = 2.7:(-1):1.1 agree qualitatively with a hydrogen model [4.4:(-1):2], thus supporting this assignment.[106] A more rigorous theory should also take into account the partial *d*-character of the $2s$ exciton in Cu_2O.[102] With an estimated density of $3p$ excitons of 3×10^{13} cm^{-3} I obtain a cross section for the $3p \rightarrow 2s$ transition of $\sigma \approx 10^{-14}$ cm^2. This value compares well with order-of-magnitude estimates based on hydrogenic exciton wavefunctions.[95]

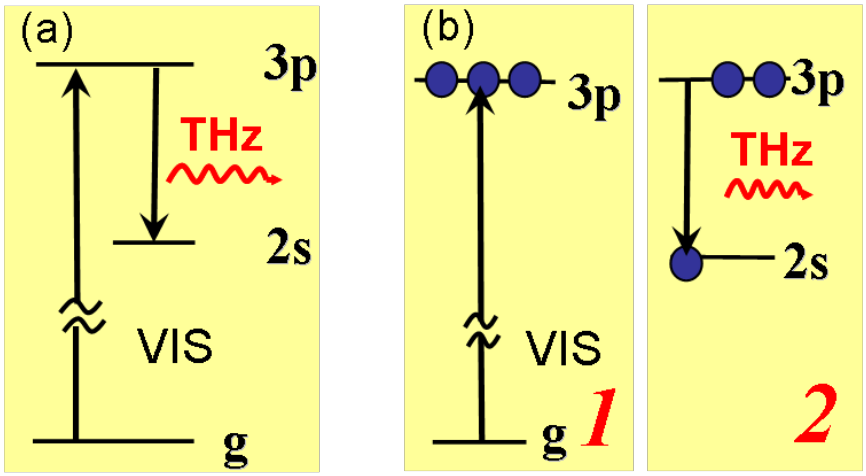

Figure 5.6: Cartoon showing the possible descriptions of stimulated emission in this system. In (a), stimulated Raman scattering occurs when the THz probe pulse couples to the coherent polarization induced by the pump. In (b), stimulated emission occurs through the more familiar population inversion, with the population in this case being incoherent excitons.

Unlike atomic systems, visible photoexcitation of excitons initially induces coherent polarization waves, which only later convert into populations via scattering processes. Thus, stimulated THz emission from excitons may originate from two different types of processes:[96,107] (*a*) *coherent excitonic polarizations,* where THz emission results from stimulated Raman scattering as a single-step nonlinear optical process–the THz field coherently couples polarizations from the $3p$ to the $2s$ state, from which in turn visible pump photons are scattered into the THz field, (*b*) *incoherent exciton populations,* where stimulated emission is driven purely by population inversion and subsequent hot luminescence, analogous to atomic lasers. These two processes are illustrated in Figure 5.6. The relative importance of these processes depends on the polarization and population decay times. A dephasing time for the $3p$ level can be estimated from the visible linewidth, which yields $T_2 \approx 0.7$ ps assuming predominantly homogeneous broadening for the high-quality Cu_2O crystal. Population relaxation can be deduced from the dynamics of the induced THz response. Figure 5.5(c) depicts an increasingly faster exponential decay as I tune from continuum states ($\tau = 36$ ps), via the $3p$ ($\tau = 1.3$ ps) to the $2p$ exciton ($\tau = 0.8$ ps). The relative spectral shape does not vary strongly in time (not shown). The relaxation is explained by recombination and scattering into $1s$ excitons mediated by optical phonon interactions.[108] On this basis, stimulated THz emission after $3p$ excitation occurs both during an initial regime of coherent excitonic polarizations and from the subsequent incoherent inverted population of excitons.

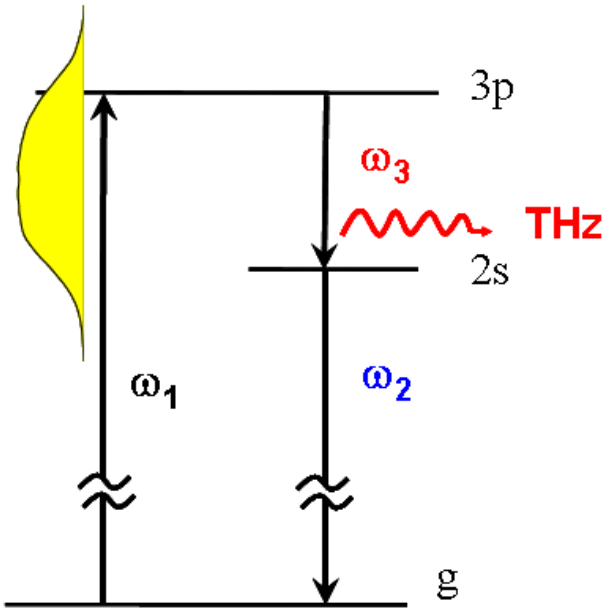

Figure 5.7: Scheme for quantum beats of intra-excitonic levels. The spectrum of the pump pulse overlaps both the $3p$ and $2s$ states. Unlike for stimulated emission, there is no external THz pulse incident on the sample.

5.4 Terahertz generation via quantum beats

In the following, I show that coherent manipulation of the $3p \rightarrow 2s$ transition may be exploited to emit THz radiation even without stimulation by external THz fields. For this second set of experiments on Cu_2O, the pump spectrum is tuned to simultaneously overlap both the $3p$ and the dipole-forbidden $2s$ resonances, as illustrated in Figure 5.7.

No THz probe light was incident on the sample. I observe emission of a coherent THz field. The transient [Figure 5.8(a)] is detected electro-optically by scanning the delay Δt between the visible pump and the near-infrared gating pulse. The corresponding power spectrum in Figure 5.8(b) peaks at 6.6 meV and exhibits a width of 1.7 meV (FWHM). This lineshape coincides with the values deduced from the $3p \rightarrow 2s$ transition in Figure 5.5, corroborating that the THz transient originates from the same internal exciton transition. The absolute size of these emitted fields is comparable to the transients ΔE_{THz} in Figure 5.4 stimulated by a far-infrared seed pulse. This fact implies that the generation mechanism cannot be explained by a spontaneous version of the emission process discussed above.

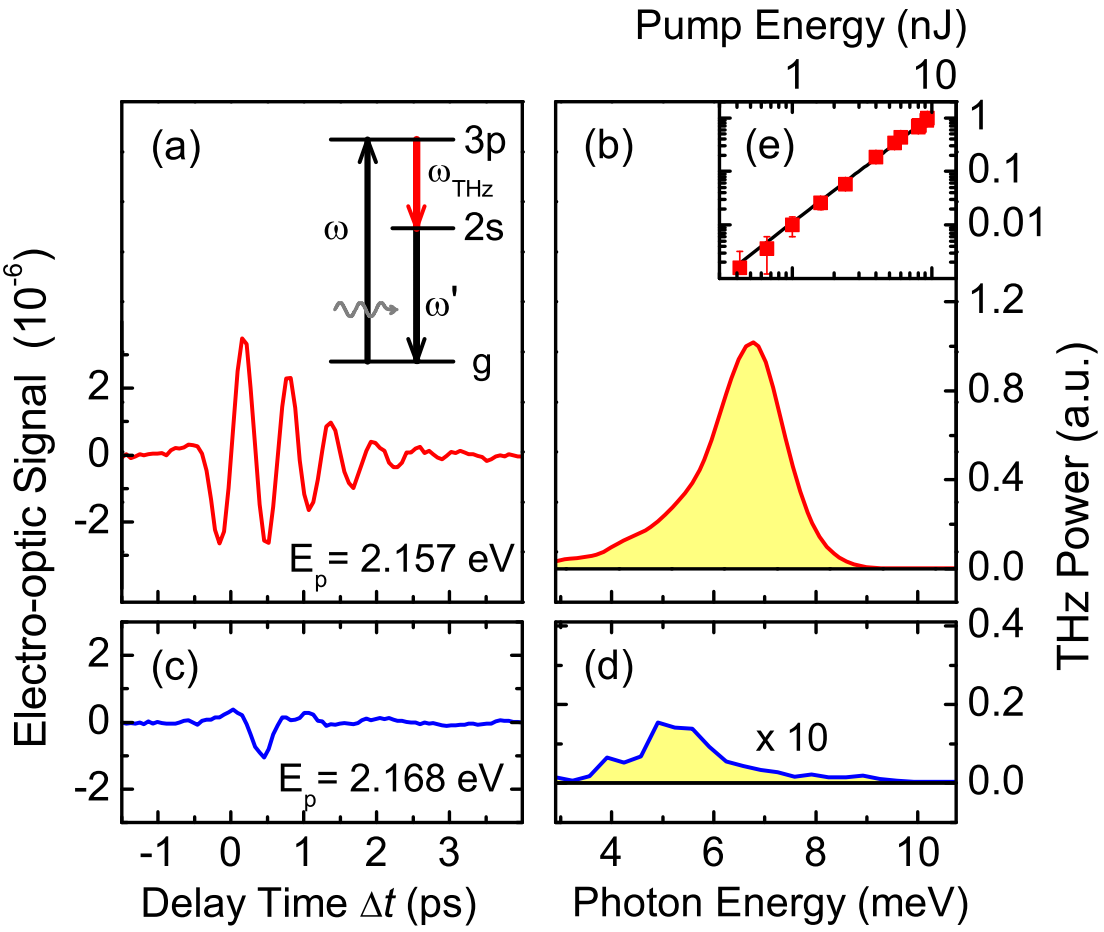

Figure 5.8: THz generation in Cu_2O: (a) Real time trace and (b) normalized power spectrum of THz pulses (FWHM: 1.7 meV) obtained with the pump centered at 2.157 eV (close to the $3p$ resonance). The spectral width of the pump pulse is 12 meV (FWHM). Inset: term scheme of the underlying quantum process. (c),(d) THz emission for pump centered at 2.168 eV. (e) The emitted THz power for excitation at 2.157 eV scales quadratically as a function of the pump pulse energy.

Moreover, I find that the THz polarization is parallel to the linear polarization of the pump light, as shown in Figure 5.9. In the figure, the amplitude of the emitted THz radiation parallel to the usual THz probe polarization is monitored while the polarization of the probe pulse is rotated. The emitted THz radiation clearly follows precisely the pump polarization. In contrast, the polarization of the stimulated change ΔE_{THz}, described previously, is determined by the *probe* polarization, not the pump.

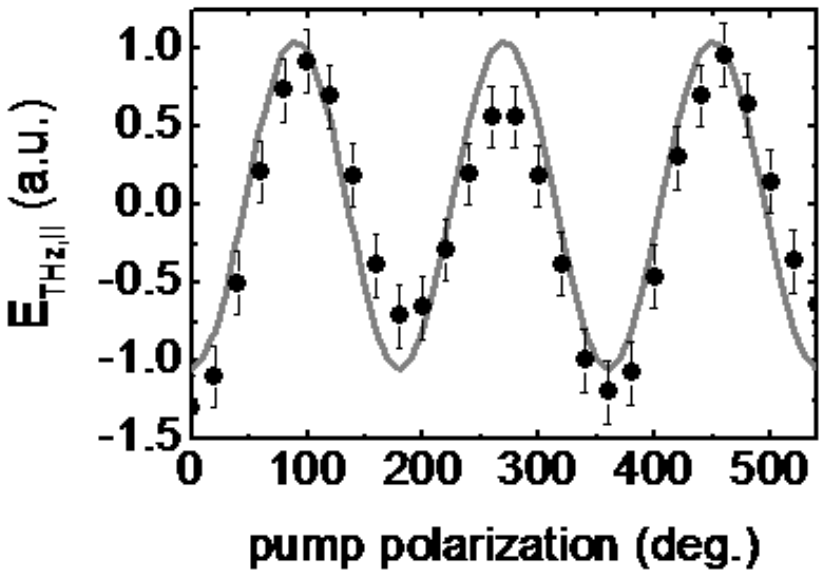

Figure 5.9: Polarization dependence of the emitted terahertz radiation versus the polarization of the incident pump pulses.

I interpret this THz emission as resulting from quantum beats between coherent exciton polarizations. Visible light induces $3p$ exciton polarizations, while the low-energy wing of the pump spectrum couples the $2s$ level to the ground state, e.g. via a weak quadrupole or surface field assisted dipole transition.[95,109] As $3p$ and $2s$ states feature opposite parity, quantum beats between them act as a radiating dipole. The THz generation may be expressed as an effective difference frequency process, described by the nonlinear susceptibility:[110]

$$\chi^{(2)}_{\text{eff}} \propto \frac{\mathrm{M}_{3p}\mathrm{M}_{2s}\mathrm{M}_{3p-2s}}{(\omega - \omega_{3p} + i\Gamma_{3p})(\omega_{\text{THz}} - \omega_{3p-2s} + i\Gamma_{3p-2s})} \tag{5.1}$$

where M_{3p} and M_{2s} are the visible interband matrix elements and M_{3p-2s} is the THz dipole matrix element. Furthermore, ω and ω_{THz} are the frequencies of visible pump and emitted THz fields, and ω_{3p} and ω_{3p-2s} are visible $3p$ and THz $3p \rightarrow 2s$ resonance energies with corresponding dephasing constants Γ_i. The three-wave interaction is schematically indicated in Figure 5.7. In this experiment both terms in the denominator become resonant, which leads to a high nonlinearity despite the relative weakness of the coupling between 2s excitons and the ground state. Off-resonant pumping reduces the conversion efficiency dramatically [Figs. 5.8(c),(d)].

As shown in Figure 5.8(e), the emitted THz intensity scales quadratically with the pump power which further supports this $\chi^{(2)}$ picture. From the pulse intensities and effective

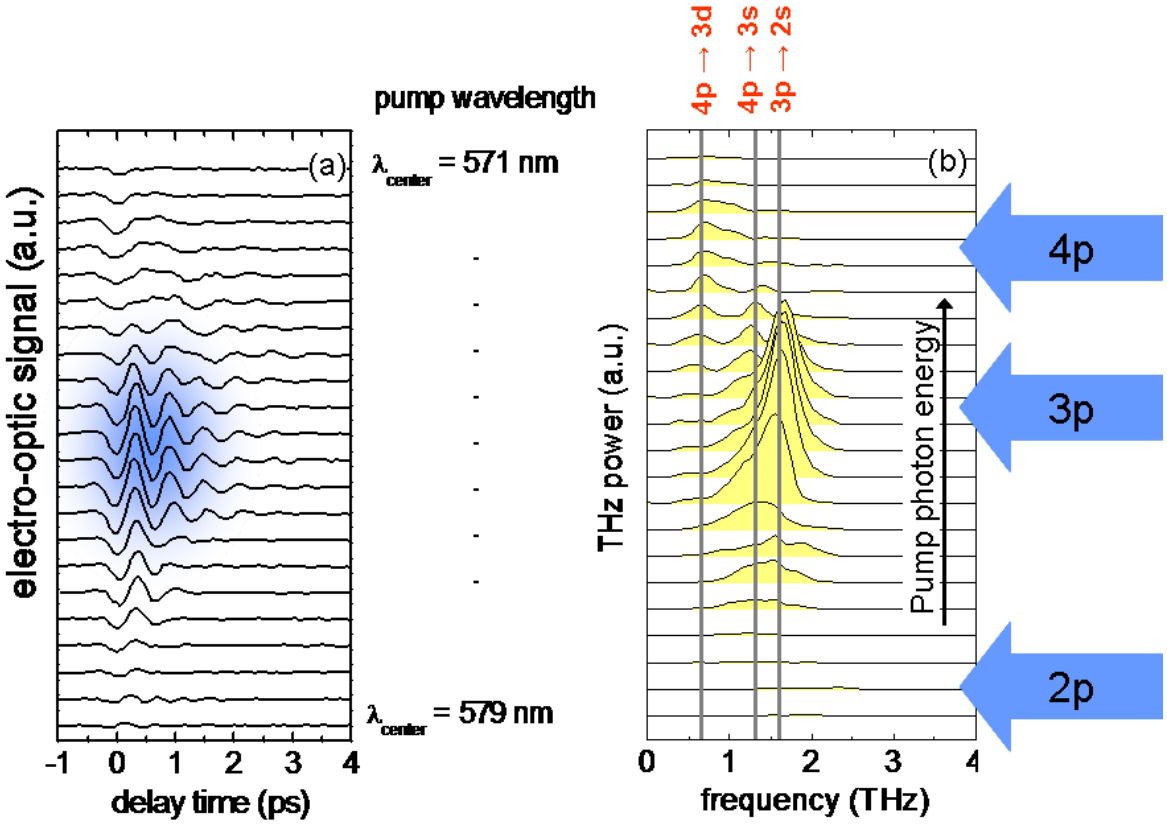

Figure 5.10: (a) Terahertz pulses generated via quantum beating of intra-excitonic levels. (b) Power spectra obtained by Fourier transform of the time-domain emitted THz fields from (a). Several dipole allowed transitions within the spectral bandwidth of the pump pulses are visible.

interaction length I estimate a nonlinearity of $\chi^{(2)}_{\text{eff}} \gtrsim 10\ pm/V$. This value exceeds the high background nonlinearity of non-centrosymmetric materials such as ZnTe, which is widely used for THz generation.[111]

By sweeping the center wavelength of the pump spectrum, it becomes possible, in fact, to map out the dipole-allowed excitonic transitions within the spectral bandwidth of the pulse. Figure 5.10 shows the THz fields emitted for different pump center wavelengths, and the resulting power spectra obtained from the time domain emitted fields via Fourier transform. In addition to the $3p$-$2s$ transition already discussed, these spectra show that beating between $4p$-$3s$ and $4p$-$3d$ levels is also possible by tuning the pump spectra to overlap those levels.

To summarize, I have observed for the first time stimulated emission of far-infrared radiation from internal transitions in excitons. Broadband THz spectroscopy was employed

to directly map out the ultrafast dynamics, spectral positions, and line broadenings of intra-excitonic transitions in Cu_2O. Stimulated emission occurs at 6.6 meV. The detailed picture is further corroborated by the independent observation of strong THz emission at the same energy due to $2s$-$3p$ quantum beats. These results provide a new, fundamental test of excitonic quantum physics, and illuminate analogies and differences to atomic systems.

By demonstrating intra-excitonic stimulated emission via population inversion of the internal energy structure of excitonic system, stimulated emission, this work has opened up new possibilities for the quantum manipulation of excitons. This demonstration of yet greater analogy between excitons and atoms suggest many new research directions, especially given the utility of optical methods common for the manipulation of cold atomic gases and the search for BEC of excitons. It has recently been demonstrated that intense terahertz pulses can coherently drive a cold $1s$ para-exciton gas in Cu_2O into the $2p$ state, through up to two Rabi cycles.[112,113] This gives great promise towards increasing nonlinear control over excitonic systems, and a new direction for the preparation of cold, dense excitonic gases by the coherent quantum-optical manipulation of their internal structure.

Chapter 6

Conclusion

In chapter 3, I have presented experimental observations of hole density in the hole-mediated ferromagnetic semiconductor gallium manganese phosphide, created with high manganese incorporation through ion implantation and pulsed-laser melting. It is observed that free-hole concentrations in this material below the Curie temperature are relatively small, confirming the observation that in contrast to gallium manganese arsenide, where ferromagnetic order is mediated by delocalized carriers, the holes in the phosphide system are highly localized.

In chapter 4, I have presented broadband terahertz studies of a high-density exciton gas in GaAs/AlGaAs multiple quantum wells. I was able to directly gauge the bound and unbound pair densities and observe the excitonic fine structure as it evolves under high-density conditions. With increasing excitation density, the far-infrared complex conductivity of this many-body system reveals a distinct red-shift of the intra-excitonic $1s$-$2p$ transition and a strong broadening of the $2p$ bound state, finally leading to the disappearance of the resonance. This technique may prove valuable in future studies of cold dense spatially-indirect excitons, or in understanding the interactions of strongly confined carriers in semiconductor quantum dots.

In chapter 5, I have presented first time observations of stimulated emission of terahertz radiation from internal exciton transitions. By directly generating excitons in a excited P state in the semiconductor cuprous oxide, it is possible to stimulate the downward dipole transition to the S state with an ultrafast terahertz pulse. This study demonstrates the potential for the direct, coherent manipulation of excitons by far-infrared light. I also discussed the observation of the generation of terahertz radiation by quantum beating of internal exciton levels. This again allows one to further expand the atomic analogy to excitons.

6.1 Reflections and future directions

This body of work points forward to a wide range of potential fields of study. In the study of the gallium manganese phosphide system, contact-free characterization of the free carrier density in these important model systems may contribute to a better quantitative understanding of carrier mediated ferromagnetism and further improvements in the materials science of magnetic semiconductors. The integration of magnetic and electronic systems opens up incredible possibilities for both scientists and engineers. These studies of excitons at high densities in gallium arsenide quantum wells help to continue to expand and test the limits of the hydrogenic picture of excitons. The first observation of stimulated emission from internal exciton transitions has opened up entire new realms of possibility for the coherent manipulation of excitons. Again, by testing the boundaries of the atomic picture of excitons, new questions naturally arise. If stimulated emission is possible, what about lasing? Cuprous oxide has long been studied as a candidate for Bose-Einstein condensation of excitons; can excitonic populations be cooled by a parallel process to the laser cooling used in atomic gases? The many new realms of physics opened up by the convergence of ultrafast measurement techniques and nanoscale manipulation of materials portends exciting times in condensed matter physics for decades to come.

Appendix A

List of Symbols

ϵ	dielectric constant
ϵ_1	real part of dielectric constant
ϵ_2	imaginary part of dielectric constant
σ	conductivity
σ_1	real part of conductivity
σ_2	imaginary part of conductivity
n	index of refraction
α	absorption coefficient
c	speed of light
$\hbar$	Planck's constant
k	wavenumber
λ	wavelength
ν	frequency
E	energy
Γ	broadening
γ	decay time

Appendix B

Matlab code samples

This Appendix includes Matlab code samples utilized for data analysis.

B.1 Analysis of terahertz transmission for "thick" samples

B.1.1 Data evaluation

```
% script for numerical evaluation of pump-probe data
clear all
c=299792458;                    %vacuum speed of light

% import raw data:
ref = load('ref.dat');
pp = load('pp.dat');
T_ref_raw = ref(:,1);
E_ref_raw = ref(:,3);
T_pp_raw = pp(:,1);
E_pp_raw = pp(:,3);
Δ_T = (max(T_ref_raw)-min(T_ref_raw))./(length(T_ref_raw)-1);
T = [min(T_ref_raw):Δ_T:max(T_ref_raw)];
E_ref = interp1(T_ref_raw,E_ref_raw,T);
E_pp = interp1(T_pp_raw,E_pp_raw,T);

% calculate complex-valued transmission function of pumped sample:
f_max = 1./Δ_T;
Δ_f = 1./(max(T)-min(T));
ratio = ifft(E_ref+E_pp)./ifft(E_ref);
L=330e-6; %sample thickness
absorption=350*100; %absorption coefficient
number_of_steps=; %number of steps to simulate absoprtion profile

```

```
for k = 1:length(T)
   f(k) = (k-1).*Δ_f.*(10^15);
   t(k) = ratio(k).*transferfunction(L,absorption,f(k),...
    n_Cu2O(0,f(k)),0,number_of_steps);
   [n_r(k),n_i(k),control(k)] = Newton(f(k),t(k),L,absorption,...
    number_of_steps);
   difference(k) = t(k)-control(k);
   Δ_n_r(k) = n_r(k)-real(n_Cu2O(0,f(k)));
   Δ_n_i(k) = n_i(k)-imag(n_Cu2O(0,f(k)));
   epsilon(k) = (n_r(k)+i.*n_i(k)).^2;
   epsilon_unexc(k) = (real(n_Cu2O(0,f(k)))+i.*imag(n_Cu2O(0,f(k)))).^2;
   Δ_sigma_1(k) = (f(k).*imag(epsilon(k))./2-f(k)...
    .*imag(epsilon_unexc(k))./2).*(1.1*10^(-12));
   Δ_epsilon_1(k) = real(epsilon(k)-epsilon_unexc(k));
   alpha(k) = 4*pi*n_i(k)*(1/c).*f(k);
   Δ_alpha(k) = 4*pi*Δ_n_i(k)*(1/c).*f(k);
end

% save calculated data:
f = f';
Δ_n_r = Δ_n_r';
Δ_n_i = Δ_n_i';
Δ_alpha = Δ_alpha';
Δ_sigma_1 = Δ_sigma_1';
Δ_epsilon_1 = Δ_epsilon_1';
Imaginary_epsilon = imag(epsilon)';
Real_epsilon = real(epsilon)';
D(:,1) = (10^(-12)).*f(:,1);
D(:,2) = Δ_n_r(:,1);
D(:,3) = Δ_n_i(:,1);
D(:,4) = Δ_alpha(:,1);
D(:,5) = Δ_sigma_1(:,1);
D(:,6) = Δ_epsilon_1(:,1);
D(:,7) = Imaginary_epsilon(:,1);
D(:,8) = Real_epsilon(:,1);

save 000.dat D -ascii;

figure(1), subplot(2,2,1), plot(f./(10^12), Δ_n_r,'k+-');
axis([0 3 -1 3]);xlabel('frequency (THz)'), ylabel('{\Delta}n_r');
figure(1), subplot(2,2,2), plot(f./(10^12), Δ_n_i, 'k+-');
axis([0 3 -1 3]);xlabel('frequency (THz)'), ylabel('{\Delta}n_i');
% figure(1), subplot(2,2,3), plot(f./(10^12), abs(imag(1./(epsil))),...
%   'k+-', f, -imag(1./((epsilon(n_anreg,f)).^2)),'b-');
% axis([0 40 -0.1 1]);xlabel('frequency (THz)'), ylabel('-im(1/epsilon)');
figure(1), subplot(2,2,4), plot(f./(10^12), Δ_alpha./100, 'k+-');
axis([0 3 -1 2000]);xlabel('frequency (THz)'),
ylabel('{\Delta}{\alpha} (cm^{-1})');
```

B.1.2 Newton algorithm

```
% script of a Newton-Raphson algorithm
% to retrieve the refractive index from the
% complex transmission measured in THz-TDS

function [n_r,n_i,control]=Newton(frequency,measured_transmission,p1,p2,p3)

f = frequency;
t_m = measured_transmission;
L = p1;  % total thickness of sample in meter
alpha = p2; % absorption coefficient = inverse skin depth in inverse meter
number_of_steps = p3; % number of points to sample refractive index



%initializing the loop:
n_background = abs(n_equil(eps,f));
%define a start value for the refractive index
n_k = n_background;
t_k = transferfunction(L, alpha, n_background, n_k-n_background, f,...
    number_of_steps); % start with transfer function of unexcited sample

while abs(t_k-t_m) > 1000000*eps,
    dt_dn = (transferfunction(L, alpha, n_background, n_k-n_background,...
    f, number_of_steps)-transferfunction(L, alpha, n_background,...
    n_k-0.000001-n_background, f, number_of_steps))./(0.000001);
    dn_dt = 1./((dt_dn+eps));
    dn = (t_m-t_k).*dn_dt;
    n_k = n_k+dn;
    t_k = transferfunction(L, alpha, n_background, n_k-n_background, f,...
    number_of_steps);
end
control = t_k;
n_r = real(n_k);
n_i = imag(n_k);
alpha = 4.*pi.*n_i.*f./299792458;
```

B.1.3 FIR Transmission including pump absorption profile

```
%%%%%%%%%%%%%%%%%%%%%%%%%%%%%%%%%%%%%%%%%%%%%%%%%%%%%
% Function to calculate complex transfer function   %
% t of CdSe NC solution with the following input    %
% parameters:                                       %
% p1: sample thickness L                            %
% p2: absorption coefficient alpha in inverse meters%
% p3: background refractive index                   %
```

```
% p4: pump-induced change of refr. index            %
% p5: frequency f                                   %
% p6: number of steps to sample refractive index    %
%%%%%%%%%%%%%%%%%%%%%%%%%%%%%%%%%%%%%%%%%%%%%%%%%%%%%%%%

function t = transferfunction(p1,p2,p3,p4,p5,p6)

L = p1;  % total thickness of medium in meters
alpha = p2; % absorption coefficient = inverse skin depth in inverse meters
n_background = p3; % background refractive index
Δ_n_0 = p4;  % largest deviation of refractive index from background
                % occuring at the entrance face of the medium
f = p5; % frequency in Hertz
number_of_steps = p6;
% n_background = real(n_background)-i.*imag(n_background);
% Δ_n_0 = real(Δ_n_0)-i.*imag(Δ_n_0);


% Definition of important constants:
c = 299792458 ; % vacuum speed of light
epsilon_0 = 8.85419*10^(-12) ; % vacuum dielectric function
mue_0 = 4*pi*10^(-7); % vacuum permeability

% Calculation of complex transfer function from matrix elements:
Y_0 = sqrt(epsilon_0/mue_0).*1;
Y_s = sqrt(epsilon_0/mue_0).*n_background;
M = exptransfer(L, alpha, n_background, Δ_n_0, f, number_of_steps);
t = 2.*Y_0./(Y_0.*M(1,1)+Y_0.*Y_s.*M(1,2)+M(2,1)+Y_s.*M(2,2));
%r = (Y_0.*M(1,1)+Y_0.*Y_s.*M(1,2)-M(2,1)-Y_s.*M(2,2))...
%   ./(Y_0.*M(1,1)+Y_0.*Y_s.*M(1,2)+M(2,1)+Y_s.*M(2,2));



%%%%%%%%%%%%%%%%%%%%%%%%%%%%%%%%%%%%%%%%%%%%%%%%%%%%%%%%
%   function to calculate the transfer matrix       %
%   of a medium characterized by an exponentially   %
%   decaying complex refractive index n (input)     %
%%%%%%%%%%%%%%%%%%%%%%%%%%%%%%%%%%%%%%%%%%%%%%%%%%%%%%%%

function M = exptransfer(p1,p2,p3,p4,p5,p6)

L = p1;  % total thickness of medium in meters
alpha = p2; % absorption coefficient = inverse skin depth in inverse meters
n_background = p3; % background refractive index
Δ_n_0 = p4;  % largest deviation of refractive index from background
                % occuring at the entrance face of the medium
f = p5; % frequency in Hertz
number_of_steps = p6;

% Define a length scale:
Δ_x = L./number_of_steps;
```

```
x = [0:Δ_x:(number_of_steps-1).*Δ_x];
n = n_background + Δ_n_0.*exp(-x.*alpha);
m = diag([1,1]); % initialize transfer matrix

for t = 1:length(x)
    m_current = transfermatrix(Δ_x,n(t),f);
    m = m*m_current;
end

M = m;
```

```
%%%%%%%%%%%%%%%%%%%%%%%%%%%%%%%%%%%%%%%%%%%%%%%%%%%%%%%%%%%%
% Function to calculate the transfer matrix of a     %
% dielectric slab of thickness d and complex         %
% refractive index n to be given as input para-      %
% meters                                             %
%%%%%%%%%%%%%%%%%%%%%%%%%%%%%%%%%%%%%%%%%%%%%%%%%%%%%%%%%%%%

function M = transfermatrix(p1,p2,p3)
d = p1;  % slab thickness in meters
n = p2;  % complex valued refractive index
f = p3;  % frequency in Hertz
% n=real(n)-i*imag(n);

% Definition of important constants:
c = 299792458 ; % vacuum speed of light
epsilon_0 = 8.85419*10^(-12) ; % vacuum dielectric function
mue_0 = 4*pi*10^(-7); % vacuum permeability

% Definition of derived parameters
lambda = c./(f+eps); % wavelength in meters
k_0 = 2*pi./lambda; % wavevector in inverse meters
phi = n.*k_0.*d; % phase shift experienced in single pass through slab
Y = sqrt(epsilon_0/mue_0).*n; % auxiliary parameter

% Calculation of transfer matrix
% according to E. Hecht, Optik, Addison-Wesley
% M = ones(2,2);
M(1,1) = cos(phi);
M(1,2) = i*sin(phi)./(Y+eps);
M(2,1) = i*sin(phi).*Y;
M(2,2) = cos(phi);
```

B.1.4 Equilibrium index of refraction

```
% function to calculate the complex-valued refractive index of
% bulk Cu2O, taking into account both lattice and plasmonic contributions
```

```
3  % in terms of a dielectric oscillator and a Drude model, respectively
4
5
6  function b=n_Cu2O(x,y)
7  n=x;                              %carrier density in cm^(-3)
8  f=y./(10^12);                             %frequency (y in Hz)
9
10 %important constants
11 c=299792458;             %vacuum speed of light
12 e=1.602*10^(-19);        %elementary charge
13 epsilon_0=8.854*10^(-12);    %vacuum dielectric constant
14 m_e=9.109*10^(-31);      %electron mass
15
16 %material parameters of GaAs
17 epsilon_inf=6.46;        %high-frequency limit of the dielectric function
18 m_eff=0.98*m_e;          %effective mass of electrons in Cu2O
19 mue=40000;%2200;             %electron mobility in cm^2/Vs
20 f_TO=146.3;          %TO-frequency in cm^-1
21 f_LO=149.3;          %LO-frequency in cm^-1
22 gamma=0;             %phonon damping in cm^-1 -- unable to find
23
24 %plasma frequency in THz:
25 f_plasma=(e/(2*pi))*sqrt((n*10^6)/(epsilon_0*epsilon_inf*m_eff))*10^(-12);
26
27 %wave vector scattering time:
28 tau=((mue*m_eff)/e)*10^11;
29
30 %dielectric function taking into account both lattice and plasmonic
31 % contributions
32 % (frequency in THz):
33 ep=epsilon_inf.*(1+((f_LO^2-f_TO^2)./((f_TO^2-(f.*(1/c)*10^10).^2)-i...
34    *gamma.*f.*(1/c)*10^10))-(f_plasma^2./(f.^2+i.*f./(2*pi*tau*10^(-3)))));
35
36 %calculation of the refractive index:
37 b=sqrt(ep);
38 %Reflectivity:
39 %b=abs(((sqrt(epsilon)-1).^2)./((sqrt(epsilon)+1).^2));
40
41 %Absorption:
42 %alpha=4*pi*imag(sqrt(epsilon))*(1/c)*(10^10).*f;
```

Bibliography

[1] T. Maiman. "*Stimulated optical radiation in ruby.*" *Nature* **187**(4736), 493–4 (1960).

[2] C. G. R. Geddes, T. C., J. van Tilborg, E. Esarey, C. Schroeder, D. Bruhwiler, C. Nieter, J. Cary & W. P. Leemans. "*High-quality electron beams from a laser wakefield accelerator using plasma-channel guiding.*" *Nature* **431**, 538–541 (2004).

[3] P. A. Franken, A. E. Hill, C. W. Peters & G. Weinreich. "*Generation of optical harmonics.*" *Phys Rev Lett* **7**(4), 118–119 (1961).

[4] R. W. Boyd. *Nonlinear Optics* (Academic Press, Inc., San Diego, 1992).

[5] M. K. Reed, M. K. Steiner-Shepard & D. K. Negus. "*Widely tunable femtosecond optical parametric amplifier at 250 kHz with a Ti:sapphire regenerative amplifier.*" *Opt Lett* **19**(22), 1855–1857 (1994).

[6] G. Cerullo, M. Nisoli & S. D. Silvestri. "*Generation of 11fs pulses tunable across the visible by optical parametric amplification.*" *Applied Physics Letters* **71**(25), 3616–3618 (1997).

[7] R. A. Baumgartner & R. L. Byer. "*Optical parametric amplification.*" *IEEE J of Quant Elec* **QE-15**(6), 432–444 (1979).

[8] P. Moulton. "*Spectroscopic and laser characteristics of $Ti{:}Al_2O_3$.*" *J Opt Soc Am B* **3**(1), 125 (1986).

[9] K. Wall & A. Sanchez. "*Titanium sapphire lasers.*" *The Lincoln Laboratory Journal* **3**(3), 447 (1990).

[10] R. Aggarwal, A. Sanchez, M. Stuppi, R. Fahey, A. Strauss, W. Rapoport & C.P.Khattak. "*Residual infrared absorption in as-grown and annealed crystals of $Ti{:}Al_2O_3$.*" *IEEE J Quantum Electron* **QE-24**, 1003 (1988).

[11] P. Lacovara, L. Esterowitz & M. Kokta. "*Growth, spectroscopy and lasing of titanium-doped sapphire.*" *IEEE J Quantum Electron* **QE-21**, 1614 (1985).

[12] E. Garmire & A. Yariv. "*Laser mode-locking with saturable absorbers.*" *Quantum Electronics, IEEE Journal of* **3**(6), 222–226 (1967).

[13] D. Spence, P. Kean & W. Sibbett. "*60-fsec pulse generation from a self-mode-locked Ti:sapphire laser.*" *Opt Lett* **16**(1), 42–44 (1991).

[14] F. Salin, J. Squier & M. Piche. "*Mode locking of Ti:Al2O3 lasers and self-focusing: a Gaussian approximation.*" *Opt Lett* **16**(21), 1674–1676 (1991).

[15] J. P. Likforman, G. Grillon, M. Joffre, C. L. Blanc, A. Migus & A. Antonetti. "*Generation of 27 fs pulses of 70kW peak power at 80MHz repetition rate using a cw self-pulsing Ti:sapphire laser.*" *Appl Phys Lett* **58**(19), 2061–2063 (1991).

[16] W. P. de Boeij. *Ultrafast solvation dynamics explored by nonlinear optical spectroscopy.* Diss., University of Groningen (1997).

[17] T. Norris. "*Femtosecond pulse amplification at 250kHz with a Ti:Sapphire regenerative amplifier and application to continuum generation.*" *Opt Lett* **17**(14), 1009–1011 (1992).

[18] Z. Jiang & X. C. Zhang. *Free-space Electro-optic Techniques.* Sensing With Terahertz Radiation (Springer, Berlin; New York, 2003).

[19] P. R. Smith, D. H. Auston & M. C. Nuss. "*Subpicosecond photoconducting dipole antennas.*" *IEEE J Quantum Elect* **24**, 255 (1988).

[20] Y. Cai, I. Brener, J. Lopata, J. Wynn, L. Pfeiffer, J. B. Stark, Q. Wu, X. C. Zhang & J. F. Federici. "*Coherent terahertz radiation detection: Direct comparison between free-space electro-optic sampling and antenna detection.*" *Applied Physics Letters* **73**, 444 (1998).

[21] S. Park, M. R. Melloch & A. M. Weiner. "*Comparison of terahertz waveforms measured by electro-optic and photoconductive sampling.*" *Applied Physics Letters* **73**, 3184 (1998).

[22] D. H. Auston & M. C. Nuss. "*Electrooptic generation and detection of femtosecond electrical transients.*" *IEEE Journal of Quantum Electronics* **24**, 184–197 (1988).

[23] B. B. Hu, X. Zhang, D. H. Auston & P. R. Smith. "*Free-space radiation from electro-optic crystals.*" *Applied Physics Letters* **56**, 506–508 (1990).

[24] A. Nahata, A. S. Weling & T. F. Heinz. "*A wideband coherent terahertz spectroscopy system using optical rectification and electro-optic sampling.*" *Applied Physics Letters* **69**, 2321–2323 (1996).

[25] P. Y. Han & X. Zhang. "*Coherent, broadband midinfrared terahertz beam sensors.*" *Applied Physics Letters* **73**, 3049 (1998).

[26] S. Ehret & H. Schneider. "*Generation of subpicosecond infrared pulses tunable between 5.2 μm and 18 μm at a repetition rate of 76 MHz.*" *Applied Physics B: Lasers and Optics* **66**, 27–30 (1998).

[27] R. A. Kaindl, D. C. Smith, M. Joschko, M. P. Hasselbeck, M. Woerner & T. Elsaesser. "*Femtosecond infrared pulses tunable from 9 to 18 μm at an 88-MHz repetition rate.*" *Opt Lett* **23**(11), 861–863 (1998).

[28] R. Huber, A. Brodschelm, F. Tauser & A. Leitenstorfer. "*Generation and field-resolved detection of femtosecond electromagnetic pulses tunable up to 41 THz.*" *Applied Physics Letters* **76**, 3191 (2000).

[29] Q. Wu & X. Zhang. "*Free-space electro-optic sampling of terahertz beams.*" *Applied Physics Letters* **67**, 3523–3525 (1995).

[30] Q. Wu & X. Zhang. "*Ultrafast electro-optic field sensors.*" *Applied Physics Letters* **68**, 1604–1606 (1996).

[31] A. Nahata, D. H. Auston, C. Wu & J. T. Yardley. "*Generation of terahertz radiation from a poled polymer.*" *Applied Physics Letters* **67**, 1358–1360 (1995).

[32] J. A. Valdmanis, G. Mourou & C. W. Gabel. "*Picosecond electro-optic sampling system.*" *Applied Physics Letters* **41**, 211–212 (1982).

[33] A. Nahata, D. H. Auston, T. F. Heinz & C. Wu. "*Coherent detection of freely propagating terahertz radiation by electro-optic sampling.*" *Applied Physics Letters* **68**, 150–152 (1996).

[34] H. J. Bakker, G. C. Cho, H. Kurz, Q. Wu & X. Zhang. "*Distortion of terahertz pulses in electro-optic sampling.*" *Journal of the Optical Society of America B Optical Physics* **15**, 1795–1801 (1998).

[35] G. Gallot & D. Grischkowsky. "*Electro-optic detection of terahertz radiation.*" *Journal of the Optical Society of America B Optical Physics* **16**, 1204–1212 (1999).

[36] H. Ohno. "*Making nonmagnetic semiconductors ferromagnetic.*" *Science* **281**(5379), 951 (1998).

[37] K. Ohno, S. Ohya & M. Tanaka. "*Properties of heavily Mn-doped GaMnAs with Curie temperature of 172.5 K.*" *Journal of Superconductivity and Novel Magnetism* **20**(6), 417–420 (2007).

[38] M. Scarpulla, U. Daud, K. Yu, O. Monteiro, Z. Liliental-Weber, D. Zakharov, W. Walukiewicz & O. Dubon. "*Diluted magnetic semiconductors formed by ion implantation and pulsed-laser melting.*" *Physica B: Physics of Condensed Matter* **340**, 908–912 (2003).

[39] H. Ohno. "*Properties of ferromagnetic III-V semiconductors.*" *J Magn Magn Mater* **200**, 110–129 (1999).

[40] T. Dietle, H. Ohno, F. Matsukura, J. Cibert & D. Farrand. "*Zener model description of ferromagnetism in zinc-blende magnetic semiconductors.*" *Science* **287**, 1019–1022 (2000).

[41] T. Dietl, H. Ohno & F. Matsukura. "*Hole-mediated ferromagnetism in tetrahedrally coordinated semiconductors.*" *Physical Review B* **63**(19), 195205 (2001).

[42] C. Bihler, M. Kraus, M. S. Brandt, S. T. B. Gronnenwein, M. Opel, M. A. Scarpulla, R. Farshchi, D. M. Estrada & O. D. Dubon. "*Suppression of hole-mediated ferromagnetism in $Ga_{1-x}Mn_xP$ by hydrogen.*" *J Appl Phys* **104**, 013908 (2008).

[43] P. Stone, M. Scarpulla, R. Farshchi, I. Sharp, E. Haller, O. Dubon, K. Yu, J. Beeman, E. Arenholz, J. Denlinger et al. "*Mn L x-ray absorption and magnetic circular dichroism in ferromagnetic GaMnP.*" *Applied Physics Letters* **89**, 012504 (2006).

[44] M. A. Scarpulla, B. L. Cardozo, R. Farshchi, W. M. H. Oo, M. D. McCluskey, K. M. Yu & O. D. Dubon. "*Ferromagnetism in $Ga_{1-x}Mn_xP$: Evidence for inter-Mn exchange mediated by localized holes within a detached impurity band.*" *Phys Rev Lett* **95**(20), 207204 (2005).

[45] S. Adachi. *GaAs and Related Materials: Bulk Semiconducting and Superlattice Properties* (World Scientific, Singapore; River Edge, NJ, 1994).

[46] M. Cardona. "*Band parameters of semiconductors with zincblende, wurtzite, and germanium structure.*" *J Phys Chem Solids* **24**, 1543 (1963).

[47] J. R. Chelikowsky & M. L. Cohen. "*Nonlocal pseudopotential calculations for electronic structure of 11 diamond and zincblende semiconductors.*" *Phys Rev B* **14**, 556–582 (1976).

[48] B. I. Min, S. Massidda & A. J. Freeman. "*Structural and electronic properties of bulk GaAs, bulk AlAs and the GaAs/AlAs superlattice.*" *Phys Rev B* **38**, 1970–1977 (1988).

[49] P. Y. Yu & M. Cardona. *Fundamentals of Semiconductors: Physics and Materials Properties* (Springer, Berlin; New York, 2001).

[50] E. I. Rashba. *Excitons* (North-Holland, Amsterdam, 1982).

[51] C. Y. P. Chao & S. L. Chuang. "*Analytical and numerical solutions for a two-dimensional exciton in momentum space.*" *Phys Rev B* **43**, 6530–6543 (1991).

[52] M. Haug & S. W. Koch. *Quantum Theory of the Optical and Electronic Properties of Semiconductors* (World Scientific, Singapore, 1993), 2 edition.

[53] L. C. Andreani & A. Pasquarello. "*Accurate theory of excitons in $GaAs/Ga_{1-x}Al_xAs$ quantum wells.*" *Phys Rev B* **42**, 8928–8938 (1990).

[54] G. Bastard. *Wave Mechanics Applied to Semiconductor Heterostructures* (Éditiones de physique, Les Ulis, France, 1988).

[55] L. V. Keldysh. "*Excitons in semiconductor dielectric nanostructures.*" *Phys Status Solidi A* **164**, 3–12 (1997).

[56] S. Schmitt-Rink, D. S. Chemla & D. A. B. Miller. "*Theory of transient excitonic optical nonlinearities in semiconductor quantum-well structures.*" *Phys Rev B* **32**, 6601–6609 (1985).

[57] C. Weisbuch & B. Vinter. *Quantum Semiconductor Structures: Fundamentals and Applications* (Academic Press, Boston, 1991).

[58] R. Winkler. "*Excitons and fundamental absorption in quantum wells.*" *Phys Rev B* **51**, 14395–14409 (1995).

[59] R. Kaindl, M. Carnahan, D. Hägele, R. Lövenich & D. Chemla. "*Ultrafast terahertz probes of transient conducting and insulating phases in an electron–hole gas.*" *Nature* **423**(6941), 734–738 (2003).

[60] R. Huber, F. Tauser, A. Brodschelm, M. Bichler, G. Abstreiter & A. Leitenstorfer. "*How many-particle interactions develop after ultrafast excitation of an electron–hole plasma.*" *Nature* **414**(6861), 286–289 (2001).

[61] E. I. Rashba. *Excitons* (North-Holland Publ. Co., Amsterdam, 1982).

[62] L. Keldysh & Y. Kopaev. "*Possible instability of the semimetal state toward coulomb interaction.*" *Soviet Phys JETP* **6**, 2219 (1965).

[63] N. Mott. "*The transition to the metallic state.*" *Philos Mag* **6**(62), 287–309 (1961).

[64] L. Kappei, J. Szczytko, F. Morier-Genoud & B. Deveaud. "*Direct observation of the Mott transition in an optically excited semiconductor quantum well.*" *Physical Review Letters* **94**(14), 147403 (2005).

[65] J. Shah. *Ultrafast Spectroscopy of Semiconductors and Semiconductor Nanostructures* (Springer Verlag, 1999).

[66] D. Chemla & J. Shah. "*Many-body and correlation effects in semiconductors.*" *Nature* **411**(6837), 549–557 (2001).

[67] A. Honold, L. Schultheis, J. Kuhl & C. Tu. "*Collision broadening of two-dimensional excitons in a GaAs single quantum well.*" *Physical Review B* **40**(9), 6442–6445 (1989).

[68] G. Tränkle, E. Lach, A. Forchel, F. Scholz, C. Ell, H. Haug, G. Weimann, G. Griffiths, H. Kroemer & S. Subbanna. "*General relation between band-gap renormalization and carrier density in two-dimensional electron-hole plasmas.*" *Physical Review B* **36**(12), 6712–6714 (1987).

[69] M. Choi, K. Je, S. Yim & S. Park. "*Relative strength of the screened Coulomb interaction and phase-space filling on exciton bleaching in multiple quantum well structures.*" *Physical Review B* **70**(8), 85309 (2004).

[70] G. Fehrenbach, W. Schäfer, J. Treusch & R. Ulbrich. "*Transient optical spectra of a dense exciton gas in a direct-gap Semiconductor.*" *Physical Review Letters* **49**(17), 1281–1284 (1982).

[71] N. Peyghambarian, H. Gibbs, J. Jewell, A. Antonetti, A. Migus, D. Hulin & A. Mysyrowicz. "*Blue shift of the exciton resonance due to exciton-exciton interactions in a multiple-quantum-well structure.*" *Physical Review Letters* **53**(25), 2433–2436 (1984).

[72] D. Wake, H. Yoon, J. Wolfe & H. Morkoc. "*Response of excitonic absorption spectra to photoexcited carriers in GaAs quantum wells.*" *Physical Review B* **46**(20), 13452–13460 (1992).

[73] G. Manzke, Q. Peng, K. Henneberger, U. Neukirch, K. Hauke, K. Wundke, J. Gutowski & D. Hommel. "*Density dependence of the exciton energy in semiconductors.*" *Physical Review Letters* **80**(22), 4943–4946 (1998).

[74] K. Litvinenko, D. Birkedal, V. Lyssenko & J. Hvam. "*Exciton dynamics in $GaAs/Al_xGa_{1-x}As$ quantum wells.*" *Physical Review B* **59**(15), 10255–10260 (1999).

[75] W. Knox, C. Hirlimann, D. Miller, J. Shah, D. Chemla & C. Shank. "*Femtosecond excitation of nonthermal carrier populations in GaAs quantum wells.*" *Physical Review Letters* **56**(11), 1191–1193 (1986).

[76] T. Timusk. "*Far-infrared absorption study of exciton ionization in germanium.*" *Physical Review B* **13**(8), 3511–3514 (1976).

[77] R. Groeneveld & D. Grischkowsky. "*Picosecond time-resolved far-infrared experiments on carriers and excitons in GaAs-AlGaAs multiple quantum wells.*" *Journal of the Optical Society of America B* **11**(12), 2502–2507 (1994).

[78] J. Černe, J. Kono, M. Sherwin, M. Sundaram, A. Gossard & G. Bauer. "*Terahertz dynamics of excitons in GaAs/AlGaAs quantum wells.*" *Physical Review Letters* **77**(6), 1131–1134 (1996).

[79] M. Kira, W. Hoyer, T. Stroucken & S. Koch. "*Exciton formation in semiconductors and the influence of a photonic environment.*" *Physical Review Letters* **87**(17), 176401 (2001).

[80] R. A. Kaindl, M. A. Carnahan, D. Hägele, R. Lövenich & D. S. Chemla. "*Ultrafast terahertz probes of transient conducting and insulating phases in an electron-hole gas.*" *Nature* **423**, 734 (2003).

[81] I. Galbraith, R. Charia, S. Pellegrini, P. J. Phillips, C. J. Dent, A. F. G. van der Meer, D. G. Clarke, A. K. Kar, G. S. Buller, C. R. Pidgeon, B. N. Murdin, J. Allam & G. Strasser. "*Excitonic signatures in the photoluminescence and terahertz absorption of $GaAs/Al_xGa_{1-x}As$ multiple quantum well.*" *Phys Rev B* **71**, 073302 (2005).

[82] J. Wolfe, W. Hansen, E. Haller, R. Markiewicz, C. Kittel & C. Jeffries. "*Photograph of an electron-hole drop in germanium.*" *Physical Review Letters* **34**(20), 1292–1293 (1975).

[83] R. Huber, F. Tauser, A. Brodschelm, M. Bichler, G. Abstreiter & A. Leitenstorfer. "*How many-particle interactions develop after ultrafast excitation of an electronhole plasma.*" *Nature* **414**, 286 (2001).

[84] R. Huber, R. Kaindl, B. Schmid & D. Chemla. "*Broadband terahertz study of excitonic resonances in the high-density regime in $GaAs/Al_xGa_{1-x}As$ quantum wells.*" *Physical Review B* **72**(16), 161314 (2005).

[85] H. Haug & S. W. Koch. *Quantum Theory of the Optical and Electronic Properties of Semiconductors* (World Scientific, Singapore, 2004).

[86] R. A. Kaindl, D. Hägele, M. A. Carnahan & D. S. Chemla. "*Transient terahertz spectroscopy of excitons and unbound carriers in quasi-two-dimensional electron-hole gases.*" *Physical Review B (Condensed Matter and Materials Physics)* **79**(4), 045320 (2009).

[87] M. D. Sturge & E. I. Rashba. *Excitons*, volume 2 of *Modern Problems in Condensed Matter Sciences* (North-Holland Pub. Co., Amsterdam; New York, 1982).

[88] L. Butov, C. Lai, A. Ivanov, A. Gossard & D. Chemla. "*Towards Bose-Einstein condensation of excitons in potential traps.*" *Nature* **417**(6884), 47–52 (2002).

[89] D. Snoke, J. Wolfe & A. Mysyrowicz. "*Evidence for Bose-Einstein condensation of a two-component exciton gas.*" *Physical Review Letters* **64**(21), 2543–2546 (1990).

[90] M. Kubouchi, K. Yoshioka, R. Shimano, A. Mysyrowicz & M. Kuwata-Gonokami. "*Study of Orthoexciton-to-Paraexciton conversion in Cu_2O by excitonic Lyman spectroscopy.*" *Physical Review Letters* **94**(1), 16403 (2005).

[91] M. Jörger, E. Tsitsishvili, T. Fleck & C. Klingshirn. "*Infrared absorption by excitons in Cu_2O.*" *physica status solidi(b)* **238**(3), 470–473 (2003).

[92] B. Ferguson & X. Zhang. "*Materials for terahertz science and technology.*" *Nature materials* **1**(1), 26–33 (2002).

[93] R. Huber, C. Kübler, S. Tübel, A. Leitenstorfer, Q. Vu, H. Haug, F. Köhler & M. Amann. "*Femtosecond formation of coupled phonon-plasmon modes in InP: Ultrabroadband THz experiment and quantum kinetic theory.*" *Physical Review Letters* **94**(2), 27401 (2005).

[94] C. Luo, K. Reimann, M. Woerner, T. Elsaesser, R. Hey & K. Ploog. "*Phase-resolved nonlinear response of a two-dimensional electron gas under femtosecond intersubband excitation.*" *Physical Review Letters* **92**(4), 47402 (2004).

[95] S. Nikitine. "*On the possibility of observation and the intensity of (nn') and (nn) transitions between exciton states in Cu_2O.*" *The Journal of Physics and Chemistry of Solids* **45**(8-9), 949–954 (1984).

[96] M. Kira & S. Koch. "*Exciton-population inversion and terahertz gain in semiconductors excited to resonance.*" *Physical Review Letters* **93**(7), 76402 (2004).

[97] E. Fortin, S. Fafard & A. Mysyrowicz. "*Exciton transport in Cu_2O: Evidence for excitonic superfluidity?*" *Physical Review Letters* **70**(25), 3951–3954 (1993).

[98] G. Kopelevich, S. Tikhodeev & N. Gippius. "*Phonon wind and excitonic transport in Cu_2O semiconductors.*" *Soviet Journal of Experimental and Theoretical Physics* **82**, 1180–1185 (1996).

[99] J. Lin & J. Wolfe. "*Bose-Einstein condensation of paraexcitons in stressed Cu_2O.*" *Physical Review Letters* **71**(8), 1222–1225 (1993).

[100] G. Kavoulakis & A. Mysyrowicz. "*Auger decay, spin exchange, and their connection to Bose-Einstein condensation of excitons in Cu_2O.*" *Physical Review B* **61**(24), 16619–16622 (2000).

[101] A. Mysyrowicz, D. Hulin & A. Antonetti. "*Long exciton lifetime in Cu_2O.*" *Physical Review Letters* **43**(15), 1123–1126 (1979).

[102] C. Uihlein, D. Fröhlich & R. Kenklies. "*Investigation of exciton fine structure in Cu_2O.*" *Physical Review B* **23**(6), 2731–2740 (1981).

[103] S. Glutsch, U. Siegner, M. Mycek & D. Chemla. "*Fano resonances due to coupled magnetoexciton and continuum states in bulk semiconductors.*" *Physical Review B* **50**(23), 17009–17017 (1994).

[104] A. Compaan & H. Cummins. "*Raman scattering, luminescence, and exciton-phonon coupling in Cu_2O.*" *Phys Rev B* **6**, 4753 (1972).

[105] *Cuprous Oxide (Cu_2O) Optical Properties.* Landoldt-Boernstein, Group III Condensed Matter (Springer, Berlin, 1998). Subvolume C.

[106] H. A. Bethe & E. E. Salpeter. *Quantum Mechanics of One- and Two-Electron Atoms* (Academic Press, New York, 1957).

[107] Y. Shen. "*Comment on: Resonant scattering or absorption followed by emission.*" *Physical Review B* **14**(4), 1772–1774 (1976).

[108] P. Yu & Y. Shen. "*Resonance Raman studies in Cu_2O. II. The yellow and green excitonic series.*" *Physical Review B* **17**(10), 4017–4030 (1978).

[109] S. Chuang, S. Schmitt-Rink, B. Greene, P. Saeta & A. Levi. "*Optical rectification at semiconductor surfaces.*" *Physical Review Letters* **68**(1), 102–105 (1992).

[110] Y. R. Shen. *The Principles of Nonlinear Optics* (Wiley, New York, 2002). Note: The relation follows from a simplified treatment of stimulated polariton scattering.

[111] Q. Wu & X. Zhang. "*Ultrafast electro-optic field sensors.*" *Applied Physics Letters* **68**, 1604 (1996).

[112] S. Leinß, T. Kampfrath, K. v. Volkmann, M. Wolf, J. Steiner, M. Kira, S. Koch, A. Leitenstorfer & R. Huber. "*Terahertz coherent control of optically dark paraexcitons in Cu_2O.*" *Physical Review Letters* **101**(24), 246401 (2008).

[113] S. Leinß, T. Kampfrath, K. Volkmann, B. Schmid, D. Fröhlich, M. Wolf, R. Kaindl, A. Leitenstorfer & R. Huber. "*THz quantum optics with dark excitons in Cu_2O: from stimulated emission to nonlinear population control.*" *Physica Status Solidi (B)* **6**(1), 156–161 (2008).